1984

Experimental Investigation of a Cylinder in Axial Motion at Low Reynolds Number.

Tsukasa Jeff Ui
Louisiana State University and Agricultural & Mechanical College

INFORMATION TO USERS

This reproduction was made from a copy of a document sent to us for microfilming. While the most advanced technology has been used to photograph and reproduce this document, the quality of the reproduction is heavily dependent upon the quality of the material submitted.

The following explanation of techniques is provided to help clarify markings or notations which may appear on this reproduction.

1. The sign or "target" for pages apparently lacking from the document photographed is "Missing Page(s)". If it was possible to obtain the missing page(s) or section, they are spliced into the film along with adjacent pages. This may have necessitated cutting through an image and duplicating adjacent pages to assure complete continuity.

2. When an image on the film is obliterated with a round black mark, it is an indication of either blurred copy because of movement during exposure, duplicate copy, or copyrighted materials that should not have been filmed. For blurred pages, a good image of the page can be found in the adjacent frame. If copyrighted materials were deleted, a target note will appear listing the pages in the adjacent frame.

3. When a map, drawing or chart, etc., is part of the material being photographed, a definite method of "sectioning" the material has been followed. It is customary to begin filming at the upper left hand corner of a large sheet and to continue from left to right in equal sections with small overlaps. If necessary, sectioning is continued again—beginning below the first row and continuing on until complete.

4. For illustrations that cannot be satisfactorily reproduced by xerographic means, photographic prints can be purchased at additional cost and inserted into your xerographic copy. These prints are available upon request from the Dissertations Customer Services Department.

5. Some pages in any document may have indistinct print. In all cases the best available copy has been filmed.

University Microfilms International
300 N. Zeeb Road
Ann Arbor, MI 48106

Ui, Tsukasa Jeff

EXPERIMENTAL INVESTIGATION OF A CYLINDER IN AXIAL MOTION AT LOW REYNOLDS NUMBER

The Louisiana State University and Agricultural and Mechanical Col. PH.D. 1984

EXPERIMENTAL INVESTIGATION OF A CYLINDER IN AXIAL MOTION AT LOW REYNOLDS NUMBER

A Dissertation

Submitted to the Graduate Faculty of the
Louisiana State University and
Agricultural and Mechanical College
in partial fulfillment of the
requirements for the degree of
Doctor of Philosophy

in

The Department of Physics and Astronomy

by
Tsukasa Jeff Ui
B.S., University of British Columbia, 1973
M.S., Simon Fraser University, 1978
May 1984

ACKNOWLEDGEMENTS

The author wishes to express his most sincere gratitude to his research advisor, Dr. R. G. Hussey for the many hours of patient guidance which were so unselfishly given.

Dr. R. P. Roger's assistance in providing the results of his computer calculations is greatly appreciated. Further thanks must be extended to Dr. A. M. D. Amarakoon for his assistance in generating the solutions of the integrals presented in Appendices I and II.

The staff of the Physics and Astronomy Department shop and Dr. Bill Good are to be thanked for their assistance in constructing the equipment necessary to this study.

TABLE OF CONTENTS

LIST OF TABLES

LIST OF FIGURES

ABSTRACT

Measurements were made on the terminal velocity of circular cylinders with length to diameter ratio $4 < L/D < 231$ moving parallel to their axes at low Reynolds number in a fluid bounded by a cylindrical container. The drag was found to vary inversely with the boundary diameter as suggested by Wakiya's theory for prolate spheroids. When extrapolated to infinite boundary, the results agree well with the numerical calculations of Youngren and Acrivos, Gluckman *et al.* and Swanson *et al.* and the experimental results of Heiss and Coull.

CHAPTER 1

INTRODUCTION

A. Statement of the Problem

Consider the problem illustrated in Fig. 1: A cylindrical tank of diameter H and height S is filled with a homogeneous, incompressible, Newtonian fluid (i.e., stress is linearly related to rate of strain) of density ρ and viscosity μ. A solid circular cylinder of length L and diameter D is coaxial with the cylindrical boundary and is moving with constant velocity U along its axis. The mid-point of the cylinder is at a distance S_t from the top of the boundary and a distance S_b from the bottom of the boundary. The Reynolds number $R_e = UL\rho/\mu$ is presumed to be $<<1$.

B. Theoretical and Experimental Background

1. Equations of Motion

The equations governing the motion of an incompressible isotropic, Newtonian fluid are the Navier-Stokes equation

$$\rho \frac{\partial \vec{v}}{\partial t} + \rho(\vec{v}\cdot\nabla)\vec{v} = -\nabla p + \mu\nabla^2 \vec{v} + \vec{F} \qquad (1.1)$$

and the continuity equation

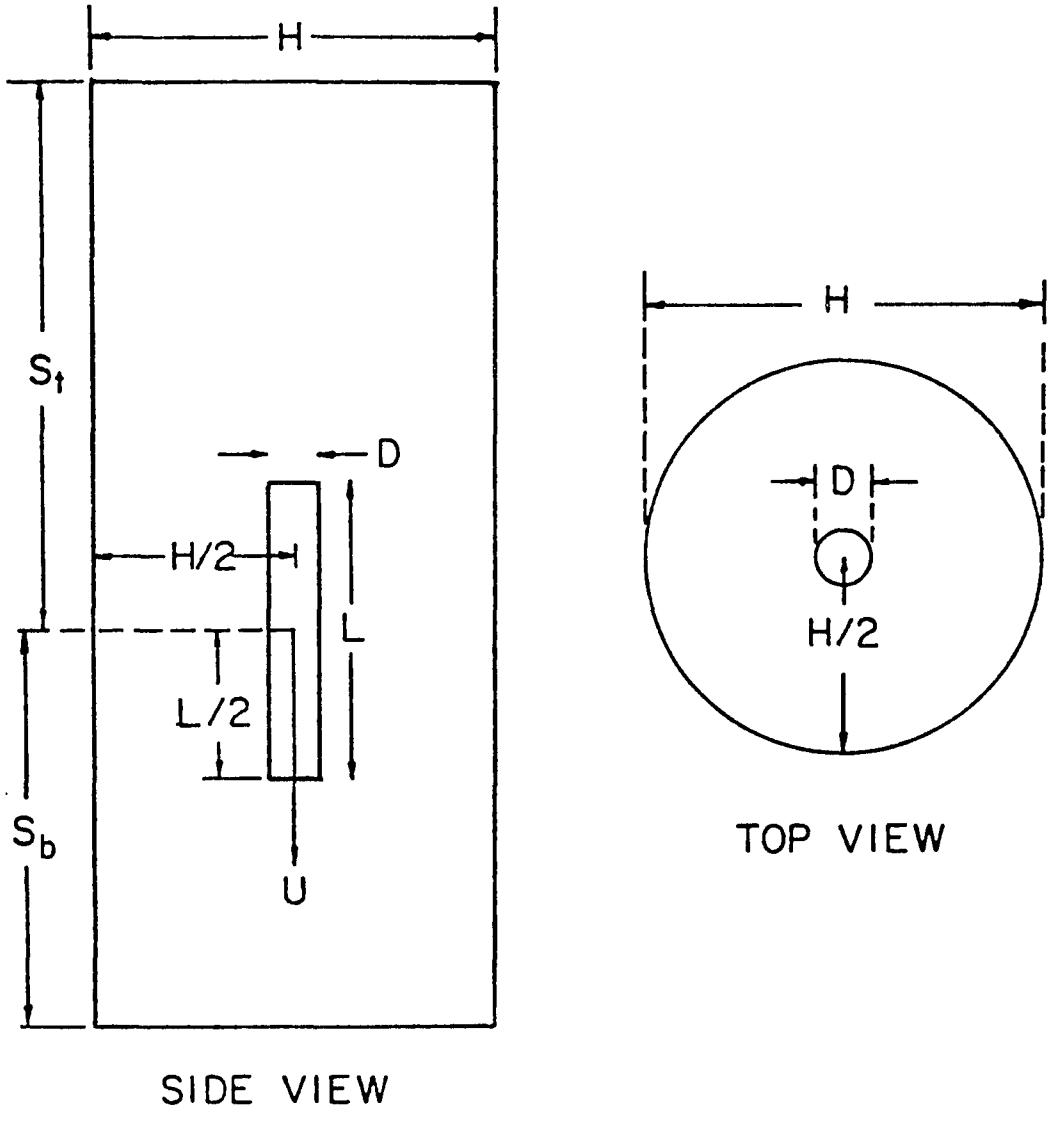

Fig. 1 Geometry and notation for a circular cylinder of finite length moving axially through a viscous fluid bounded by a cylindrical container.

$$\nabla \cdot \vec{v} = 0 \tag{1.2}$$

where $\vec{v} = \vec{v}(\vec{r},t)$ and $p = p(\vec{r},t)$ are respectively the velocity and pressure at the position $\vec{r}$ and time t. $\vec{F}$ is the body force (forces which act throughout the mass of the body) per unit volume. The pressure $-\nabla p$ and shear $\mu\nabla^2\vec{v}$ forces are classified as surface forces because they act on the boundary of a fluid particle. $\rho \frac{\partial \vec{v}}{\partial t}$ and $\rho(\vec{v}\cdot\nabla)\vec{v}$ are called inertial forces because they express the rate of change of momentum per unit volume of the fluid. For an incompressible, isotropic, homogeneous Newtonian fluid at constant temperature, the density ρ and the dynamic shear viscosity μ are constants independent of the position and shear rate. If the body force $\vec{F}$ is conservative (e.g., gravity), it can be written as the gradient of a scalar potential and combined with the pressure term in Eq. (1.1) to form a "modified" pressure. With this substitution Eq. (1.1) becomes

$$\rho \frac{\partial \vec{v}}{\partial t} + \rho(\vec{v}\cdot\nabla)\vec{v} = -\nabla p + \mu\nabla^2\vec{v} \tag{1.3}$$

where p is now the modified pressure. The Navier-Stokes equation is derived from the application of Newton's Second Law of Motion, which states that the rate of change of momentum of a particle is equal to the sum of the

external forces acting on the particle. The equation of continuity expresses the fact that mass is conserved. For an incompressible fluid, this is equivalent to stating that the divergence of the velocity $\vec{v}$ is zero.

The Navier-Stokes equation is an elliptic, second order partial differential equation. The appropriate boundary conditions to use are Dirichlet or Neumann conditions on a closed surface.[1,2] Usually this amounts to specifying the velocity on the solid boundary. For viscous fluid flow, this condition has been determined by direct observation[3] to be that there is "no slip" between the fluid and a solid boundary at the interface. In other words, if a solid is traveling with a velocity $\vec{U}$, the velocity $\vec{v}$ of the fluid at the boundary of the solid is

$$\vec{v} = \vec{U} \ .$$

2. The Reynolds Number and Stokes Flow Equations

In considering viscous fluid flow, the quantity of primary importance is the Reynolds number $Re = \frac{UL\rho}{\mu}$ where L is a characteristic dimension of the object under consideration, U is a characteristic velocity, ρ is the density of the fluid and μ is the dynamic viscosity of the fluid. The Reynolds number can be extracted from

the Navier-Stokes equation by rendering the equation dimensionless. If we introduce into Eq. (1.3) the dimensionless ratios

$$\vec{v}' = \frac{\vec{v}}{U} \quad , \quad \vec{r}' = \frac{\vec{r}}{L} \, , \quad p' = \frac{PL}{\mu U} \, , \quad \text{and} \quad t' = \frac{t}{\tau}$$

where τ is a characteristic time for the flow, we obtain

$$\frac{\rho U}{\tau} \frac{\partial \vec{v}'}{\partial t'} + \frac{\rho U^2}{L} (\vec{v}' \cdot \nabla') \vec{v}' = - \frac{\mu U}{L^2} \nabla' p' + \frac{\mu U}{L^2} \nabla'^2 \vec{v}' \, . \qquad (1.4)$$

If Equation (1.4) is multiplied by $L^2/\mu U$, we obtain

$$\frac{L^2 \rho}{\mu \tau} \frac{\partial \vec{v}'}{\partial t'} + \frac{UL\rho}{\mu} (\vec{v}' \cdot \nabla') \vec{v}' = -\nabla' p' + \nabla'^2 v' \qquad (1.5)$$

The equation above can be rewritten as

$$S \frac{\partial \vec{v}'}{\partial t'} + Re(\vec{v}' \cdot \nabla') \vec{v}' = -\nabla' p' + \nabla'^2 \vec{v}' \qquad (1.6)$$

where $S = L^2 \rho / \mu \tau$ is the Stokes number and $Re = UL\rho/\mu$ is the Reynolds number. If the flow is steady, the derivative of any variable with respect to time is zero (i.e. $\partial \vec{v}/\partial t = \partial \vec{v}'/\partial t' = 0$). In addition, if the Reynolds number is much less than one, equation (1.6) reduces to $\nabla' p' = \nabla'^2 \vec{v}'$. In terms of dimensional variables it is

$$\nabla p = \mu \nabla^2 \vec{v} \ . \qquad (1.7)$$

The equation above along with the continuity equation $\nabla \cdot \vec{v} = 0$ are called the Stokes or creeping flow equations. If $S \ll 1$, Equations (1.2) and (1.7) are called the quasi-steady Stokes flow equations.[4] If $S = 0(1)$, the unsteady term $\partial \vec{v}/\partial t$ in the equation of motion must be retained.[4,5] The Reynolds number can be thought of as the ratio of the inertial force to the viscous force,[6] so in the Stokes flow region when $Re \ll 1$, viscous forces are considerably greater than inertial forces.

3. Solutions to the Stokes Equations for Limiting Cases

No exact solution exists for the case of a cylinder of finite length moving axially in a cylindrical boundary of finite depth. However, approximate solutions are available for several limiting cases.

(a) Cylinder of infinite length in a coaxial cylindrical boundary of infinite length ($S_t \to \infty$, $S_b \to \infty$, $L \to \infty$).

The solution for this case is given by Happel and Brenner[7], but there is a typographical error in their expression. Their result for the inverse

dimensionless drag is

$$F \equiv \frac{F'}{2\pi\mu U} = \frac{1-[2D^2/(H^2-D^2)]\{1-[2D^2/(H^2-D^2)][\ell n\ H/D]\}}{[(H^2+D^2)/(H^2-D^2)][\ell n\ H/D - 1]} \tag{1.8}$$

where F' is the drag per unit length. H and D are as before the diameter of the cylindrical boundary and the diameter of the cylinder, respectively. The correct expression is

$$F = \frac{1-[2D^2/(H^2-D^2)]\{1-[2D^2/(H^2-D^2)][\ell n\ H/D]\}}{[(H^2+D^2)/(H^2-D^2)][\ell n\ H/D] - 1} \tag{1.9}$$

If we let $\sigma = H/D$, we obtain

$$F = \frac{\sigma^2-3+[4(\ell n\ \sigma)/(\sigma^2-1)]}{[(\sigma^2+1)(\ell n\ \sigma)] + 1-\sigma^2} \quad . \tag{1.10}$$

For $\sigma >> 1$, $F \to (\ell n\ \sigma)^{-1}$, so for a fluid of infinite extent ($\sigma \to \infty$), the drag is zero, which means simply that the only steady flow solution is one for which the entire fluid is moving with velocity $\vec{U}$. The same conclusion can be drawn from the solution for the impulsively

started axial motion of a cylinder of radius a and infinite length in the limit of large time. The solution for this case is[3]

$$F = \frac{F'}{2\pi\mu U} = \frac{4}{\pi^2} \int_0^\infty \frac{\exp(-k^2\nu t)\,dk}{k\{J_0^2(ka)+Y_0^2(ka)\}} \tag{1.11}$$

where ν is the kinematic viscosity $\nu = \mu/\rho$, $J_0(ka)$ is the Bessel function of the first kind of order zero and $Y_0(ka)$ is the Bessel function of the second kind of order zero. In the limit $t\to\infty$, the equation above reduces to

$$F = \frac{2}{\ell n(\nu t/a^2)} \quad . \tag{1.12}$$

For large t, F approaches zero.

(b) Cylinder of finite length in a fluid of infinite extent ($S_t \to \infty$, $S_b \to \infty$, $H \to \infty$).

For cylinders with $L/D \gg 1$, a technique known as slender body theory has been frequently used to solve for the Stokes drag. Slender body theory takes advantage of the slenderness of the object in order to achieve simplifications in obtaining approximate solutions. The primary simplification results from the observation that the velocities induced at a point on the surface of a slender body by singularities outside a certain "near-field" are dominated by Stokeslets (fundamental singularities of the Stokes equations corresponding to point forces) in the "far-field" since their far field effect ($\sim r^{-1}$) dominates that of other singularities.[8] The slender body can be represented by a distribution of Stokeslets along the axis of the body. Higher order solutions (moments) of the Stokes equations are included to satisfy the no slip boundary condition at the surface of the body. This leads to the following integral equation for the velocity $\vec{U}(r)$:[9]

$$U_i(\vec{r}) = \int_{-L/2}^{+L/2} G_{ij}(\vec{r},s) F_j(s)\,ds \qquad (1.13)$$

where s is the centerline of the body, $\vec{F}(s)$ is the drag per unit length acting on the body, and $G_{ij}(\vec{r},s)$ is the Green's function (distribution of Stokeslets and higher

moments) appropriate to the geometry of the problem and the no slip condition. Burgers[10] represented a circular cylinder by a line of force along its axis and obtained for the dimensionless drag per unit length

$$F = \frac{\varepsilon}{1-0.72\varepsilon} \tag{1.14}$$

where $\varepsilon = [\ell n(2L/D)]^{-1}$. Broersma[11] used a similar method and obtained a numerical coefficient of 0.81 instead of 0.72. Cox[12] showed that the coefficient should be $\alpha \equiv (3/2) - \ell n2 \cong 0.80685$. Batchelor[13] derived results for the axial and transverse drag on slender bodies of arbitrary cross-sectional shape. When restricted to the case of a circular cylinder in axial motion, his result for the dimensionless drag per unit length is

$$F_B = \frac{\varepsilon(1-\varepsilon H_{02})}{(1 - \frac{1}{2}\varepsilon)} + \varepsilon^3(H_{02} - \tfrac{1}{2} H_{01}) \ , \tag{1.15}$$

where $H_{01} = -1 + \ell n2$ and $H_{02} = 1 + (1 - \ell n2)^2 - \frac{\pi^2}{12}$. H_{01} and H_{02} are special cases of the integral defined by

$$H_{mn} = (m + 1)\int_0^1 \xi^m\{\ell n(1 - \xi^2)^{\frac{1}{2}}\}^n \, d\xi \ , \tag{1.16}$$

where m = 0 or 2 and n = 1 or 2. Batchelor obtained his result for H_{01} analytically and for H_{02} numerically. The analytical solutions for H_{01} and H_{02} are given in our

appendices I and II, respectively. Batchelor's expression for the drag F_B given in Eq. (1.15) can be simplified by expanding $(1 - \frac{1}{2}\varepsilon)^{-1}$ binomially. When expanded, the expression is

$$(1 - \tfrac{1}{2}\varepsilon)^{-1} \cong 1 + \tfrac{1}{2}\varepsilon + \tfrac{1}{4}\varepsilon^2 \ldots \tag{1.17}$$

If Eq. (1.17) is substituted into Eq. (1.15) we obtain

$$F_B \cong \varepsilon(1 - \varepsilon H_{02})(1 + \tfrac{1}{2}\varepsilon + \tfrac{1}{4}\varepsilon^2) + \varepsilon^3(H_{02} - \tfrac{1}{2}H_{01})$$

$$= \varepsilon + \tfrac{1}{2}\varepsilon^2 + \tfrac{1}{4}\varepsilon^3 - \varepsilon^2 H_{02} - \tfrac{1}{2}\varepsilon^3 H_{02} - \tfrac{1}{4}\varepsilon^4 H_{02}$$

$$+ \varepsilon^3(H_{02} - \tfrac{1}{2}H_{01})$$

$$= \varepsilon + (\tfrac{1}{2} - H_{02})\varepsilon^2 + (H_{02} - H_{01} + \tfrac{1}{4})\varepsilon^3 - \tfrac{1}{4}\varepsilon^4 H_{02}$$

$$\simeq \varepsilon + 0.80685\varepsilon^2 + 0.82854\varepsilon^3 \,. \tag{1.18}$$

Keller and Rubinow[14] used the method of matched asymptotic expansions[15] to obtain

$$F_{KR} = [\ell n \tfrac{L}{a} - \tfrac{3}{2} + \ell n\ 2 - (1 - \tfrac{\pi^2}{12})/(\ell n \tfrac{L}{a})]^{-1}$$

$$+ O\left[\frac{1}{\ell n\ L/a}\right]^4 , \tag{1.19}$$

where L is the length of the slender body and a is the radius. If we introduce the variable $\varepsilon = (\ell n\ L/a)^{-1} = (\ell n\ 2L/D)^{-1}$, where D is the diameter of the cylinder, F_{KR} becomes

$$F_{KR} = [\varepsilon^{-1} - \frac{3}{2} + \ell n2 - (1 - \frac{\pi^2}{12})\varepsilon]^{-1}$$

$$= [\frac{1 - (3/2 - \ell n2)\varepsilon - (1 - \pi^2/12)\varepsilon^2}{\varepsilon}]^{-1}$$

$$= \frac{\varepsilon}{1 - (3/2 - \ell n2)\varepsilon - (1 - \pi^2/12)\varepsilon^2} . \qquad (1.20)$$

The equation above can be expanded binomially (as for F_B) to obtain

$$F_{KR} = \varepsilon[1 - (3/2 - \ell n2) - (1 - \pi^2/12)\varepsilon^2]^{-1}$$

$$= \varepsilon[1 - (\alpha\varepsilon + \beta\varepsilon^2)]^{-1}$$

$$\cong \varepsilon[1 + \alpha\varepsilon + \beta\varepsilon^2 + (\alpha\varepsilon + \beta\varepsilon^2)^2] , \qquad (1.21)$$

where $\alpha = 3/2 - \ell n2$ and $\beta = 1 - \pi^2/12$. If, as previously, terms of order up to and including ε^3 are collected, we obtain

$$F_{KR} = \varepsilon + \alpha\varepsilon^2 + \beta\varepsilon^3 + \alpha^2\varepsilon^3$$

$$= \varepsilon + \alpha\varepsilon^2 + (\beta+\alpha^2)\varepsilon^3$$

$$= \varepsilon + (3/2 - \ell n2)\varepsilon^2 + [(1 - \pi^2/12) + (3/2 - \ell n2)^2]\varepsilon^3$$

$$= \varepsilon + 0.80685\varepsilon^2 + 0.82854\varepsilon^3 \ . \qquad (1.22)$$

Thus we see that the results of Batchelor, and Keller and Rubinow are the same to order ε^3.

Russel et al.[16] used numerical integration of the slender body integral equations to obtain a more accurate solution. From their Fig. 3 we have obtained the following approximate result

$$F_R = F_{KR} + 4\varepsilon^5 + 28\varepsilon^6 \ , \qquad (1.23)$$

which represents their results well for $\varepsilon < 0.275$.

For $0.25 \leq L/D \leq 4$, values of the drag have been calculated by Youngren and Acrivos,[17] Gluckman et al.,[18] and Swanson et al.[19] Youngren and Acrivos used a surface distribution of point forces and numerical integration over elements of surface area. Gluckman et al. approximated the cylinder by a set of touching oblate spheroids and solved the Stokes equations using the oblate spheroidal coordinate system. Swanson et al. represented the cylinder

by an array of small spheres covering the surface of the cylinder (beads-on-a-shell model). The drag on the array was evaluated by means of the modified Oseen interaction tensor. More details and references are given by Roger and Hussey,[20] Teller et al.[21] and Garcia de la Torre and Bloomfield,[22] and in Section E of this chapter. The results of these three approaches are in substantial agreement and also agree with the experimental values of Heiss and Coull[23] and of Blumberg and Mohr,[24] as can be seen in Table I. Values of the dimensionless drag for short cylinders including those from Roger's[25] beads-on-a-shell calculations are given in Table I. In the limit $L/D \to 0$, the drag should approach the well-known solution for a disk of zero thickness, $8\mu UD$.

Youngren and Acrivos also calculated the drag in the intermediate range $4 \leq L/D \leq 100$. Their values for L/D equal to 60, 80 and 100 are in good agreement with the slender body results of Russel et al. Gluckman et al. obtained approximate values of the drag for L/D equal to 10, 20, and 40 by representing the cylinder by touching prolate spheroids; their values are consistently lower than those of Youngren and Acrivos as can be seen in Fig. 3.8 in Chapter 3. DeMestre[26] has made measurements for L/D ranging from 15.6 to 98.1. His experimental values of the drag are 13 to 24% higher than his slender body

calculations, which include the effects of parallel plane walls.

TABLE I

VALUES OF THE DIMENSIONLESS DRAG
FOR CYLINDERS IN AXIAL MOTION

L/D	F_d = drag/8μUD				
	Roger[25]	Youngren and Acrivos[17]	Gluckman et al[18]	Swanson et al[19]	Heiss and Coull[23]
0.00	1.0000				
0.25	1.1081				
0.50	1.2109	1.226	1.220	1.223	1.239
0.75	1.3076				
1.00	1.3994	1.414	1.405	1.409	1.408
1.50	1.5699				
2.00	1.7279	1.739	1.723	1.736	1.743
4.00	2.2881	2.297	2.270	2.294	2.304
10.00	3.6789	3.687			

(c) Cylinder of finite length approaching an infinite plane wall ($S_t \to \infty$, $H \to \infty$).

The case of a slender cylinder ($L >> D$) has been treated by deMestre and Russel.[27] Their result is

$$F = \frac{F'}{2\pi\mu U} = \varepsilon \left[1 + \frac{1}{2} \varepsilon \{-0.614 + W_{111}\} + 0(\varepsilon^2) \right] , \tag{1.24}$$

where F' is the drag per unit length and W_{111} is

$$W_{111} = \left(\frac{2S_b}{L} + 1\right) \ell n \left(1 + \frac{L}{2S_b}\right) + \left(\frac{2S_b}{L} - 1\right) \ell n \left(1 - \frac{L}{2S_b}\right) + \frac{L}{4S_b} . \tag{1.25}$$

In deMestre and Russel's notation, the distance of the mid-point of the cylinder from the bottom boundary S_b is given as L and the length L of the cylinder is given as 2ℓ. When the cylinder is far from the wall (i.e., $L/2S_b << 1$), W_{111} becomes

$$\begin{aligned} W_{111} &\cong \left(\frac{2S_b}{L} + 1\right) \left(\frac{L}{2S_b} - \left(\frac{L}{2S_b}\right)^2/2\right) \\ &\quad + \left(\frac{2S_b}{L} - 1\right) \left(-\frac{L}{2S_b} - \left(\frac{L}{2S_b}\right)^2/2\right) + \frac{L}{4S_b} \\ &= \frac{3L}{4S_b} \to 0 , \end{aligned} \tag{1.26}$$

where we have used the expansion

$$\ell n(1 + x) \cong x - \frac{x^2}{2} + \ldots \quad \text{for} \quad -1 < x \leq 1.$$

The dimensionless drag in this case is

$$F = \varepsilon - 0.307\ \varepsilon^2 \ . \tag{1.27}$$

This does not agree with the results of Batchelor, and Keller and Rubinow beyond the first order in ε.

The case of a thin disk close to the bottom wall ($L << D$, $S_b - \frac{1}{2} L << D$) has been treated by lubrication theory and is a case of the squeeze film problem.[28]

(d) Spheroids in a cylindrical boundary of infinite depth ($S_t \to \infty$, $S_b \to \infty$).

Wakiya[29] extended Oberbeck's[30] solution for the drag on ellipsoids in infinite fluid, to include the effect of a cylindrical boundary of infinite depth. For a prolate spheroid of major axis L and minor axis D, falling in a boundary of diameter H, Wakiya's solution for the drag can be written

$$\frac{F}{F_\infty} = \frac{1}{1 - \frac{3}{4}\frac{R}{H}\left[5.6112 - 2.0211\ (\frac{L}{H})^2 - \frac{3.5431}{A^2}\ (\frac{L}{H})^2\right]} \tag{1.28}$$

where F_∞ is the dimensionless drag per unit length in infinite fluid and

$$R = \frac{8}{3} \frac{(D/2)}{\left[- \frac{2A}{A^2-1} + \frac{2A^2-1}{(A^2-1)^{3/2}} \ln \left(\frac{A+(A^2-1)^{1/2}}{A-(A^2-1)^{1/2}} \right) \right]} . \tag{1.29}$$

A is the aspect ratio L/D. When A >> 1, R becomes

$$R \cong \frac{2}{3} \frac{(D/2)(L/D)}{(\ln \frac{2L}{D} - 0.5)}$$

$$= \frac{1}{3} \frac{L}{(\ln \frac{2L}{D} - 0.5)} . \tag{1.30}$$

If Eq. (1.30) is substituted into Eq. (1.28) and if terms of order $(L/H)^3$ are ignored, we obtain

$$\frac{F}{F_\infty} = \frac{1}{1 - \frac{C}{(\ln \frac{2L}{D} - 0.5)} \frac{L}{H}} ,$$

which can be rewritten as

$$\frac{F}{F_\infty} = 1 + C F_\infty \frac{L}{H} . \tag{1.31}$$

We have used Oberbeck's result

$$F_\infty = \frac{1}{(\ell n \frac{2L}{D} - 0.5)} \quad .$$

C is a constant equal to $5.6112/4 \cong 1.403$. Chang[31] obtained a similar expression in his perturbation solution for the Stokes drag for axially symmetric bodies moving inside a cylindrical tube. Chang's expression is

$$\frac{F}{F_\infty} = 1 + \frac{(2.203)(2\pi\mu UL)F_\infty}{\pi^2 \mu UH}$$

$$= 1 + 1.402\ F_\infty \frac{L}{H} \quad . \tag{1.32}$$

Theoretical treatments of the influence of a boundary on the drag of a particle by Brenner[32] and Williams[33] indicate that the correct expression for the boundary effect in that case is

$$\frac{F}{F_\infty} = [1 - \frac{kF'_\infty}{6\pi\mu U(H/2)} + O(\frac{L}{H})^3]^{-1}$$

$$= [1 - \frac{(2.1044)(2\pi\mu UL)F}{6\pi\mu U(H/2)} + O(\frac{L}{H})^3]^{-1}$$

$$= [1 - 1.403\ F_\infty \frac{L}{H}]^{-1} \quad . \tag{1.33}$$

In Brenner's notation $F'_\infty = 2\pi\mu ULF_\infty = D_\infty$, $L = 2C$ and

$H = 2\ell$. Equations (1.31) through (1.33) suggest possible methods of treating the boundary effect on cylinders in axial motion in a cylindrical boundary. The results of Wakiya and Chang imply that a plot of F vs $\frac{1}{H}$ should be linear whereas Brenner's solution implies that a plot of $\frac{1}{F}$ vs $\frac{1}{H}$ should be linear.

A way of accounting for the boundary influence on disks (like oblate spheroids) is also suggested by Wakiya's theory[29] for spheroids. Wakiya's expression for the effect of a cylindrical boundary on the drag of an oblate spheroid is

$$\frac{F}{F_\infty} = [1 - \frac{3}{4}\frac{R}{H}[5.6112 - 2.0211\, A^2(\frac{D}{H})^2 - 3.5431(\frac{D}{H})^2]]^{-1}, \tag{1.34}$$

where R is given by

$$R = \frac{4}{3} D[\frac{2A}{1-A^2} + \frac{2(1-2A^2)}{(1-A^2)^{3/2}} + {}^{+}_{a}n^{-1}\ (\frac{(1-A^2)^{1/2}}{A})]^{-1} \ . \tag{1.35}$$

Equation (1.34) can be written in the form

$$\frac{F}{F_\infty} = [1 - \lambda(\frac{D}{H}) + \delta(\frac{D}{H})^3]^{-1} \ , \tag{1.36}$$

where

$$\lambda = \frac{3}{4}\,\frac{(5.6112)R}{D} \tag{1.37}$$

and

$$\delta = \frac{3R}{4D}\,[2.0211A^2 + 3.5431]\ . \tag{1.38}$$

We can assume that an expression of the form given by Eq. (1.36) also applies to disks but the coefficients λ and δ may be different. However, in the limit $A \to 0$ the two results must approach the result for the ideal disk of zero thickness. In the limit $A \to 0$, R is equal to $4D/3\pi$. This corresponds to values of $\lambda = 1.786$ and $\delta = 1.128$.

C. Transverse Motion of Cylinders

Additional experimental data exist for the motion of a cylinder in viscous fluid. However, these investigations were conducted for the case of a cylinder moving perpendicular to its axis of rotational symmetry (transverse motion). Huner[34] examined the effect of parallel sidewall boundaries on the drag of cylinders in transverse motion. Stalnaker[35] measured the drag on a cylinder as a function of the parallel sidewall separation distance and the end-wall separation distance. Chen[36] examined the behavior of a cylinder as it approached a plane bottom boundary. These results and those for axial motion have practical application in biophysics, in the propulsion of flagellated micro-organisms.[37] Propulsion occurs because while executing a spiral like motion,[38] the portion of the flagellum parallel to the motion experiences less drag per unit length than the portion which is perpendicular to the motion. According to Taylor,[39] the ratio of transverse drag (F_{tr}) to axial drag (F_{ax}) for a cylinder approaches 2 as $\varepsilon \to 0$ (L/D becomes large). Tillett[40] and Weinberger[41] have shown that this limit is approached from below. Tillet's expression for the ratio is

$$\frac{F_{tr}}{F_{ax}} = 2 + 2(\ell n\ \phi)^{-1} + 0[(\ell n\ \phi)^{-2}] \ , \qquad (1.39)$$

where ϕ is defined by the equations for a slender axisymmetric body

$$r \equiv (x^2 + y^2)^{\frac{1}{2}} = \phi R(z) \qquad (-L/2 \leq z \leq L/2) \tag{1.40}$$

and

$$\max R(z) = D/2 \ . \tag{1.41}$$

For a spheroidal body whose surface is represented by

$$\frac{x^2}{a^2} + \frac{y^2}{b^2} + \frac{z^2}{c^2} = 1 \ , \tag{1.42}$$

$R(z)$ is given by

$$R(z) = [c^2 - z^2]^{\frac{1}{2}} \ . \tag{1.43}$$

The constants a and b (a=b for a spheroid) are the semi-minor axes and c the semi-major axis. Equation (1.42) can be rearranged so that

$$(x^2 + y^2)^{\frac{1}{2}} = \frac{a}{c} (c^2 - z^2)^{\frac{1}{2}} \ . \tag{1.44}$$

Therefore

$$\phi = \frac{(x^2+y^2)^{\frac{1}{2}}}{R(z)} = \left[\frac{a}{c} (c^2 - z^2)^{\frac{1}{2}} \right] / [c^2 - z^2]^{\frac{1}{2}} = \frac{a}{c} .$$

(1.45)

The ratio F_{tr}/F_{ax} can now be written as $F_{tr}/F_{ax} = 2 + 2(\ell n \frac{a}{c})^{-1}$. For a cylinder this is equivalent to

$$\frac{F_{tr}}{F_{ax}} = 2 + 2(\ell n \frac{D}{L})^{-1} , \qquad (1.46)$$

where a = D/2 and c = L/2. The equation above can be expressed in terms of the parameter ε by the following method. We note that $\ell n(D/L) = [\ell n(\frac{L}{D})^{-1}] = -\ell n \frac{L}{D}$ and

$$\varepsilon = \frac{1}{\ell n \frac{2L}{D}} = \frac{1}{\ell n \frac{L}{D} + \ell n\ 2}$$

so that

$$\ell n(\frac{L}{D}) = \frac{1 - \varepsilon\ \ell n\ 2}{\varepsilon} .$$

Hence,

$$\frac{F_{tr}}{F_{ax}} = 2 + 2(\ell n \frac{D}{L})^{-1} = 2 - \frac{2}{\ell n \frac{L}{D}} = 2 - \frac{2\varepsilon}{1 - \varepsilon\ \ell n\ 2} .$$

(1.47)

If we expand the denominator binomially, we get

$$\frac{F_{tr}}{F_{ax}} = 2 - 2\varepsilon - 2\varepsilon^2 \ln 2 + \ldots \qquad (1.48)$$

We see that F_{tr}/F_{ax} approaches the value 2 from below (i.e. $F_{tr}/F_{ax} < 2$ for $L/D < \infty$).

D. Inertial Corrections to the Stokes Equation

The first attempt to evaluate the inertial term $[(\vec{v}\cdot\nabla)\vec{v}]$ in the Navier-Stokes equation when the approximation Re << 1 is not valid was made by Whitehead (1889)[42] who tried to extend Stokes' solution for the drag $D' = 6\pi\mu aU$ on a sphere of radius a to higher Reynolds number by using an iterative scheme. However, as Whitehead discovered, no solution exists which satisfies the condition of uniform flow at infinity, when the convective term is added to the Stokes equations. A description of Whitehead's scheme is given in the book by Happel and Brenner (p. 43). Oseen[43] showed that Stokes' approximation, in which inertial forces are presumed to be everywhere negligible compared to viscous forces, is not valid at distances far from the sphere. As Oseen pointed out, Stokes' solution of the creeping flow equations is of the form $\vec{v} = \vec{U} + UaO(r^{-1})$ far from the sphere, so that $\nabla^2\vec{v} = UaO(r^{-3})$ and $\vec{v}\cdot\nabla\vec{v} = U^2aO(r^{-2})$. The ratio of the inertial force to the viscous force at a distance r far from the sphere is

$$\frac{\rho|\vec{v}\cdot\nabla\vec{v}|}{\mu|\nabla^2\vec{v}|} = O\left(\frac{rU\rho}{\mu}\right) .$$

Thus for large r when $rU\rho/\mu$ is of the order 1, the inertial term must be retained. At this distance, Oseen suggested that the local velocity $\vec{v}$ is well approximated by the

free stream velocity U, so that the convective term can be approximated by $\rho\vec{U}\cdot\nabla\vec{v}$. Oseen solved the resulting equations (Oseen's equations)

$$\mu\nabla^2\vec{v}-\nabla p = \rho\vec{U}\cdot\nabla\vec{v} \tag{1.49}$$

and

$$\nabla\cdot\vec{v} = 0 \tag{1.50}$$

for the drag on a sphere. His solution is

$$D' = 6\pi\mu aU\ [1 + \frac{3}{8}\ Re + O(Re^2)]\ . \tag{1.51}$$

In the limit $Re \to 0$, the equation above reduces to Stokes' solution.

Some questions over the validity of Oseen's inertial correction factor 3/8 Re existed, since the approximation $\vec{U}\cdot\nabla\vec{v}$ fails in the region close to the sphere, where the no slip boundary condition requires that $\vec{v}\cdot\nabla\vec{v}$ be small. Proudman and Pearson[44] suggested that Oseen's solution provides a uniformly valid zeroth order approximation to the Navier-Stokes equation and could be used to justify Stokes' result but not be used directly to generate higher order solutions. Their method of solution was to generate two expressions, one being valid near the body (Stokes

expansion) and the other being valid far from the body (Oseen expansion). These two solutions were then uniquely determined by matching them in their common area of validity. Details of this "Method of Matched Asymptotic Expansions" are given in the book by Van Dyke. Proudman and Pearson's result for the drag on a sphere at low Reynolds number is

$$D' = 6\pi\mu aU \left[1 + \frac{3}{8} Re + \frac{9}{40} Re^2 \ln Re + O(Re^2)\right] . \quad (1.52)$$

Chester and Breach[45] extended Proudman and Pearson's result to higher order in Re to obtain

$$D' = 6\pi\mu aU \left[1 + \frac{3}{8} Re + \frac{9}{40} Re^2 \left(\ln Re + \gamma + \frac{5}{3} \ln 2 - \frac{323}{360}\right) + \frac{27}{80} Re^3 \ln Re + O(Re^3)\right] , \quad (1.53)$$

where γ is Euler's number equal to 0.5772156699... When compared with the experimental results of Maxworthy[46] and of Sutterby,[47] the lower order solution of Proudman and Pearson agrees with experiment to a higher Reynolds number (Re $\sim$ 1) than the solution of Chester and Breach (Re $\sim$ 0.7).

Breach[48] generalized the results of Proudman and Pearson for a sphere, to apply to all ellipsoids of revolution, both prolate and oblate. His result for the drag on a prolate spheroid of major axis L and minor axis D is

$$D' = \frac{\pi\mu ULB}{(1-\ ^2)}\ [\ 1 + \frac{BRe}{24} + \frac{B^2Re^2}{360}\ \ell n\ Re + O(Re^2)]\ ,$$

(1.54)

where e is the eccentricity equal to $(L^2-D^2)^{\frac{1}{2}}/L$ and B is given by

$$B = 24e^3[(1+e^2)\ell n(\frac{1+e}{1-e}) - 2e]^{-1}\ . \qquad (1.55)$$

For the oblate spheroid, he obtained

$$D' = \frac{2\pi\mu UDb}{3}\ [1 + \frac{bRe}{24} + \frac{b^2}{360}\ Re^2\ \ell n\ Re + O(Re^2)]\ ,$$

(1.56)

where b is given by

$$b = 12e^3[e(1-e^2)^{\frac{1}{2}} + (2e^2-1)\tan^{-1}\ [\frac{e}{(1-e^2)^{\frac{1}{2}}}]]^{-1}\ .$$

(1.57)

The eccentricity e is now equal to $(D^2-L^2)^{\frac{1}{2}}/D$. For the oblate spheroid, e = 1 or L = 0 corresponds to the case of an ideal disk of thickness zero moving broadside on to the flow. The drag for this case is

$$D' = 8\mu UD \left[1 + \frac{Re}{\pi} + \frac{8Re^2}{5\pi^2} \ln Re + O(Re^2)\right] . \qquad (1.58)$$

The first two terms of equations (1.54) and (1.56) were given by Oseen.

Brenner[49] solved Oseen's equations for the resistance of a particle of arbitrary shape moving parallel to a principal axis of resistance. His solution for the Oseen drag is

$$D' = D_s \left[1 + \frac{D_s}{16\pi\mu CU} Re + O(Re^2)\right] , \qquad (1.59)$$

where D_s is the Stokes drag and C is a characteristic particle dimension. Brenner and Cox[50] used the method of matched asymptotic expansions to solve for the drag on a particle of arbitrary shape in motion at low Reynolds numbers. Their solution for the case of a particle moving parallel to a principal axis of resistance is

$$D' = D_s\left[1 + \frac{3}{8}\left(\frac{D_s}{6\pi\mu CU}\right)Re + \frac{9}{40}\left(\frac{D_s}{6\pi\mu CU}\right)^2 Re^2 \ln Re + O(Re^2)\right] . \qquad (1.60)$$

We see that equation (1.60) is identical to Proudman and Pearson's result for the sphere if the substitution $D_s = 6\pi\mu CU$ is made. It can also be seen that the above equation agrees with the results of Breach for prolate and oblate spheroids.

E. Beads-on-a-Shell Model

1. Introduction

In previous sections we have dealt with solutions of the Stokes equations which represented a cylinder by a line distribution of point forces and other singularities along the axis of the body. Reference has also been made to the work of Youngren and Acrivos who used a surface distribution of point forces to calculate the drag for spheroids and for axial motion of circular cylinders. This was accomplished by evaluating elements of the hydrodynamic interaction tensor (for interaction between point forces) developed by Oseen[43] and Burgers,[10] by numerical integration over small sections of the surface of the body. In the beads-on-a-shell method a body is represented by an array of small touching spheres (beads) distributed over the surface. The Stokes flow drag is evaluated[53] using the modified Oseen tensor which results from averaging the pairwise interaction tensor over the beads centered at the site of the point forces. Bloomfield et al.[54] have shown that in the limit of an infinite number of beads (continuous distribution of point forces) this method yields the exact result Drag = $6\pi\mu UR$ for the Stokes flow drag of a sphere of radius R. Swanson et al.[19] report good agreement between their beads-on-a-shell calculations and the exact solutions for spheroids, the hemispherical cap and the experimental results of Heiss and Coull for

circular cylinders of length to diameter ratios of 0.5 to 4.0.

2. Theory

A clear and concise account of the beads-on-a-shell theory is given in the article by Roger and Hussey[20] and is followed here.

For a point force $\vec{F}$ located at the origin, the velocity perturbation at $\vec{r}$ is given by

$$\vec{V}' = T_o(\vec{r})\vec{F} \ , \tag{1.61}$$

where $T_o(\vec{r})$ is the Oseen interaction tensor

$$T_o(\vec{r}) = \frac{1}{8\pi\mu Ur} \left[I + \frac{\vec{r}\vec{r}}{r^2} \right] , \tag{1.62}$$

and I is the unit tensor. The finite size of the bead in the beads-on-a-shell method is incorporated into the tensor by distributing the point force over a spherical surface of radius a with the center at the origin and averaging $T_o(\vec{r} - \vec{a})$ over the spherical surface. The result is

$$T(\vec{r}) = \frac{1}{8\pi\mu Ur} \left[\left(1 + \frac{a^2}{3r^2}\right) I + \left(1 - \frac{a^2}{r^2}\right) \frac{\vec{r}\vec{r}}{r^2} \right] . \tag{1.63}$$

If $\vec{F}$ is set equal to $6\pi\mu a\vec{U}$, the Stokes drag on a sphere of radius a moving with velocity $\vec{U}$ in an unbounded fluid, then $T(\vec{r})\vec{F}$ gives the Stokes velocity distribution around the sphere.[53]

In order for this method to be of use in calculating the drag on objects such as circular cylinders and disks, the above procedure is extended to two spheres fixed relative to each other and moving with the same velocity $\vec{U}$ through the fluid. The force exerted on the fluid by bead 1 can be written as

$$\vec{F}_1 = \zeta(\vec{U} - \vec{V}_1') \ , \tag{1.64}$$

where $\zeta = 6\pi\mu a$ is the Stokes friction coefficient, and $\vec{V}_1'$ is the perturbation due to bead 2 at the surface of bead 1. $\vec{V}_1'$ is calculated by averaging the Oseen tensor $T_o(\vec{r}_{12} - \vec{a}_1 + \vec{a}_2)$, where $\vec{a}_1$ and $\vec{a}_2$ are the radius vectors of the two beads, over both spherical surfaces. This results in the modified Oseen interaction tensor[53]

$$T_{12} = \frac{1}{8\pi\mu r_{12}} \left[\left(1 + \frac{2a^2}{3r_{12}^2}\right) I + \left(1 - \frac{2a^2}{r_{12}^2}\right) \frac{\vec{r}_{12}\vec{r}_{12}}{r_{12}^2} \right] \tag{1.65}$$

for non-overlapping beads of the same radius a. For overlapping beads of the same radius T_{12} has been shown by

Rotne and Prager[56] to be

$$T_{12} = \frac{1}{6\pi\mu a}\left[\left(1 - \frac{9r_{12}}{32a}\right)I + \frac{3\vec{r}_{12}\vec{r}_{12}}{32ar_{12}}\right] . \qquad (1.66)$$

If the radii are not equal the modified interaction tensor takes the form[22]

$$T_{12} = \frac{1}{8\pi\mu r_{12}}\left[\left(1 + \frac{a_1^2+a_2^2}{3r_{12}^2}\right)I + \left(1 - \frac{a_1^2+a_2^2}{r_{12}^2}\right)\frac{\vec{r}_{12}\vec{r}_{12}}{r_{12}^2}\right] . \qquad (1.67)$$

If we substitute for the tensor, the force on the fluid at $\vec{r}_1$ can be written as

$$\vec{F}_1 = \zeta_1\vec{U} - \alpha_1 T_{12}\vec{F}_2 . \qquad (1.68)$$

For a rigid assembly of N beads, the force on the fluid at the site of ith bead (equal in magnitude to the drag on the bead) is

$$\vec{F}_i = \zeta_i\vec{U} - \sum_{\substack{j=1 \\ i\neq j}}^{N} \zeta_i T_{ij}\vec{F}_j . \qquad (1.69)$$

The drag on the array is determined by solving an alternate form of the equal above given by

$$\sum_{j=1}^{N} \delta_{ij}\vec{F}_j + \sum_{\substack{j=1 \\ i\neq j}}^{N} \zeta_i T_{ij}\vec{F}_j = \zeta_i \vec{U} \ , \tag{1.70}$$

which represent a system of N equations, each having three components. The set of equations above can be written as

$$MF = 6\pi\mu U \ , \tag{1.71}$$

where M is a 3N X 3N matrix consisting of 3 X 3 blocks M_{ij} given by

$$M_{ij} = \begin{cases} 6\pi\mu \ T_{ij} \ , & i \neq j \ , \\ \\ \dfrac{1}{a_i} \ I \ . \end{cases} \tag{1.72}$$

F and U are 3N X 1 column vectors, which for the array of beads traveling in the Z direction is given by

$$F = \begin{pmatrix} F_{1x} \\ F_{1y} \\ F_{1z} \\ \vdots \\ F_{nz} \end{pmatrix} \quad \text{and} \quad U = \begin{pmatrix} 0 \\ 0 \\ 1 \\ \vdots \\ 0 \\ 0 \\ 1 \end{pmatrix} \vec{U} \ . \tag{1.73}$$

The force components on each bead are calculated by solving

$$F = 6\pi\mu M^{-1}U \ . \qquad (1.74)$$

This involves the inverting of the 3N X 3N matrix M, where N is the number of beads in the assembly. By repeating the calculations for larger N, an extrapolation to the case for an infinite number of beads (continuous distribution of point forces) covering the body can be made.

3. Results

Roger[56] has used the beads-on-a-shell method to calculate the drag for several shapes for which analytical solutions are available. The results of these calculations are given in Table II, which includes results for the ideal disk of zero thickness, the sphere, the body of revolution whose section is a cardioid and a hemispherical cap for which a separation in flow occurs.[57,58] Additional results are given for two symmetric double-convex lens shapes constructed from the intersection of two spheres.[59,60] The interior angle at the intersection of the two spheres is 30° for one lens and 120° for the other lens. The agreement between the calculated and exact values of the drag for all shapes with the exception of the hemispherical cap, is very close, with the % difference ranging from a low of 0.001% for the disk of zero thickness to a high of

TABLE II

Comparison Between Drag Values Calculated With the Beads-on-a-Shell Method and Exact Solutions

Shape	F_d = drag/8μUD		
	Calculated	Exact	% Difference
disk	1.00001	1.00000	0.001
30° lens	1.00021	1.00032	0.012
120° lens	1.03731	1.03791	0.057
sphere	1.17812	1.17810	0.002
cardioid	1.16140	1.16155	0.013
hemispherical cap	1.03313...	1.08905...	5.135

0.057% for the 120° lens.

There appears to be an inconsistency between Roger's results and those of Swanson and Teller[19] for the hemispherical cap. According to Roger, the % difference between the calculated and exact values is 5.135%, which suggests that the beads-on-a-shell method fails to yield accurate results for shapes for which separation occurs. Swanson and Teller reported for the translational friction coefficient $f = |\vec{F}|/|\vec{U}|$, a calculated value of 3.4956 and an exact value of 3.4918. This corresponds to a % difference of [(3.4956 - 3.4918)/(3.4918)] X 100% = 0.11%. In addition, the relationship between the exact solution 3.4918 reported by Swanson and Teller and the exact result of Collins[61] for the hemispherical cap $f = |\vec{F}|/|\vec{U}| = |(3\pi + 8)\mu\vec{U}a|/|\vec{U}| = (3\pi + 8)\mu a$, is not clear, since the coefficient 3.4918 does not seem to be related in any simple way to the value $3\pi + 8 = 17.4248$.

F. Present Experiment

We report here measurements of the drag on cylinders in axial motion with L/D ranging from 4 to 230 and the drag on disks with L/D ranging from 0.25 to 0.019 moving parallel to their axes of rotational symmetry. The influence of the top and bottom boundaries is assumed to be negligible. The effect of the cylindrical sidewall is taken into account by an empirical correlation.

CHAPTER 2

THE EXPERIMENT

A. Method of Measurement

Terminal velocity measurements were made using time of flight techniques. Velocities for the disks were obtained by measuring photoelectrically the time of fall between two focused laser beams. The experiments on disks were performed in a glass walled tank (disk tank) of square cross section (25.7 cm x 25.7 cm) and height 51 cm filled to a depth of 48 cm with silicone fluid. Velocities for the cylinders were obtained by measuring manually the time of fall between markers taped to the glass walls of a tank (cylinder tank) of square cross section (30.5 cm x 30.5 cm) and height 61 cm. The level of the fluid in the tank was 49 cm.

B. Materials

1. Boundaries. Pyrex glass tubing was used to obtain boundaries of circular cross section with height 47.7 cm and inside diameters of 13.32, 8.955, 4.32 and 2.18 cm. A larger boundary of inside diameter 21.25 cm and height 45.6 cm was made from polycarbonate (Lexan plastic) tubing. This polycarbonate boundary was found to be slightly tapered with inside diameter 21.65, 21.25 and 20.90 cm at the top,

middle and bottom of the boundary, respectively. The largest boundary of inside diameter 23.6 cm and height 48.6 cm, was made from a thin sheet of fiberglass curved to form a cylinder.

2. Cylinders and Disks. The thirty-two cylinders used were fashioned from four sources: 21A, 24B, 25B and 30A were made from precision stainless steel shafting. Cylinders 17A, 18A, 21B, 21D, 22B, 25D, 27D, 38A and 46A were made from steel KO (knockout) pins. Cylinders 19B, 22A, 22C, 24A, 25A, 25C, 26A, 27A, 27B, 27C, 32A and 34A were made from steel drill blanks (American Standard Twist Drill numbers 61, 65, 70, 75 and 80). Rods 34B, 36A, 41A and 49A were made of acrylic plastic (polymethyl methacrylate, trade name Plexiglas or Lucite). The ends of the steel cylinders were ground flat and perpendicular to the axis. Disks A, B, C and I were made of aluminum and disks G, J and H were made of acrylic plastic. The diameter of each disk and the length of each cylinder were measured to ±0.0036 mm with a traveling microscope. The diameter of each cylinder and the thickness of each disk were measured to ± 0.0025 mm with a micrometer caliper. The steel cylinders ranged in length from 0.384 to 10.98 cm and in diameter from 0.0396 to 0.0987 cm, with $4.21 < L/D < 231$. The acrylic rods were cut from the same rod of diameter 0.338 cm, with $3.74 < L/D < 9.37$. These rods were of circular

cross section but the diameter varied as the point of measurement was changed. The diameter measurements are listed in Table III, in order of measurement from one end of a cylinder to the other end. The standard deviation ranged from 0.3 percent for 41A to 0.9 percent for 36A. The disks ranged in diameter from 1.023 to 2.692 cm and in thickness from 0.0206 to 0.3023 cm with $0.019 < L/D < 0.259$. The experimental parameters of the cylinders are given in Table IV and the disks in Table V.

When an object falls at its terminal velocity, the drag force is equal to the difference between the weight of the object and the buoyant force of the fluid on the object. This effective weight W' was determined as the product of the effective mass and the local gravitational acceleration g (979.35 cm^2/sec). Measurements of the effective mass were made using a Sartorius 2400 analytical balance accurate to ±0.0001 g. The accuracy of each measurement was ±0.0002 g since the effective mass of the thin wire carriage used to suspend the cylinders and disks in the fluid also had to be measured. The carriage was made out of thin tungsten wire of diameter 0.01829 cm and shaped in the form of a ring of outside diameter 0.94 cm connected to three wires which were joined to a single wire. There was a loop at the top of the carriage which was used to suspend the assembly from the top of the scale pan. Before each measurement, the balance was set at 0.0000 g using

TABLE III

DIAMETER MEASUREMENTS OF ACRYLIC CYLINDERS

CYLINDER	D(CM)	$D_{AVERAGE}$ (CM)	STANDARD DEVIATION (%)
34B	0.3386 0.3404 0.3386 0.3399 0.3366 0.3327	0.3378	0.8
36A	0.3304 0.3299 0.3322 0.3345 0.3367	0.3327	0.9
41A	0.3388 0.3378 0.3363 0.3383	0.3378	0.3
49A	0.3399 0.3386 0.3365	0.3383	0.5

TABLE IV

EXPERIMENTAL PARAMETERS OF THE CYLINDERS

CYLINDER	L(CM)	D(CM)	L/D	ε	W_{AIR}(DYNES)	W'(DYNES)	W'_{CAL}(DYNES)	$\frac{W'_{CAL}-W'}{W'_{CAL}} \times 100$
16A	9.134	0.03962	230.5	0.1630	90.39	79.72	79.82	+0.13
17A	10.978	0.06375	172.2	0.1712	278.7	243.9	245.6	+0.69
18A	7.816	0.06384	122.4	0.1818	198.6	174.0	175.0	+0.57
19B	5.944	0.07925	75.00	0.1996	225.6	197.9	197.9	0.00
21D	2.276	0.03988	51.07	0.2111	22.43	19.78	19.78	0.00
21C	2.261	0.04522	50.00	0.2171	28.60	25.07	25.17	+0.40
21B	3.233	0.06477	49.92	0.2172	81.87	71.39	71.79	+0.56
21A	3.840	0.07899	48.61	0.2185	145.4	127.0	127.6	+0.47
22A	3.846	0.08827	43.57	0.2238	185.9	163.5	163.7	+0.12
22C	4.206	0.09868	42.62	0.2249	250.9	220.6	220.6	0.00
22B	2.703	0.06401	42.23	0.2254	68.65	60.13	60.43	+0.50
23A	2.426	0.07036	34.48	0.2362	72.96	64.05	64.05	0.00
24B	2.525	0.07925	31.86	0.2407	95.88	83.73	84.13	+0.48
24A	2.431	0.08814	27.58	0.2494	117.3	102.8	103.3	+0.48
25C	1.819	0.07092	25.65	0.2540	55.14	48.38	48.38	0.00

TABLE IV (cont'd)

25D	1.613	0.06401	25.20	0.2551	40.64	35.65	35.72	+0.20
25B	1.980	0.07874	25.15	0.2552	74.53	65.22	65.32	+0.15
25A	2.456	0.09804	25.05	0.2555	143.6	125.9	126.1	+0.16
26A	2.032	0.08839	22.99	0.2612	98.33	86.67	86.67	0.00
27B	1.750	0.08839	19.80	0.2718	84.22	74.23	74.14	-0.12
27A	1.920	0.09804	19.58	0.2726	113.4	99.50	99.70	+0.20
27C	1.292	0.07087	18.23	0.2781	38.98	34.08	34.18	+0.29
27D	1.153	0.06375	18.09	0.2787	29.28	25.85	25.85	0.00
30A	1.060	0.07925	13.38	0.3043	39.96	34.86	35.06	+0.57
32A	1.080	0.09804	11.02	0.3234	63.46	55.63	55.63	0.00
34A	0.8346	0.08814	9.469	0.3400	40.06	35.16	35.26	+0.28
34B	3.165	0.3378	9.369	0.3412	326.6	58.57	58.57	0.00
36A	2.540	0.3327	7.635	0.3669	253.4	44.76	44.95	+0.42
38A	0.5969	0.09093	6.564	0.3884	29.87	26.05	26.25	+0.76
41A	1.909	0.3378	5.651	0.4124	197.2	35.35	35.75	+0.56
46A	0.3835	0.09093	4.218	0.4690	19.20	16.75	16.84	+0.53
49A	1.265	0.3383	3.739	0.4970	130.9	23.41	23.70	+1.22

TABLE V

EXPERIMENTAL PARAMETERS OF THE DISKS

DISK	L(CM)	D(CM)	L/D	W_{AIR}(DYNES)	W'(DYNES)	W'_{CAL}(DYNES)	$\frac{W'_{CAL}-W'}{W'_{CAL}} \times 100$
A	0.2550	1.018	0.2505	548.4	352.1	351.0	- 0.28
B	0.1900	1.018	0.1866	406.7	260.8	259.6	- 0.46
C	0.1278	1.021	0.1252	275.0	176.5	175.5	-0.57
G	0.3023	1.905	0.1587	1004	184.7	185.0	+0.16
H	0.1460	1.900	0.0768	483.5	90.49	90.79	+0.33
I	0.0523	2.692	0.0194	791.2	511.7	508.6	-0.61
J	0.0688	2.690	0.0256	452.9	81.48	81.29	-0.23

the zero control knob with only the wire carriage immersed in the fluid. The effective mass readings are dependent on the density of the fluid,which varies with the temperature. Therefore, the fluid was allowed to reach its equilibrium temperature. The zero setting of the balance was periodically adjusted. The fluid was considered to have reached equilibrium when no zero adjustment was necessary for fifteen minutes. The cylinder or disk was then lowered carefully into the fluid with plastic tipped tweezers and allowed to float onto the carriage. A reading was taken only after observing that no bubbles clung to the surface of the carriage and the object being weighed. The disks were positioned at an angle on the carriage so that bubbles could float to the free surface of the fluid instead of being trapped on their undersides. Extreme caution was necessary when weighing acrylic cylinders and disks since bubbles formed easily when acrylic objects were immersed. Care was taken to remove static charge from the acrylic material by breathing on them before each measurement. The balance was turned off and the object was removed very carefully using the plastic tipped tweezers. The balance was turned on and the zero reading was checked. If the balance reading was not 0.0000 g, the zero was adjusted and the weighing process was repeated. The process of zeroing the balance and weighing the cylinder or disk was repeated until the mass reading was reproducible. The temperature

of the fluid was taken with a mercury in-glass thermometer after each measurement of the effective mass. Due to the sensitivity of the balance to physical disturbances, a successful measurement required typically three trials over a period of two hours. For the cylinders as shown in Table IV the measured effective weight W' was generally less (by approximately 0.4 percent) than the calculated effective weight W'_{CAL} given by the following equation

$$W'_{CAL} = (\sigma - \rho)V g \qquad (2.1)$$

where σ is the density of the object, ρ is the density of the fluid and V is the volume of the object. The weight of each object is known to ±0.0002 g x 979.35 cm/s² = ±0.2 dynes. Similar observations were reported by Huner and Stalnaker for cylinders and by Amarakoon for rings. For the aluminum disks A, B, C and I, as shown in Table III, the measured effective weight was greater (by approximately 0.5 percent) than the calculated effective weight, whereas for the acrylic disks G and H the measured effective weight was less (by approximately 0.5 percent) than the calculated effective weight. The measured effective weight for disk J was greater than the calculated value by 0.2 percent.

3. Tanks. The tank used for disks was the same tank used by Amarakoon.[51] The tank used for cylinders was made entirely of glass panels of thickness 0.64 cm. The base has dimensions 31.75 cm x 31.75 cm and the sides 60.96 cm x 31.12 cm. The side panels were sealed together two at a time before being glued on to the base. A T-square was used to ensure the joints formed at 90 degrees. Sealant was applied along the edges, inside and outside the tank, to make certain the tank was leak-free. Two sealants were tested. Initially, Dow Corning Silastic RTV Adhesive/Sealant was used. The sealant became soft and a leak developed approximately 2 months after the fluid was poured into the tank. No such leak has occurred in the 27 months after the second sealant, Dow Corning Silicone Adhesive/Sealant was substituted.

4. Fluids. The fluid used for the disks was obtained by mixing silicone liquid of kinematic viscosity 10 cm^2/sec (approximately 55 percent by volume) with silicone liquid of kinematic viscosity 125 cm^2/sec. The viscosity of the mixture was measured by Amarakoon with a Cannon-Fenske routine type viscometer No. 502 (size 500) immersed in a controlled temperature bath over a temperature range of 19° to 28°C. The reproducibility of the measurements was 0.1 percent or better. The density of the fluid was determined over the same temperature range by measuring

the buoyant force on a pyrex glass plummet (of volume 1.556 cm^3).

The fluid used for the cylinders was obtained by mixing silicone liquid of kinematic viscosity 10 cm^2/sec (approximately 48 percent by volume) with silicone liquid of kinematic viscosity 125 cm^2/sec. The viscosity of the fluid was measured with a Cannon-Fenske routine type viscometer No. 502 (size 500) or a Cannon-Ubbelohde viscometer No. 500 (A702) immersed in a controlled temperature bath over the temperature range 20° to 27°C. The routine type viscometer must be charged with a precise amount of fluid whereas the amount of fluid poured into the Ubbelohde viscometer need only fall within a certain range. The reproducibility of the measurements was about 0.07 percent. The absolute viscosity is known only to 0.25 percent, because of uncertainty in the standard of viscosity (0.01002 g/(cm·sec)) for the dynamic viscosity $\mu = \nu\rho$ of water at 20°C and one atmosphere pressure). The fluid density was measured over the same temperature range by measuring the buoyant force on a brass rod of length 4.855 cm, diameter 0.7940 cm and mass in air 20.3521 g.

5. Variation of Viscosity With Time

The viscosity of both liquids increased with time (see Fig. 2.1). The viscosity at 24° C is plotted against time in months (1 month = 30 days). As shown in Fig. 2.1, the approach to a steady value was approximately exponential with an e-folding time of 1 month for the liquid used for the cylinders compared a time of 7 months for the liquid used for the disks (see Fig. 2.2). In Fig. 2.2, $-\ell n[(\nu_s-\nu_2)/(\nu_s-\nu_1)]$ is plotted versus time, where ν_s is the steady, final value of the viscosity approached as the time $t \to \infty$, ν_2 is the viscosity at time t, and ν_1 is the viscosity at time t = 0. The reference date t = 0, for the disk liquid is February 15, 1980. The tank used for the disks was filled on December 31, 1979. The reference date for the cylinder liquid is March 31, 1981. The tank was filled on January 20, 1981. The more rapid approach to a steady value for the liquid used for the cylinders was achieved by pouring the 10 cm^2/sec and 125 cm^2/sec liquids into the tank alternatively in thin layers rather than adding one liquid in bulk to the other before stirring. Additional mixing occurred because of the following sequence of events. A leak in the cylinder tank was observed on March 13, 1981. The cylinder fluid was transferred back into the original drum cans which still contained small amounts (approximately 0.3 liter)

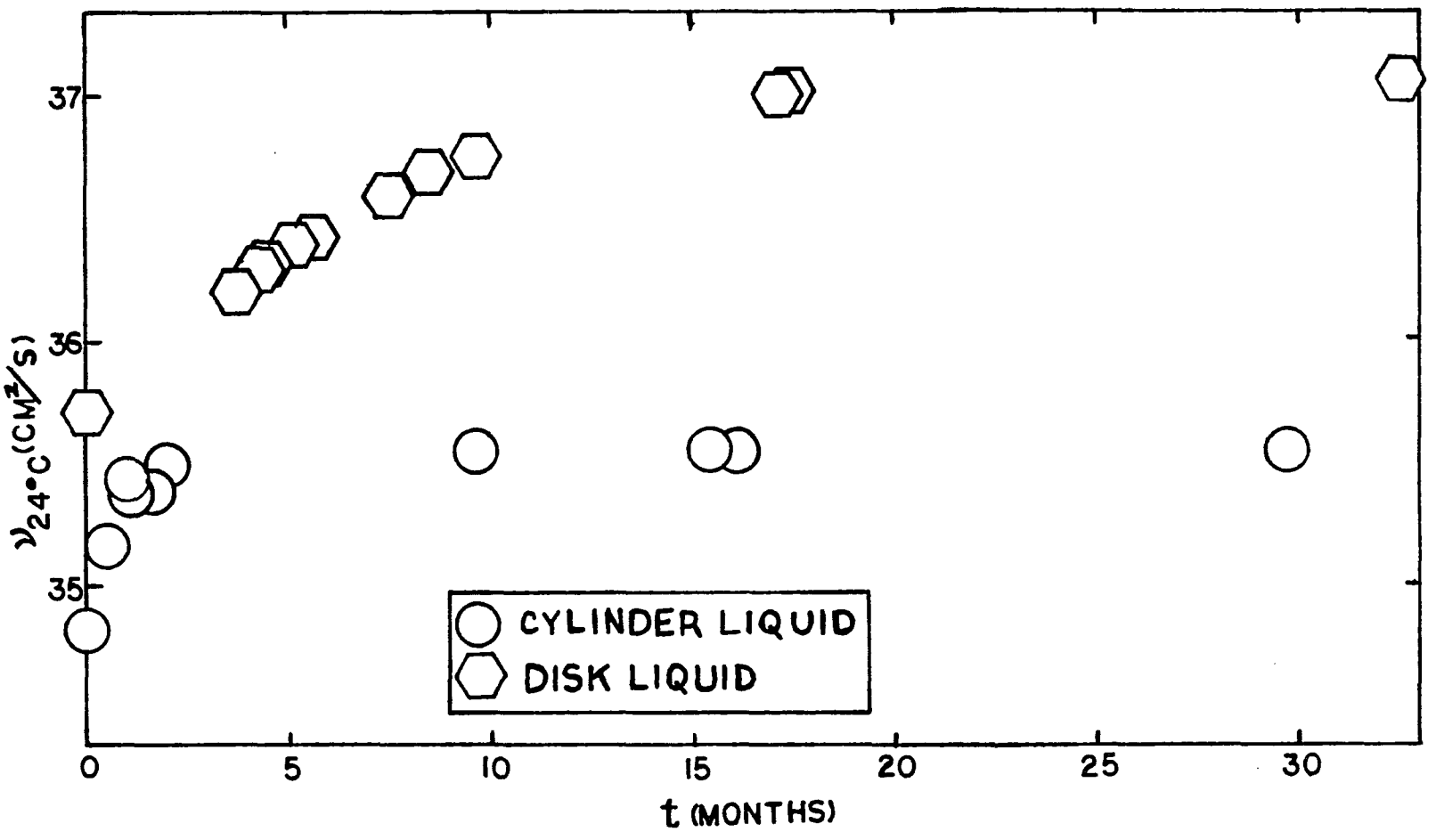

Fig. 2.1 THE KINEMATIC VISCOSITY ν AT 24°C VS. TIME.

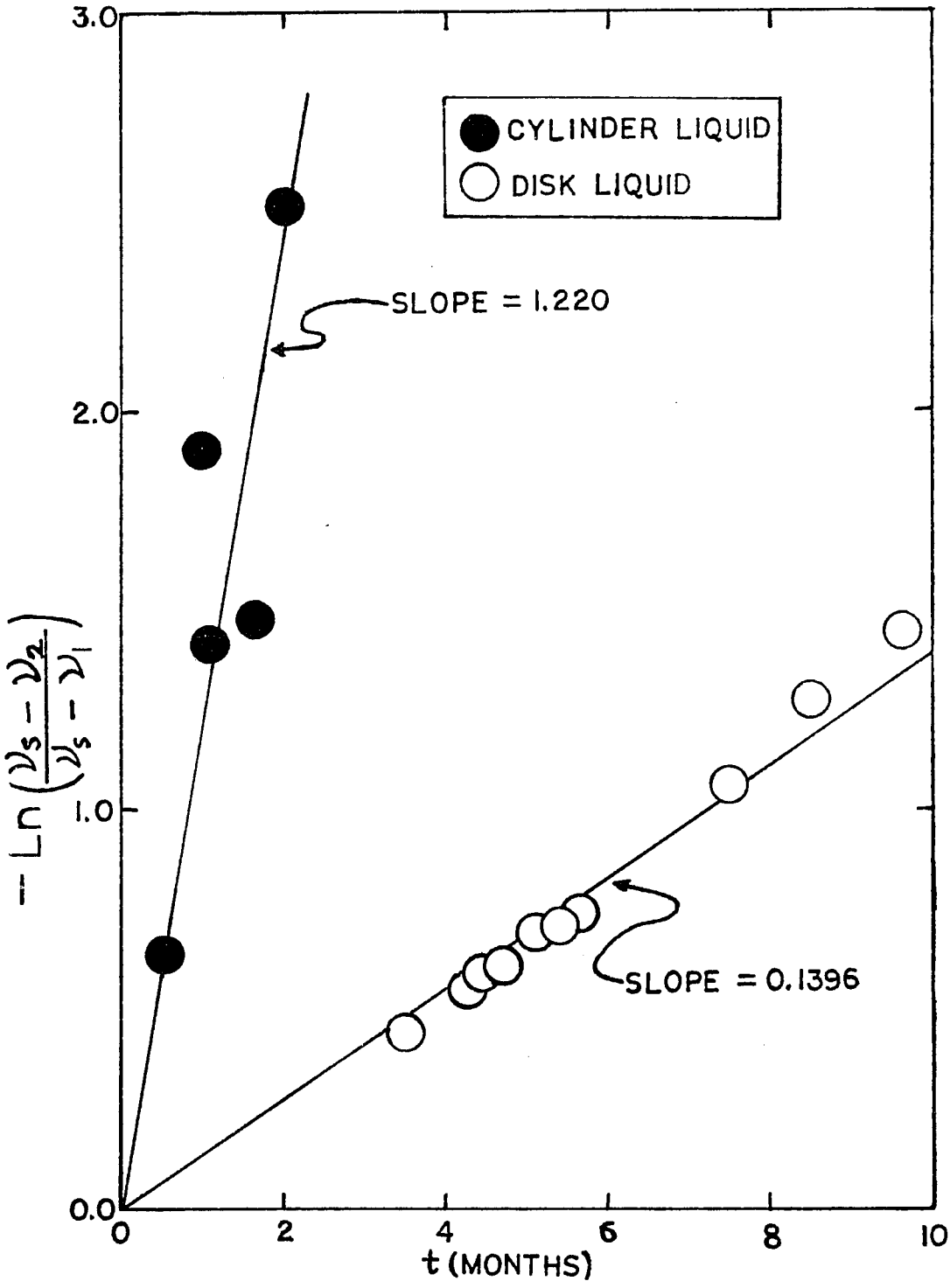

Fig. 2.2 CALCULATION OF e-FOLDING TIMES.

of the 10 cm^2/sec and 125 cm^2/sec liquids. The tank was dismantled and reconstructed. Viscosity measurements were made on March 31, 1981.

The disks were released in the liquid for which the density and viscosity are represented by the equations

$$\rho = 0.9708\ [1 + 8.02 \times 10^{-4}(24-T)]g/cm^3 \qquad (2.2)$$

and

$$\nu = 37.04\ [1 + 1.973 \times 10^{-2}(24-T)]cm^2/sec \qquad (2.3)$$

where T is the temperature in °C. The majority of the cylinder drops were made from February 24, 1981 to July 2, 1981 when the fluid viscosity was changing. The data were adjusted according to the exponential dependence. Cylinders 18A, 21A, 21B, 21C, 21D, 22A, 22B, 22C, 24A, 25A, 25B, 25C, 25D, 26A, 27A, 27B, 27C and 27D were released in the boundary of diameter H = 21.25 cm between February 24, 1981 and March 2, 1981, before the leak in the tank occurred. The viscosity of the fluid as of March 1, 1981, used for these cylinders is given by

$$\nu = 34.63\ [1 + 1.899 \times 10^{-2}(24-T)]cm^2/sec \qquad (2.4)$$

where T is the temperature in °C. The density and viscosity

of the stable fluid are given by

$$\rho = 0.9653\ [1 + 1.1596 \times 10^{-3}(24-T)]\ g/cm^3 \qquad (2.5)$$

and

$$\nu = 35.54\ [1 + 1.976 \times 10^{-2}(24-T)]\ cm^2/sec\ . \qquad (2.6)$$

C. Test for Newtonian Character of Fluids

Silicone fluids were chosen for the present experiment because they have low temperature coefficients of viscosity, are reasonably stable with respect to time, and are Newtonian[52] up to fairly high values of the dynamic viscosity (about 3.1 g/cm·s) if the rate of shear is low (less than 60 s^{-1}). The Newtonian character of the disk and cylinder fluids was examined by measuring terminal velocities of spheres. Steel spheres of diameter 0.3163 and 0.5551 cm were released by Amarakoon in the disk fluid. When corrections for the influence of inertia and finite boundaries were applied,[47] the viscosities calculated from the velocity measurements for the two spheres agreed to within 0.5% with the capillary viscometer measurements. The shear rates ranged from 2.9 s^{-1} for the capillary to 17 s^{-1} for the larger sphere. A steel sphere of diameter 0.4763 cm and a teflon sphere of diameter 0.7938 cm were released in the fluid used for the cylinders. The data are listed in Tables VI(a) and VI(b). Res is the Reynolds number $(UD\rho)/\mu_s$. μ_s is equal to $D^2(\sigma-\rho)g/(18U)$, where σ is the density of the sphere and ρ is the density of the fluid. μ was calculated by using Equations (2.4) and (2.5). When inertial and finite boundary corrections were applied by using Sutterby's factor K, the viscosity for the steel sphere was greater by approximately 0.46% in two trials and less by approximately 0.33% in three trials, than the

TABLE VI(a)

DATA FOR SPHERES RELEASED IN THE CYLINDER
FLUID IN THE BOUNDARY OF DIAMETER H = 21.25 cm

SPHERE	TRIAL	D(cm)	D/H	U(cm/sec)	Mass(g)	$3U/D(sec^{-1})$
Steel	1	0.4763	0.0224	2.364	0.4387	14.9
	2			2.347		14.8
	3			2.336		14.7
	4			2.358		14.9
	5			2.331		14.7
Teflon	1	0.7938	0.0374	1.097	0.5595	4.15
	2			1.082		4.09
	3			1.104		4.17

TABLE VI(b)

μ, μ_s and μ' in g/cm·sec

SPHERE	TRIAL	Res	μ_s	μ	K	$\mu'=\mu_s/K$	$\frac{\mu'-\mu}{\mu} \times 100$
Steel	1	0.0321	35.45	33.84	1.0514	33.72	-0.35
	2	0.0319	35.70	33.82	1.0513	33.96	+0.41
	3	0.0316	35.87	33.95	1.0513	34.12	+0.50
	4	0.0319	35.54	33.95	1.0513	33.81	-0.41
	5	0.0313	35.95	34.27	1.0513	34.19	-0.23
Teflon	1	0.0223	37.11	34.02	1.0859	34.17	+0.44
	2	0.0229	36.62	33.98	1.0859	39.72	-0.77
	3	0.0232	36.39	33.84	1.0859	3.51	-0.98

capillary viscometer measurements. The viscosity calculated for the teflon sphere was greater by 0.44% and less by 0.77 and 0.98 percent than the capillary viscometer measurements. The shear rates for the spheres, given by Sutterby's expression 3U/D, ranged from 4.09 s^{-1} for the teflon sphere to 14.9 s^{-1} for the steel sphere. The shear rate for the capillary was 2.2 s^{-1}. The shear rate for the capillary was calculated using the expression $(4Q)/(\pi tR^3)$, which follows from Poiseuille's equation for fluid flow (Ref. Schlichting p. 86).[6] Q is the volume of fluid flow in time t and R is the radius of the capillary. Values of the correction factor K, were calculated by using Table IX of Amarakoon's dissertation (reproduced here as Table VII). The results of Sutterby were found (by Amarakoon) to be well represented by relations of the form

$$K = A(Res)^n + K_o \text{ , for a given } D/H \tag{2.7}$$

and

$$K = B(D/H)^m + K_o \text{ ,} \tag{2.8}$$

for a given value of Res $\neq$ 0. For the present calculations, A and K_o were evaluated by applying Eq. (2.6) to each unique pair of Res for a given D/H and solving the corresponding simultaneous equation. The average of these

TABLE VII

SUTTERBY'S VALUES OF K FOR SPHERES (TABLE IX OF AMARAKOON'S DISSERTATION)

D/H	Res	0.0	0.2	0.4	0.6	0.8	1.0	n
0.00		1.0000	1.0331	1.0639	1.0941	1.1241	1.1519	0.947
0.01		1.0215	1.0423	1.0706	1.0980	1.1251	1.1570	1.106
0.02		1.0439	1.0559	1.0792	1.1050	1.1303	1.1661	1.307
0.03		1.0673	1.0748	1.0919	1.1157	1.1409	1.1661	1.515
0.04		1.0917	1.0970	1.1100	1.1311	1.1550	1.1795	1.678
0.05		1.1172	1.1213	1.1321	1.1500	1.1720	1.1950	1.772
0.06		1.1439	1.1473	1.1556	1.1700	1.1903	1.2121	1.888
0.07		1.1717	1.1751	1.1803	1.1923	1.2100	1.2300	1.979
0.08		1.2008	1.2031	1.2074	1.2161	1.2311	1.2500	2.158
0.09		1.2313	1.2338	1.2380	1.2460	1.2582	1.2752	2.018
0.10		1.2631	1.2660	1.2709	1.2783	1.2900	1.3055	1.848
0.11		1.2964	1.2996	1.3041	1.3117	1.3230	1.3373	1.778
0.12		1.3313	1.3345	1.3391	1.3463	1.3571	1.3700	1.712
0.13		1.3679	1.3709	1.3754	1.3823	1.3920	1.4034	1.661
m			1.413	1.601	1.743	1.863	1.912	

results for D/H equal to 0.01, 0.02, 0.03 and 0.04 are given Table VIII(a). The agreement between Sutterby's values of K and those calculated by using the data given in Table VIII(a) and Eq. (2.7) is better than 0.34%. These results were used to calculate K for the Res obtained for the spheres (see Table VIII(b)). The results listed in Table VIII(b) are represented well by the equation,

$$K = 3.285(D/H)^{1.132} + 1.0063 \qquad (2.9)$$

for the teflon sphere. The data for the steel spheres are represented well by the equations

$$K = 3.458(D/H)^{1.154} + 1.0082 \qquad (2.10)$$

for trial one,

$$K = 3.370(D/H)^{1.145} + 1.0078 \qquad (2.11)$$

for trials two and four, and by

$$K = 3.396(D/H)^{1.148} + 1.0079 \qquad (2.12)$$

for trials three and five.

TABLE VIII(a)

SLOPE AND INTERCEPT FOR THE EQUATION

$$K = A(Res)^{n} + K_{o}$$

D/H	n*	A	K_o
0.01	1.06	.1328	1.0222
0.02	1.307	.1161	1.0448
0.03	1.515	.1019	1.0679
0.04	1.678	.09031	1.0922

*The exponents n are those listed in Table VII.

TABLE VIII(b)

K GENERATED USING THE RESULTS OF TABLE VIII(a)

D/H	Res	0.0223	0.0229	0.0232	0.0313	0.0316	0.0319	0.0321
0.01		1.0242	1.0242	1.0243	1.0251	1.0251	1.0252	1.0252
0.02		1.0456	1.0456	1.0456	1.0461	1.0461	1.0461	1.0461
0.03		1.0682	1.0682	1.0682	1.0684	1.0684	1.0685	1.0685
0.04		1.0424	1.0924	1.0924	1.0925	1.0925	1.0925	1.0925

Youngren and Acrivos have shown that the viscous stress force and hence the shear rate is sharply peaked at the corner of a cylinder where the curved surface meets the flat end surfaces. Similar results have been obtained by Roger[56] with his beads-on-a-shell model calculations as shown in Fig. 2.3. The normalized stress force is plotted for a cylinder of L/D = 1 as one proceeds from the center of an end face (s = 0) around the corner (s = 1) to a point halfway up the curved surface (s = 2). For further details, see Chapter 3. For a mathematically sharp edge, the shear rate is infinite[62] and the fluid non-Newtonian. The shear rate is finite for real objects since real objects have slightly rounded edges.[63] For the present case, the radius of curvature r at a corner was typically 0.001 cm for the cylinders and less than 0.001 cm for the disks. The radii of curvature were measured by comparing the objects with a scale (200 divisions per 2 mm) under a Unitron 73141 microscope.

Estimates of the shear rates at the corner of cylinders and disks may be calculated as follows. An examination of the flow pattern near the corner of a cylinder (Fig. 2.4(a)) suggests that a reasonable estimate for the lower bound for the shear rate may be

$$SR_1 = (U/r)/(L/D) \ , \qquad (2.13)$$

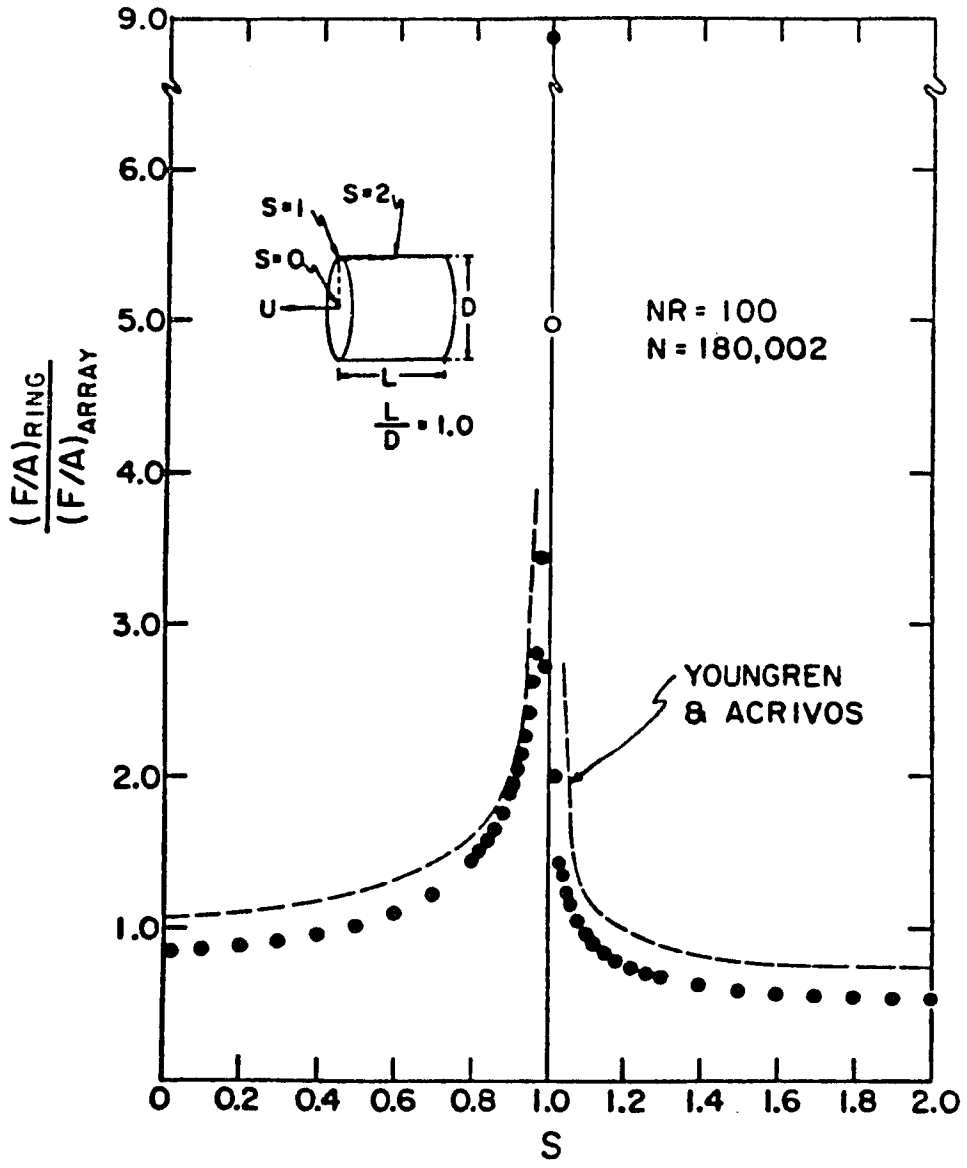

Fig. 2.3 Variation of the axial stress force with position on the cylinder. N is the total number of beads and NR is the number of rings of beads.

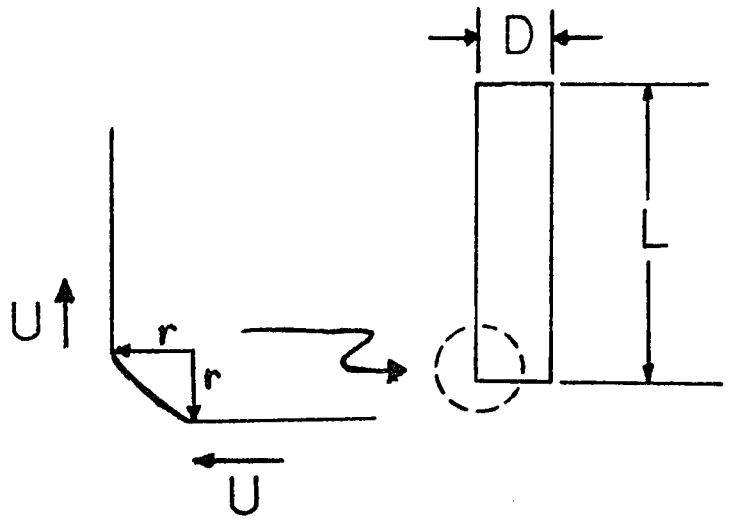

Fig. 2.4(a) FLOW PATTERN NEAR THE CORNER OF A CYLINDER WITH RADIUS OF CURVATURE r.

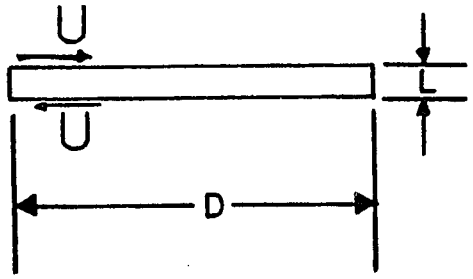

Fig. 2.4(b) FLOW PATTERN NEAR THE EDGE OF A DISK.

since one would expect the effect on the total drag at the corner to diminish in comparison to that at the curved surfaces as L/D increases. For disk-like objects (Fig. 2.4(b)), the change in fluid velocity 2U occurs over a distance L, where L is the thickness of the disk. The shear rate in this case may be approximated by

$$SR_2 = 2U/L \ . \tag{2.14}$$

Another estimate for the lower bound may be calculated by using Roger's results for the stress force along the surface of a cylinder (see Fig. 2.3). This expression is given by

$$SR_3 = \frac{8.9}{\mu} \frac{DRAG}{SA} = \frac{8.9}{\mu} \frac{m'g}{2(\frac{\pi D^2}{4}) + \pi DL} \ , \tag{2.15}$$

where μ is the viscosity of the fluid, SA is the total surface area of the body and 8.9 is the normalized stress force at the corner of a cylinder with L/D = 1. The results of these three approaches are tabulated in Table IX, for cylinders 21A and 18A and for disks A and I. The values of the viscosity given are those at T = 24° C. Values of the velocity U were taken from measurements made in the largest boundaries H = 21.25 cm for the cylinders and H = 23.6 cm for the disks. All estimates of the lower bound of the shear rate are less than 60 s^{-1}, which suggests

that the fluid may be Newtonian. However, if the flow is non-Newtonian, we expect the contribution to the total drag to be negligible since this effect occurs over a very small area.

TABLE IX

ESTIMATES OF THE LOWER BOUND FOR THE SHEAR RATE
AT THE EDGE OF A CYLINDER OR DISK

OBJECT	L(cm)	D(cm)	U(cm/s)	μ(g/s·cm)	m'g(DYNES)	$SR_1(s^{-1})$	$SR_2(s^{-1})$	$SR_3(s^{-1})$
Cylinder 18A	7.816	0.06384	0.4288	34.31	174.0	3.5		28.7
Cylinder 21A	3.840	0.07899	0.5294	34.31	127.0	10.9		34.2
Disk A	0.2550	1.018	0.9866	35.96	352.1		7.7	35.7
Disk I	0.0523	2.692	0.4969	35.96	511.7		19	10.7

D. Experimental Set Up

1. Timing Method for Disks

The experimental set up used for measuring the velocity of a disk is described in detail by Amarakoon.[51] The velocity was determined by measuring the time of fall between two, parallel focused laser beams, which were directed onto a photodetector. When a disk passed through the upper and lower beams, the resulting blockage of the laser light from the photodetector induced voltage pulses which activated and deactivated a timer-counter (Hewlett-Packard 5326B). The time of fall between the two beams was displayed on the counter to 0.01 msec. The times ranged from 5.3 sec to 103 sec.

The beam separation distance 5.235 ± 0.015 cm was measured using the vertical rack-and-pinion mechanism of a traveling microscope. The measuring process was as follows: A device (approximately 40 cm long) which consisted of a teflon ring (diameter about 4 cm) and a flexible wire (about 30 cm long) connected to the vertex of a carriage (in the shape of an isosceles triangle), was hung from the microscope. The base of the carriage was a horizontal piece of phosphor bronze wire of length 2.5 cm and diameter 0.0403 cm. With the microscope resting on a platform at the top of the tank, the measuring device was lowered carefully into the tank by turning the knob on the rack-and-pinion mechanism of the microscope. When the phosphor

bronze wire was low enough to intercept the upper laser beam, the timer-counter was activated. When the lower beam was intercepted, the timer-counter was deactivated. Care was taken to see that only the phosphor bronze wire intercepted the beam. The difference in the readings of the vernier scale on the traveling microscope, at the points of beam interception was the beam separation distance.

2. Timing Method for Cylinders

The velocity of a cylinder moving parallel to its axis was determined by measuring the time of fall manually with an electric clock (Standard Electric Model S-10) between markers taped to the walls of the cylinder tank. The clock could be read to 0.01 sec. Sighting errors due to parallax were reduced by placing markers at the same levels on opposite faces of the tank. Distances between the markers were measured by employing the same rack-and-pinion mechanism of the traveling microscope used to measure the laser beam separation. The measurements were made down the center of the front and rear side panels in the following way. The top edge of each marker was aligned with the horizontal cross hair of the traveling microscope. The difference between the microscope readings for successive markers gave the distance between the markers. The separation distances are given in Fig. 2.5. The interval over which the timing took place ranged from 4.98 to

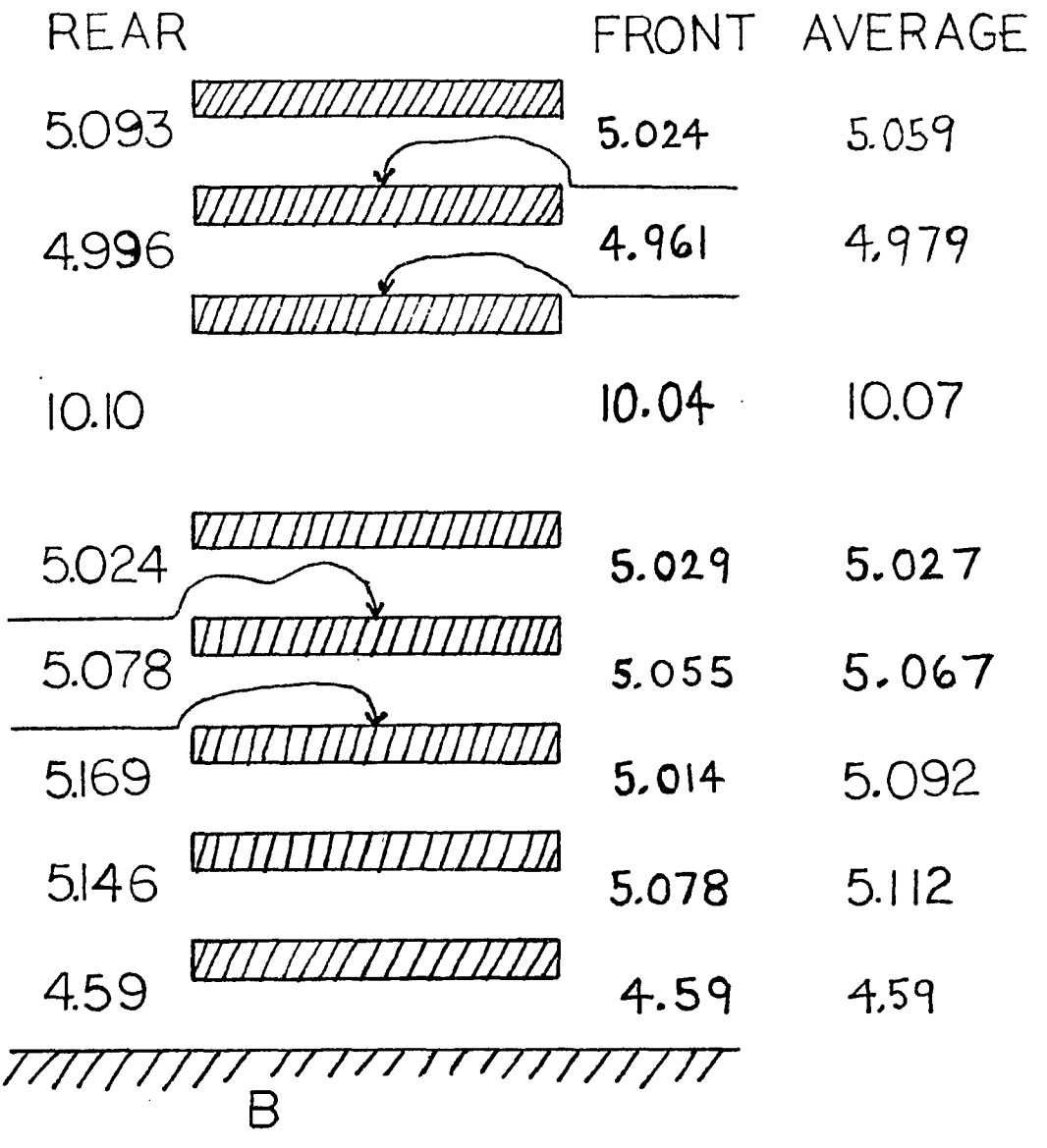

Fig. 2.5 DISTANCES IN CENTIMETERS BETWEEN THE MARKERS ON THE THE TANK USED FOR THE CYLINDERS. MEASUREMENTS WERE MADE DOWN THE CENTER OF EACH SIDE PANEL.

25.14 cm. The times of flight ranged from 12.64 to 224.02 sec. The average of the front and rear measurements was taken to be the interval distance. In order to ensure that this average of the measurements represented accurately the distance traveled by the cylinders, care was taken to place each boundary in the center of the tank in the following way. Two strings weighted at the ends with nuts were placed at 90 degrees to each other and over marks drawn at the midpoint of the top edge of each side panel of the tank. The boundary was then moved so that a similar set of marks drawn on the circumference of the boundary was aligned with the strings.

3. Temperature Dependence of Drag

The velocity measurements for the cylinders and disks were influenced by the change in the dynamic viscosity μ of the fluids due to variation in the temperature (as much as 3° C) when different boundaries were used. This variation in the temperature corresponded to a change in μ of 6.3% for the fluid used for the cylinders and 6.2% for the fluid used for the disks. These variations were taken into account by evaluating the product μU for each object in each boundary. The standard deviation of μU for the disks for at least 3 measurements was typically 0.47% and 0.33% for the cylinders for at least 4 measurements. The effective mass of each object also was influenced by the

variation in the temperature through the temperature dependence of the fluid density. The correction was as much as 0.5% for the disks and for the cylinders. Typically the correction was less than 0.1% and was ignored.

4. Release Device for Disks

The mechanical dropper used to release the disks with their planes horizontal is described by Amarakoon in his dissertation. The dropper was equipped with a bubble level indicator and three leveling screws. A second bubble level was placed at 90° with respect to the first and used to position the dropper so that a disk was released with its plane horizontal. Before releasing each disk (approximately once every 30 minutes), a flexible wire of diameter 0.099 cm was used to sweep away bubbles which had become attached to the bottom surface of the disk. The frequency of successful drops (i.e. disks falling with planes horizontal) using this leveling procedure was about 75%. If the time between drops was shortened to as little as 15 minutes, the success rate dropped to below 40%.

5. Release Device for Cylinders

The cylinders were released from rest manually through a vertical hole drilled in a rectangular acrylic block attached to an acrylic plate. The hole was originally 0.22 cm in diameter but was enlarged to 0.38 cm to accommodate the thick acrylic cylinders (D = 0.338 cm). The plate

was long enough (L = 24 cm) so that the device could be placed on the largest boundary used (H = 21.25 cm) for the cylinders. The dimensions of the release device are given in Fig. 2.6. The hole was centered in a boundary by aligning it with a set of marks placed on the quadrants of each boundary. The release device served as a vertical guide so that a cylinder was coaxial with a boundary at the point of departure. A cylinder with L > 3.2 cm could be visually adjusted while still in the hole so that its path was coaxial with a boundary ($H \geq 4.32$ cm) in over 90% of the trials. A cylinder with L < 3.2 cm tended to go down the guide hole in a tilted position. However, the cylinder drifted back so that it was parallel with the axis of a boundary, as it remained stationary for a moment just before separating from the release device. The rate of successful trials was about 80%. This figure was less than 40% for the acrylic cylinders since bubbles tended to cling to the surfaces of the cylinders. As for the acrylic disks, care was taken to remove static charges from the acrylic cylinders by breathing on them before each measurement. There was no significant improvement in the reproducibility of the measurements as the time between releases was varied from 5 to 30 minutes. It was finally decided to release the cylinders every 15 minutes.

In the smallest boundary (H = 2.18 cm), the rate of successful releases was about 70%. The following behavior

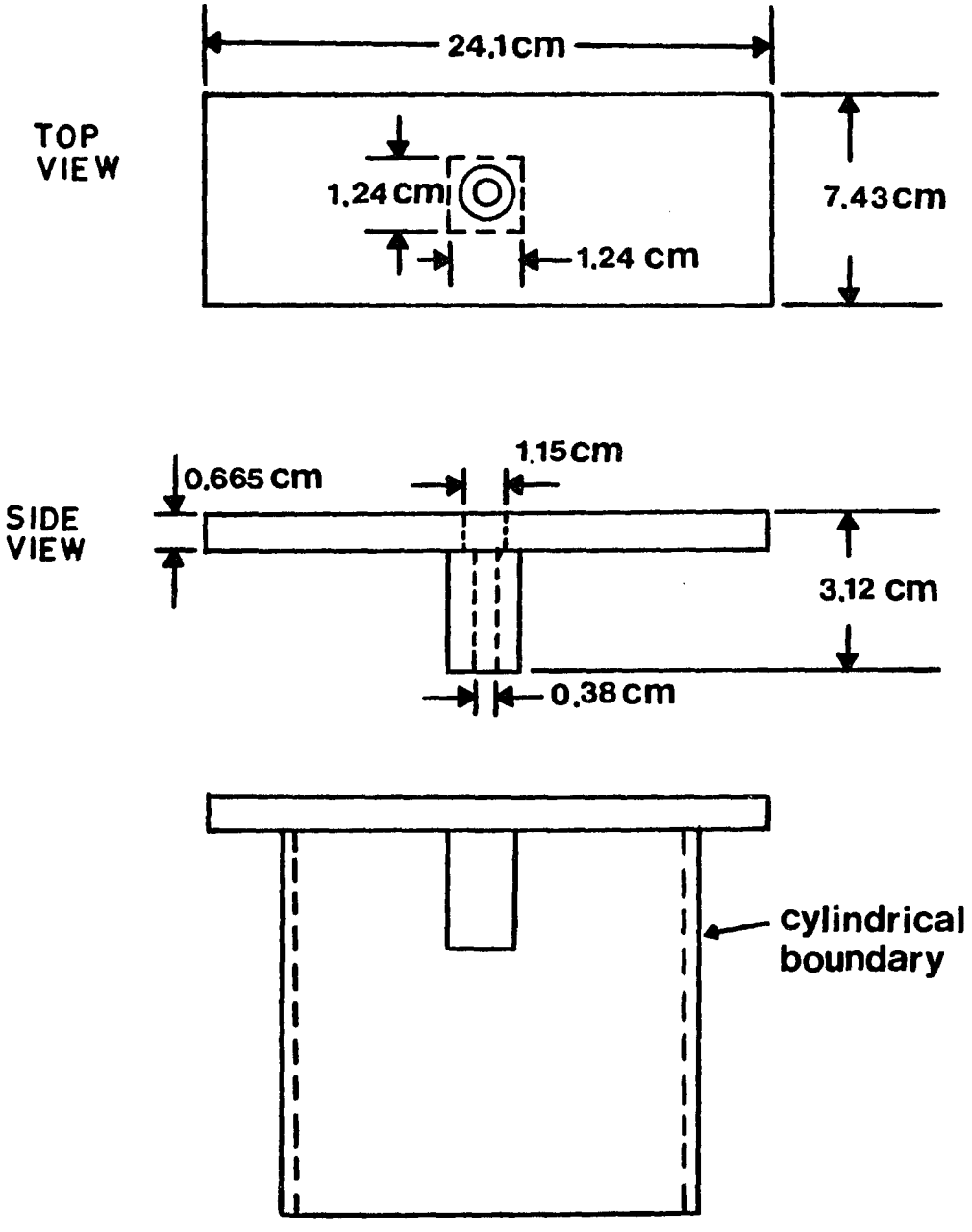

Fig. 2.6 DIMENSIONS OF THE RELEASE DEVICE USED FOR THE LONG CYLINDERS.

was observed for the unsuccessful drops. If a cylinder fell with its axis tilted slightly away from the axis of the boundary at the point of release, it tended to proceed down the tube in the following way: The cylinder drifted laterally in the direction of the leading bottom end. At the wall (boundary) the cylinder turned smoothly through the vertical and drifted away with the same end leading. This glancing turn (cylinder does not touch the wall), similar to that observed by Russel et al.[16] for plane walls, is repeated at the opposite wall and so on such that the cylinder oscillated periodically before coming to rest at the bottom of the boundary. The oscillatory behavior was not observed in the larger boundaries ($H \geq 4.32$ cm).

CHAPTER 3

RESULTS

A. Presentation of Data

The presentation of our data is done as follows: The results for the long and short (disk-like) cylinders are covered in Sections B and C, respectively. The tests for inertial effects are discussed in Section D and effects due to the presence of the bottom boundary are discussed in Section E.

B. Long Cylinders

The most difficult part in the experimental determination of the Stokes drag on an object is the proper assessment of the boundary effect. As discussed earlier in Chapter 1 (Section B-3(d)), there are several theoretical treatments that can be used for guidance. Chang[31] derived an expression for the motion of an axisymmetric object along the axis of a circular cylindrical boundary. His result, applied to the present case, can be written in the form

$$\frac{F}{F_\infty} = 1 + \frac{CF_\infty L}{H} \quad , \tag{1.31}$$

where F_∞ is the dimensionless Stokes drag (made dimension-

less by the factor $2\pi\mu UL$) in a fluid extending to infinity and $C = 1.402$. Brenner[32] has obtained a more general result for non-axisymmetric particles and for outer boundaries of arbitrary shape. The coefficient in Brenner's theory corresponding to C in Eq. (1.31) depends on the shape of the outer boundary but not on the shape of the particle. Wakiya[29] has found the effect of a cylindrical outer boundary on the drag of a spheroid, including terms up to $(L/H)^3$. In the limit $L<<H$ the results of Chang, Brenner and Wakiya are nearly the same, with $C \cong 1.403$ for Brenner and Wakiya, and $C = 1.402$ for Chang.

For the present case (a long cylinder moving lengthwise along the axis of a cylindrical boundary) we have observed that the dimensionless drag ($F = \text{Drag}/2\pi\mu UL$) is a linear function of the inverse of the boundary diameter (1/H). This linear relation, shown in Fig. 3.1, suggests that a linear extrapolation ($1/H \to 0$) will give the Stokes drag for a fluid of infinite extent. As discussed earlier in Chapter 1 (Section 3d), such an extrapolation procedure is suggested by the result of Wakiya[29] (shown as the dashed lines in Fig. 3.1) for a long prolate spheroid. One can see from Fig. 3.1 that as the length to diameter ratio increases, the observed behavior of the cylinder more closely approaches the theoretical result for the spheroid. This is to be expected since the spheroid approximation is best for those cylinders with large length to diameter

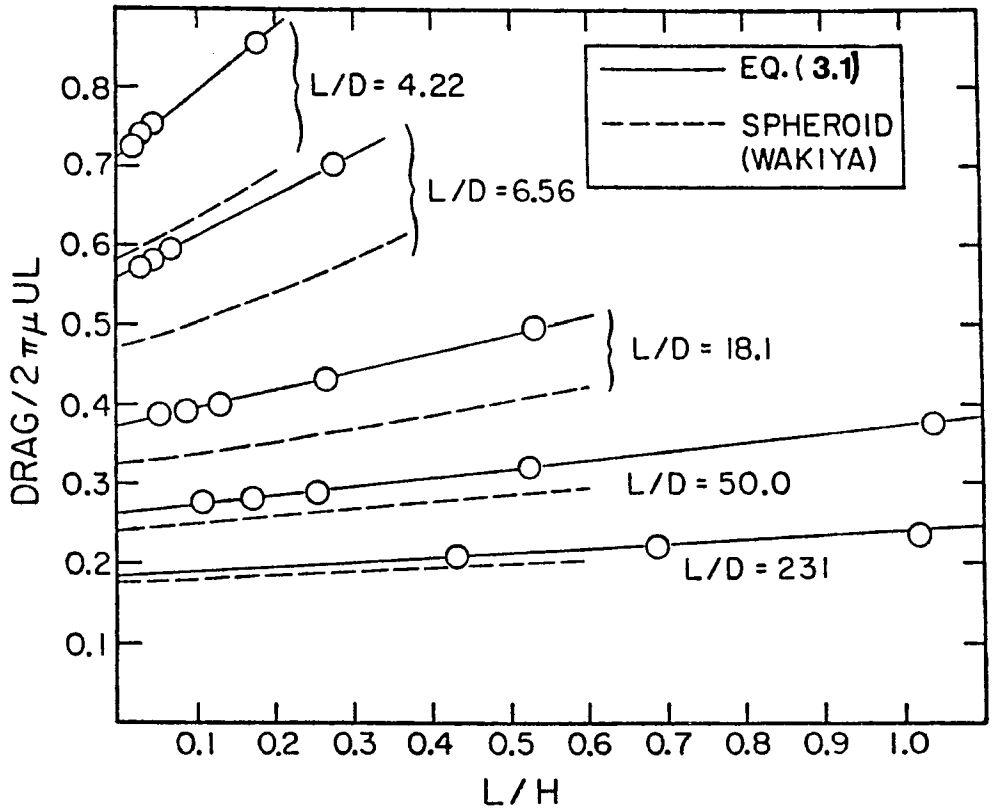

Fig. 3.1 The boundary effect for long cylinders. The solid lines represent our empirical correlation, Eq. (3.1), and the dashed curves represent results derived by Wakiya[29] for the corresponding inscribed prolate spheroids.

ratios. Our measured values can be written in the form of Eq. (1.31) but the coefficient C was found to depend weakly on the ratio L/D and to approach the value 1.403 from above as L/D increases. This behavior can be seen in Fig. 3.2 in which a plot of the coefficient C vs L/D is shown. The final result is:

$$(F/F_\infty) - 1 = CF_\infty L/H$$

with

$$C = 1.60 \pm 0.15 \quad \text{for} \quad L/D < 40$$

and

$$C = 1.403 + (7D/L) \quad \text{for} \quad L/D > 40 \quad . \qquad (3.1)$$

Figure 3.3 is a plot of $(F/F_\infty) - 1$ vs CLF_∞/H for the long cylinders. The experimental points for the steel cylinders are represented by the open circles and the experimental points for the acrylic plastic cylinders are represented by the filled circles. Values of L/H are given beside those points for which $L/H \geq 1.1$. Figure 3.3 shows that Eq. (1.31) is valid when $L/H < 1.2$.

The theoretical treatments of Brenner[32] and Williams[33] for the influence of a boundary on the drag of a particle indicate that the correct expression in that case is

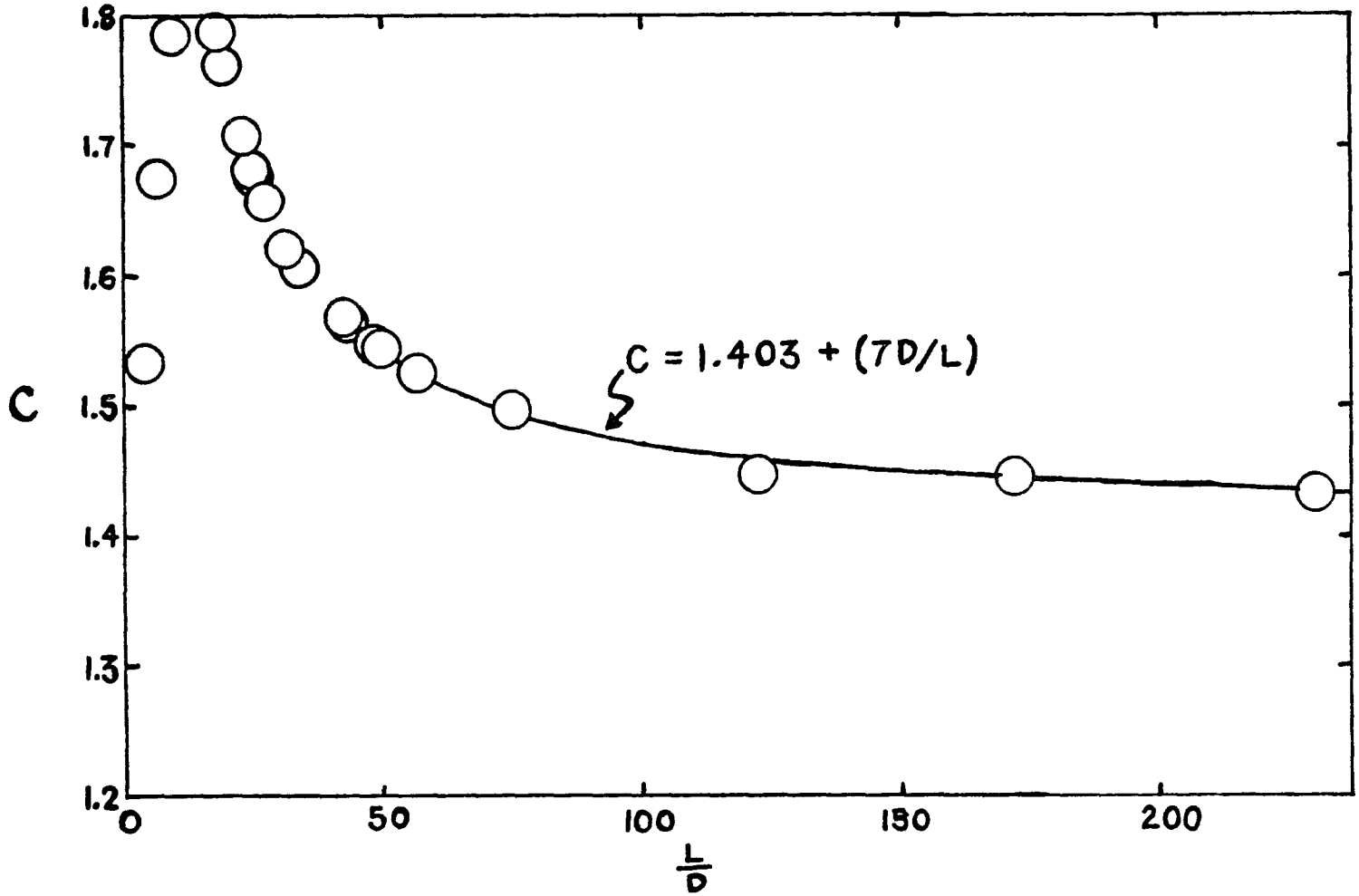

Fig. 3.2 THE DEPENDENCE OF THE SLOPE C ON L/D.

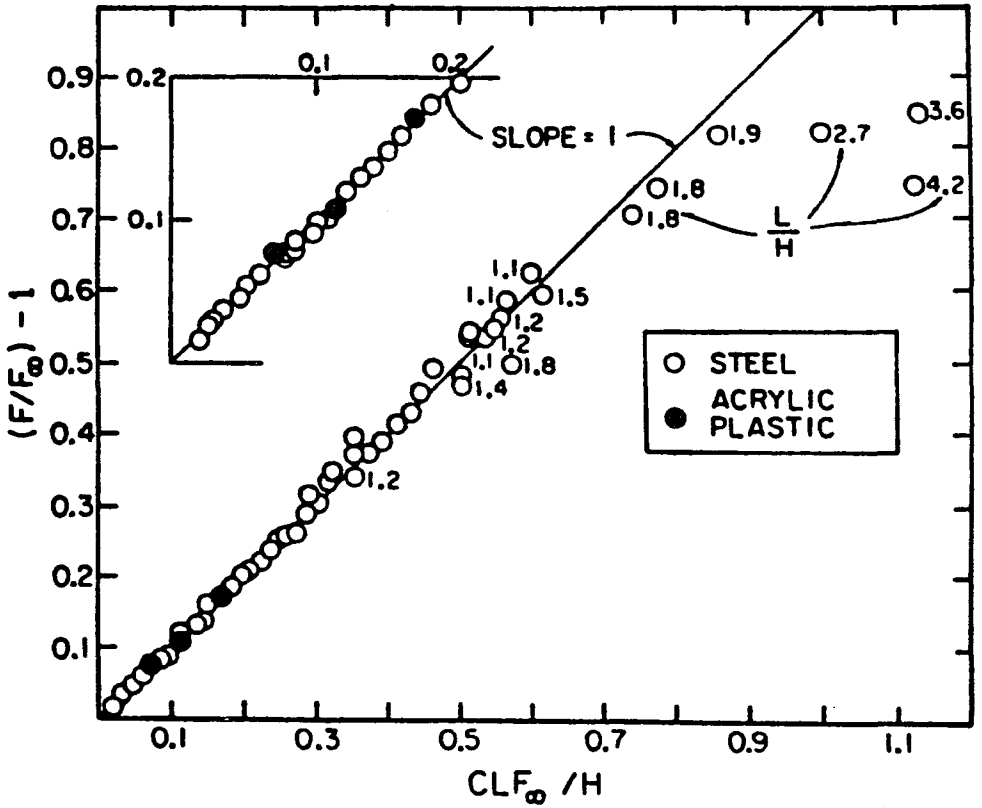

Fig. 3.3 Correlation of the boundary effect data for long cylinders. Values of L/H are given beside those points for which $L/H \geq 1.1$.

$$F/F_\infty = [1 - (CF_\infty L/H) + O(L/H)^3] \ , \qquad (1.32)$$

which implies that a plot of 1/F vs 1/H should be linear over a wider range of H than a plot of F vs 1/H. Our data indicate that for a long cylinder moving axially, an expression in the form of Eq. (1.31) is more appropriate than an expression in the form of Eq. (1.32). This can be seen by comparing Figs. 3.1 and 3.4. More points lie on a straight line when F is plotted vs L/H (Fig. 3.1) than when 1/F is plotted vs L/H (Fig. 3.4). Figure 3.5 shows that the pattern of behavior for the disk-like objects is opposite to that for the long cylinders (i.e. more linear when 1/F is plotted vs D/H than when F is plotted vs D/H).

The same conclusion can be drawn from Wakiya's theory for spheroids. The boundary effect for an oblate spheroid (moving along its minor axis) is more linear when 1/F is plotted vs 1/H, but for a long prolate spheroid (moving along its major axis) it is more linear when F is plotted vs 1/H. A sensitive way of showing this behavior is to display Wakiya's results as deviations from a straight line in the following manner: For oblate spheroids, the two functions

$$\Delta F1 = \frac{(F/F_\infty - 1)_{SL} - (F/F_\infty - 1)D/H}{(F/F_\infty - 1)_{SL}} \times 100\%$$

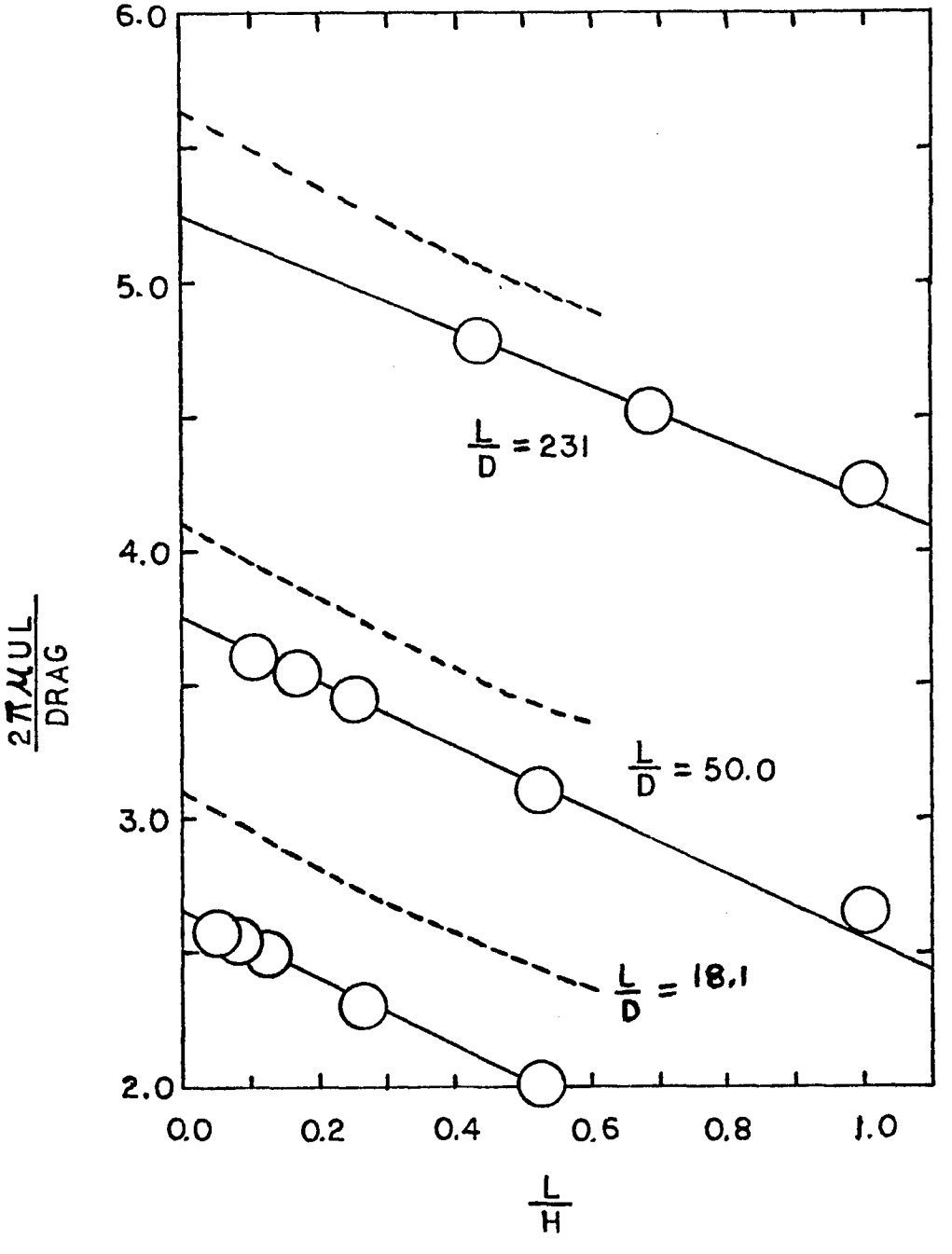

Fig. 3.4 INVERSE DIMENSIONLESS DRAG VERSUS L/H. THE DASHED LINES REPRESENT WAKIYA'S THEORY FOR PROLATE SPHEROIDS.

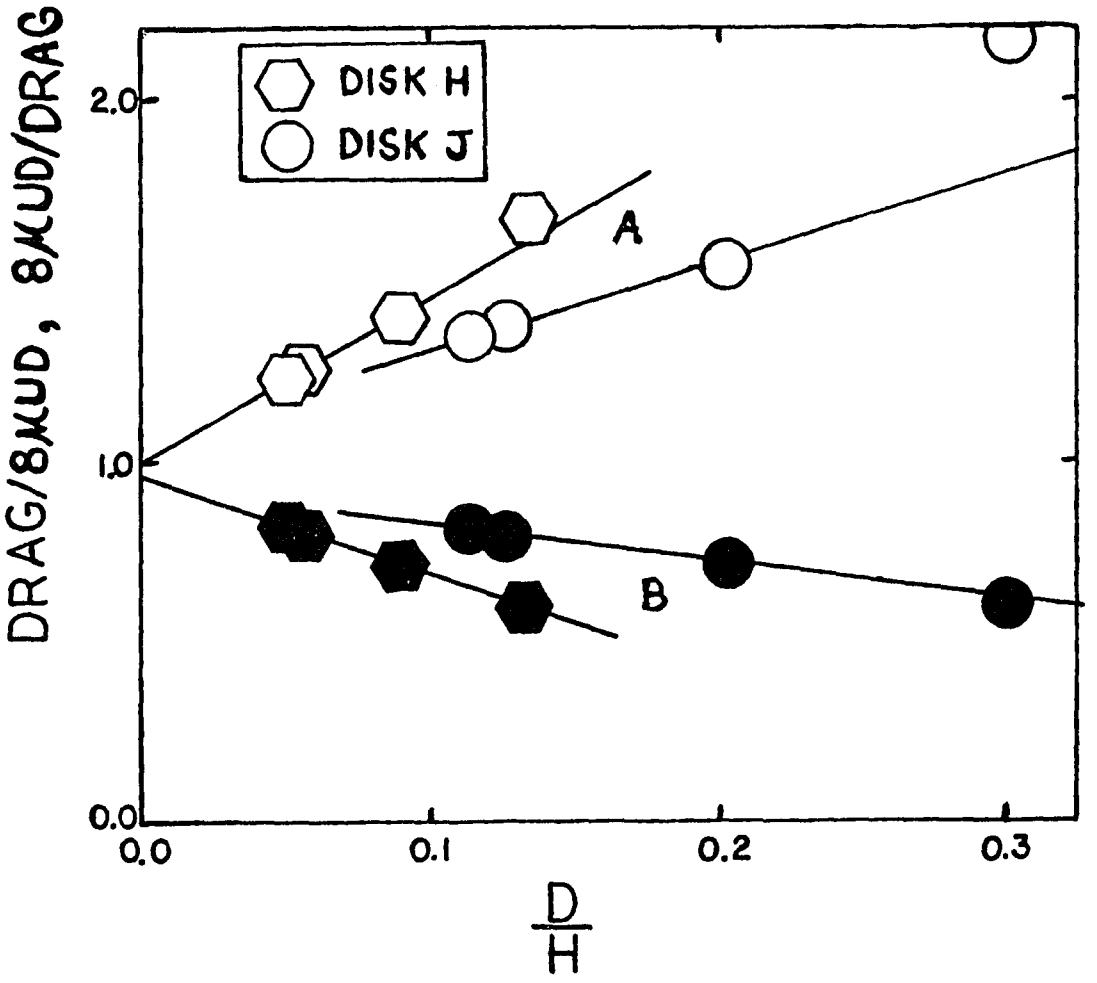

Fig. 3.5 A PLOT OF (A) m'a/8μUD AND (B) 8μUD/m'a VERSUS D/H.

and

$$\Delta F2 = \frac{(1-F_\infty/F)_{SL} - (1-F_\infty/F)_{D/H}}{(1-F_\infty/F)_{SL}} \times 100\%$$

were calculated, where the subscript D/H denotes that the function enclosed in the brackets was evaluated at D/H using Eqs. (1.34) and (1.35) and the subscript SL denotes that the function enclosed in the brackets was evaluated at D/H by using straight line (SL) expressions of the form $(1-F_\infty/F) = A(D/H)$ and $(F/F_\infty - 1) = B(D/H)$. The slope A was determined by dividing by 0.01, Wakiya's value of $(1-F_\infty/F)$ at D/H = 0.01 and the slope B was determined by dividing by 0.01, Wakiya's value of $(F/F_\infty-1)$ at D/H = 0.01. For the present experiment, values of D/H ranged from 0.0431 to 1.235. The results are displayed in Fig. 3.6 where $\Delta F1$ and $\Delta F2$ are plotted vs D/H for L/D = 0.01. As can be seen $\Delta F2$ remains close to zero over the range $0.01 \leq D/H \leq 0.1$, whereas $\Delta F2$ deviates very quickly from zero percent. Equations (1.28) and (1.29) were used to calculate $\Delta F1$ and $\Delta F2$ for a prolate spheroid with L/D = 100, in a manner similar to that for the oblate spheroid case. For the prolate spheroid, $(F/F_\infty-1)$ and $(1-F_\infty/F)$ were evaluated at L/H instead of at D/H. The slope of the straight line expression $(1-F_\infty/F) = A'(L/H)$ was determined by dividing by 0.1, the value of $(1-F_\infty/F)$ at L/H = 0.1 given by Eqs. (1.28) and (1.29). Similarly the slope of

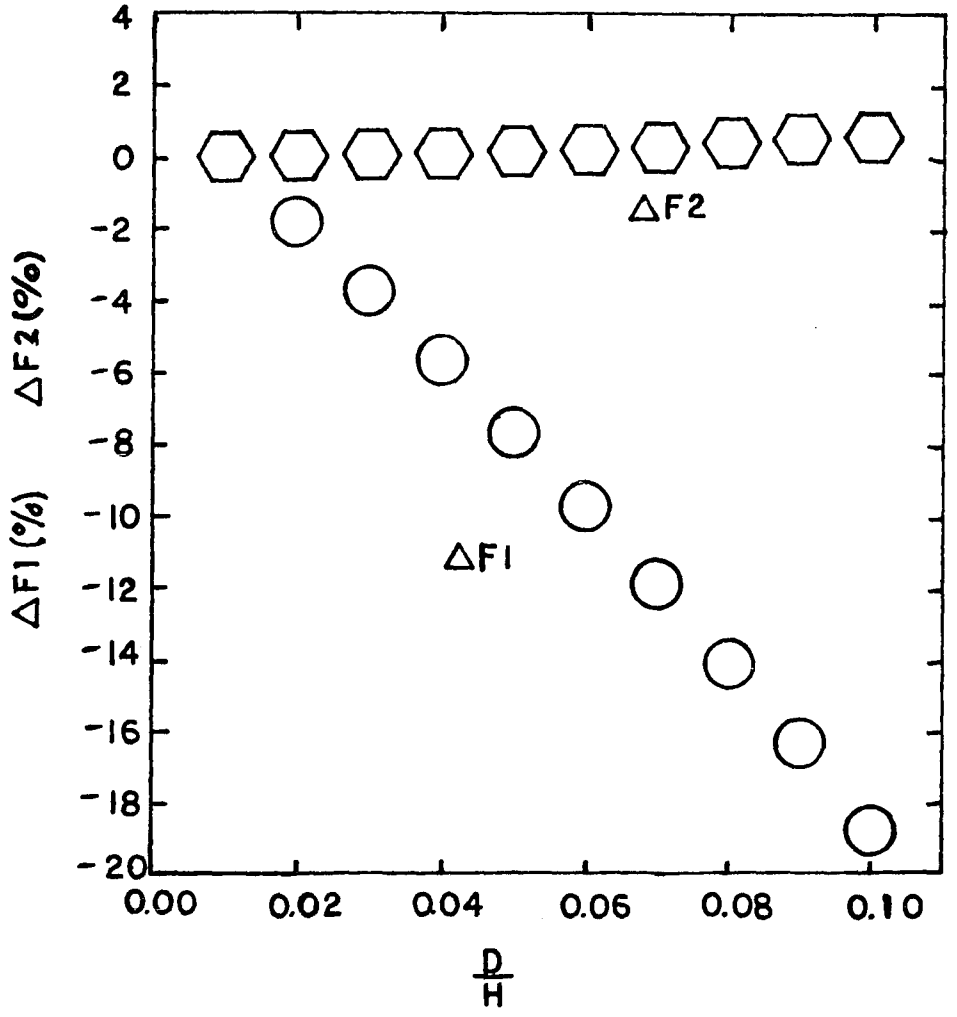

Fig. 3.6 DEVIATION FROM A STRAIGHT LINE CALCULATED FOR WAKIYA'S THEORY OF OBLATE SPHEROIDS (L/D = 0.01).

the straight line expression $(F/F_\infty-1) = B'(L/H)$ was determined by dividing by 0.1, the value of $(F/F_\infty-1)$ at $L/H = 0.1$ given by Wakiya's expressions. In the present experiment, the values of L/H were in the range $0.0543 < L/H < 5.036$. The results are displayed in Fig. 3.7, where $\Delta F1$ and $\Delta F2$ are plotted vs L/H. When the slopes A' and B' are evaluated at 0.1, a plot of F vs 1/H is more linear over a wider range of H than a plot of 1/F vs 1/H. However, as shown in the inset, a plot of 1/F vs 1/H is linear over a wider range of H than a plot of F vs 1/H when $L/H < 0.1$. This suggests that if A' and B' were evaluated at $L/H < 0.1$ (e.g. $L/H = 0.01$) a plot of 1/F vs L/H and not F vs L/H would be linear over a wider range of H. However, the choice of $L/H = 0.1$ is more realistic than $L/H = 0.01$ when the physical dimensions of the present experiment are considered.

The theory of Williams[33] indicates that the minimum distance from the body to the boundary (H-D)/2 rather than the boundary H/2 should be used in Eq. (1.32). However, the difference between H and H-D is insignificant for the long thin cylinders.

The values of F_∞ obtained by extrapolation are compared with theory in Fig. 3.8. The theoretical results for slender cylinders, Eqs. (1.14), (1.15), (1.19) and (1.23), all have as the leading term $\varepsilon = [\ell n(2L/D)]^{-1}$,

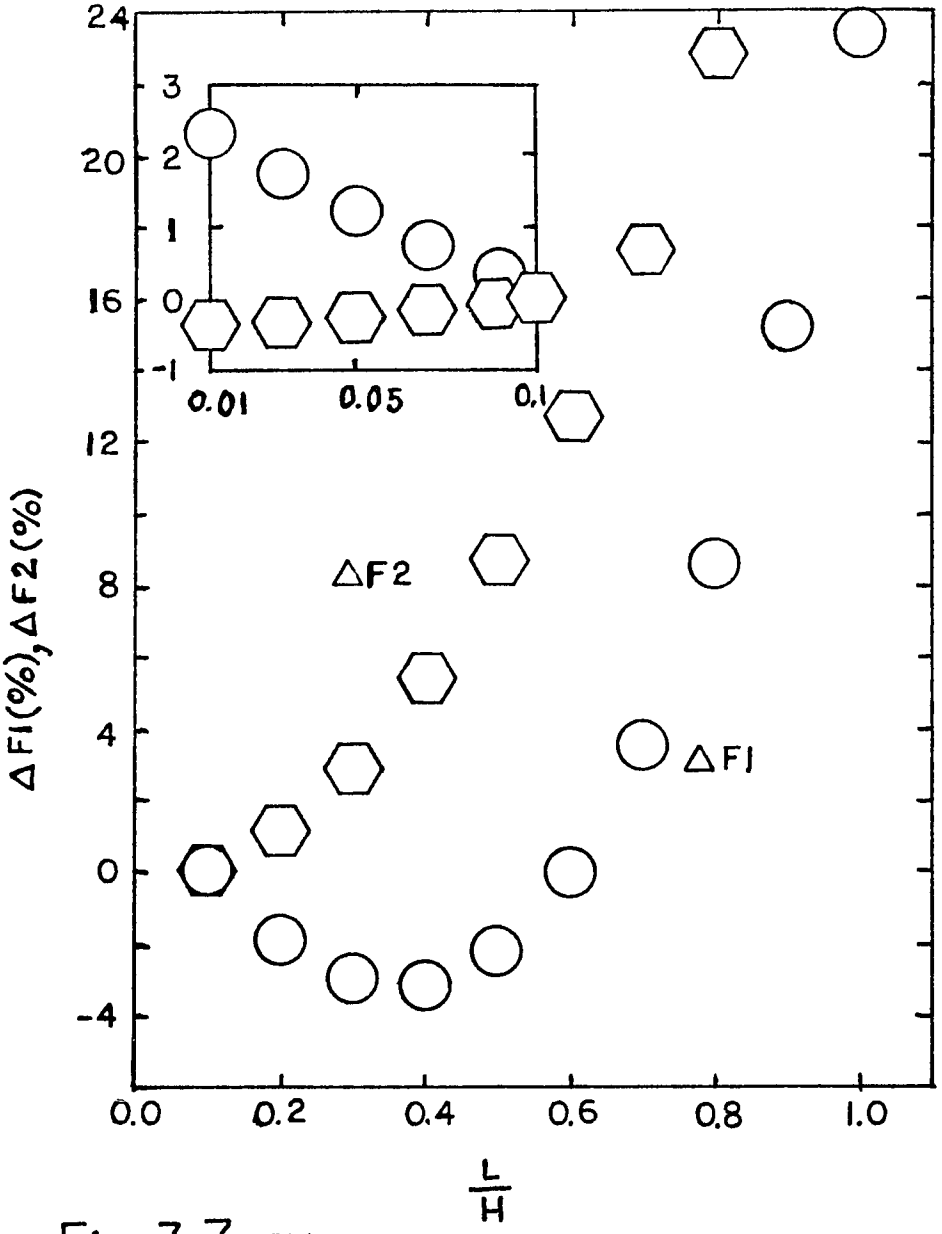

Fig. 3.7 DEVIATION FROM A STRAIGHT LINE CALCULATED FOR WAKIYA'S THEORY OF PROLATE SPHEROIDS (L/D = 100).

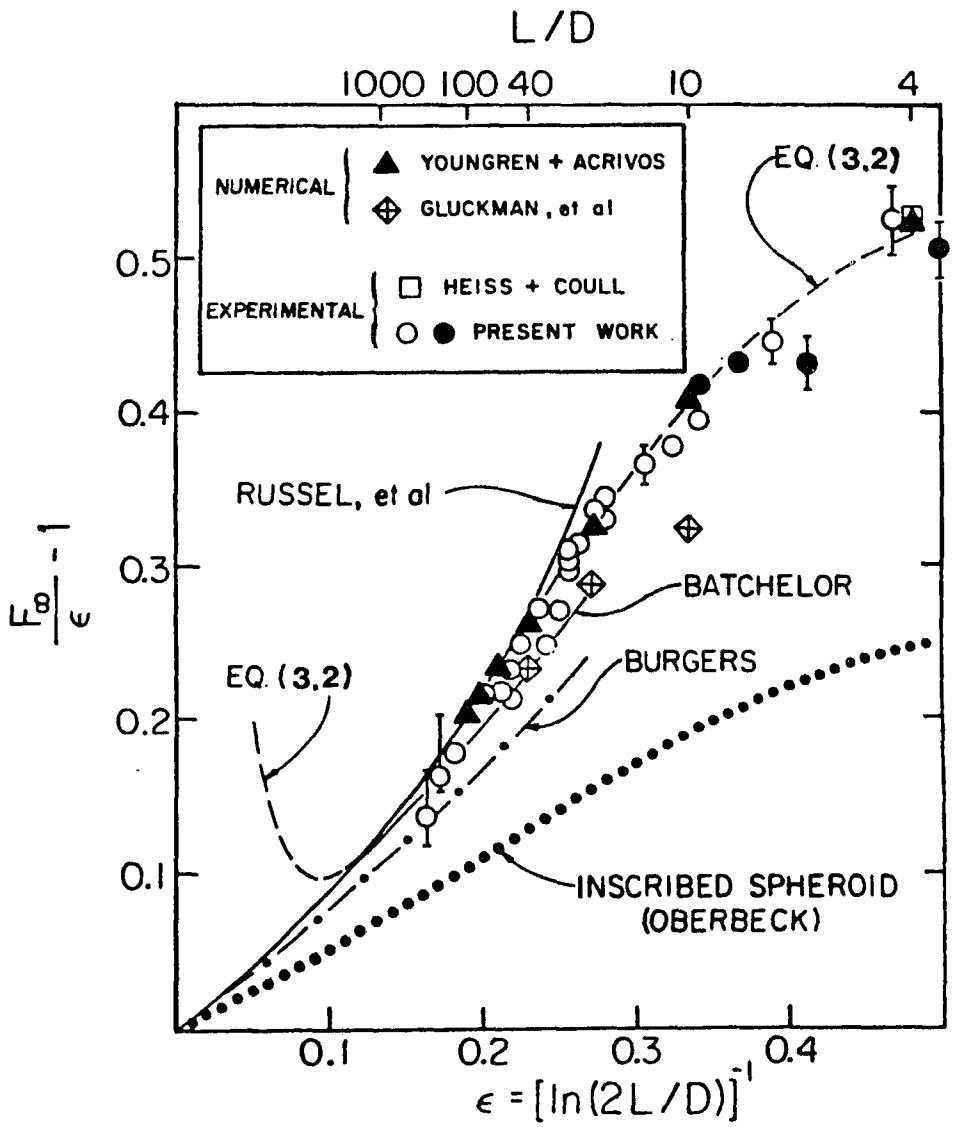

Fig. 3.8 Comparison of our experimental results for long cylinders with expressions from slender body theory and with numerical calculations. The open circles are our results for steel cylinders and the closed circles are for acrylic cylinders. Error bars are indicated for some selected experimental points.

so a sensitive method of presenting the results is to plot $(F_\infty/\varepsilon)-1$ vs ε. As shown in the figure, our experimental values are in good agreement with the slender body results of Batchelor and of Russel *et al.*, for $\varepsilon < 0.2$, and agree well with the values calculated by Youngren and Acrivos for $4 \leq L/D \leq 100$. From the values of Youngren and Acrivos and from Roger's calculated values for L/D = 10 and 4, we have obtained the following empirical relation:

$$F = 0.0244 + 0.5504\varepsilon + 3.328\varepsilon^2 - 2.971\varepsilon^3 \ . \qquad (3.2)$$

This relation is plotted as the dashed curve in Fig. 3.8. The result for the drag on an inscribed prolate spheroid, calculated from the exact solution of Oberbeck,[30] is similar in form but consistently less than the drag on the corresponding circular cylinder. For the inscribed prolate spheroid, the major and minor axes are assigned the same values as the length and diameter of a corresponding cylinder.

C. Short Cylinders

Values of the drag were calculated by Roger by means of the beads-on-a-shell method for cylinders of length to diameter ratio ranging from 0 to 10. The results for axial motion are presented in Table I, along with the calculated values of Youngren and Acrivos,[17] Gluckman et al.,[18] and Swanson et al.,[19] and the experimental values of Heiss and Coull.[22] The results for transverse motion are presented in Table X, along with the calculated values of Swanson et al. and the experimental values of Heiss and Coull. Roger's values for the drag are consistent with but slightly lower than previous values. F_d is the axial drag $(\sigma-\rho)\frac{\pi D^2 L}{4} g$ divided by $8\mu UD$, the exact solution for the disk of zero thickness. As in Chapter 2, σ is the density of the cylinder and ρ is the density of the fluid. Other authors have used the settling factor K defined as

$$K \equiv \frac{6\pi\mu UR}{(\sigma-\rho)\frac{\pi D^2 L}{4} g} = \frac{24\mu UR}{(\sigma-\rho)D^2 Lg} \tag{3.3}$$

where $R = \frac{1}{2}\left(\frac{3}{2} D^2 L\right)^{1/3}$ is the radius of the sphere having a volume equal to the volume of the cylinder. By solving the equation

$$F_d = \frac{\pi g D^2 L}{4} \frac{(\sigma-\rho)}{8\mu UD} = \frac{K'}{K} = \frac{K'(\sigma-\rho)D^2 Lg}{24\mu UR} \tag{3.4}$$

TABLE X

Values of the Dimensionless Drag
For Short Cylinders in Transverse Motion

	DRAG/(16μUD/3)		
L/D	Roger	Swanson *et al.*	Heiss and Coull
0.00	1.0001		
0.50	1.6606	1.663	1.671
1.00	2.1243	2.126	2.141
1.50	2.5319		
2.00	2.9094	2.908	2.903
4.00	4.2518	4.239	4.236
10.00	7.6240		

we see that

$$K' = \frac{3\pi}{8} \left(\frac{3}{2} \frac{L}{D}\right)^{1/3} . \qquad (3.5)$$

Therefore the relation between F_d and K is

$$Fd = \frac{3\pi}{8K} \left(\frac{3}{2} \frac{L}{D}\right)^{1/3} . \qquad (3.6)$$

For $L/D \leq 1$, Roger's calculated values are represented well by the equation

$$F_d = 1 + 0.437A - 0.0749A^3 + 0.0623A^5 - 0.0250A^7 , \qquad (3.7)$$

where A = L/D.

The equation above is plotted in Fig. 3.9 along with our experimental results and the experimental results of Heiss and Coull[23] and of Blumberg and Mohr.[24] Also shown is Equation (3.2), the curve fit for long cylinders. Neither Equation (3.7) nor (3.2) represents the results well in the region $1 < L/D < 4$. The following equation serves as an interpolation between Equations (3.7) and (3.2) in that region:

$$F_d = 1.0276 + 0.3963A - 0.0259A^5 + 0.0014A^3 . \qquad (3.8)$$

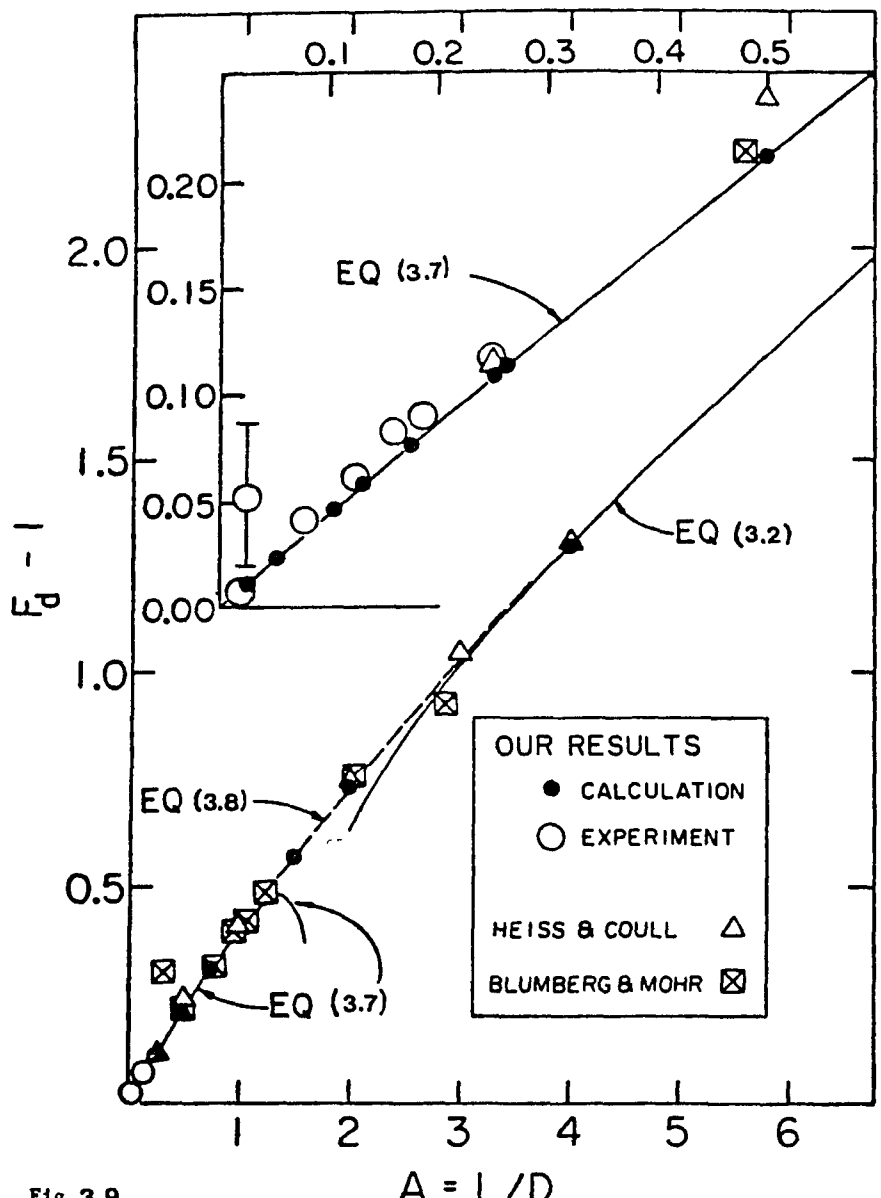

Fig. 3.9 Comparison of experimental results for short cylinders with Roger's beads-on-a-shell calculations (small closed circles). Equations (3.2), (3.7) and (3.8) are empirical curve fits.

Experimental values for the drag on disks are shown as the open circles in Fig. 3.9. The influence of the outer boundary was determined as for long cylinders by using Wakiya's theory[27] for spheroids as a model. As stated earlier in Chapter 1, Wakiya's expression for the effect of a cylindrical boundary on the drag of an oblate spheroid can be written

$$\frac{F}{F_\infty} = [1 - \lambda(\frac{D}{H}) + \delta(\frac{D}{H})^3]^{-1} \qquad (1.36)$$

where λ and δ are functions of the aspect ratio A = L/D. See Equations (1.35), (1.37) and (1.38). We assume that the boundary effect for disks can be represented by an expression having the same form as Equation (1.36) but with different coefficients λ and δ. However, in the limit $A \to 0$, the value of λ must approach 1.786 and the value of δ must approach 1.128 since in that limit both the oblate spheroid and the disk approach the same shape, namely the disk of zero thickness.

Empirical expressions for λ and δ were obtained as follows: Initial values for the drag F_∞ in a fluid of infinite extent were obtained by plotting 1/F vs 1/H and extrapolating to (1/H) = 0. These initial values were used along with data for which the cubic term in Equation (1.36) could be neglected (D/H < 0.15) to determine the dependence of λ on A, which was found to be

$$\lambda = 1.786(1+0.44A) \quad . \tag{3.9}$$

Equation (3.9) is consistent with Brenner's theory[30] for the boundary effect on a particle of arbitrary shape and our Eq. (3.8) for the dependence of F_∞ on A. Equation (3.9) was used along with data for which $D/H < 0.15$ to obtain improved values of F_∞, which were then used along with Equation (3.9) and all of the data ($0.043 < D/H < 0.31$) to obtain the following approximate expression for δ:

$$\delta = 1.128 + 3(A)^{1/2} \quad . \tag{3.10}$$

Then Equations (3.9) and (3.10) were used to obtain the final values of F_∞. The resulting correlation of the boundary effect data for disks is shown in Fig. 3.10 where a plot of $1 - F_\infty/F$ vs $\lambda(D/H)-\delta(D/H)^3$ is given.

D. Inertial Corrections

The influence of fluid inertia was assumed to be negligible. This assumption was checked in the following manner. The inertial contribution to the drag was estimated from Breach's theory (see Chapter 1D) for spheroids. For the long cylinders, approximated by prolate spheroids, the inertial contribution is given by the second and third terms of Equation (1.54)

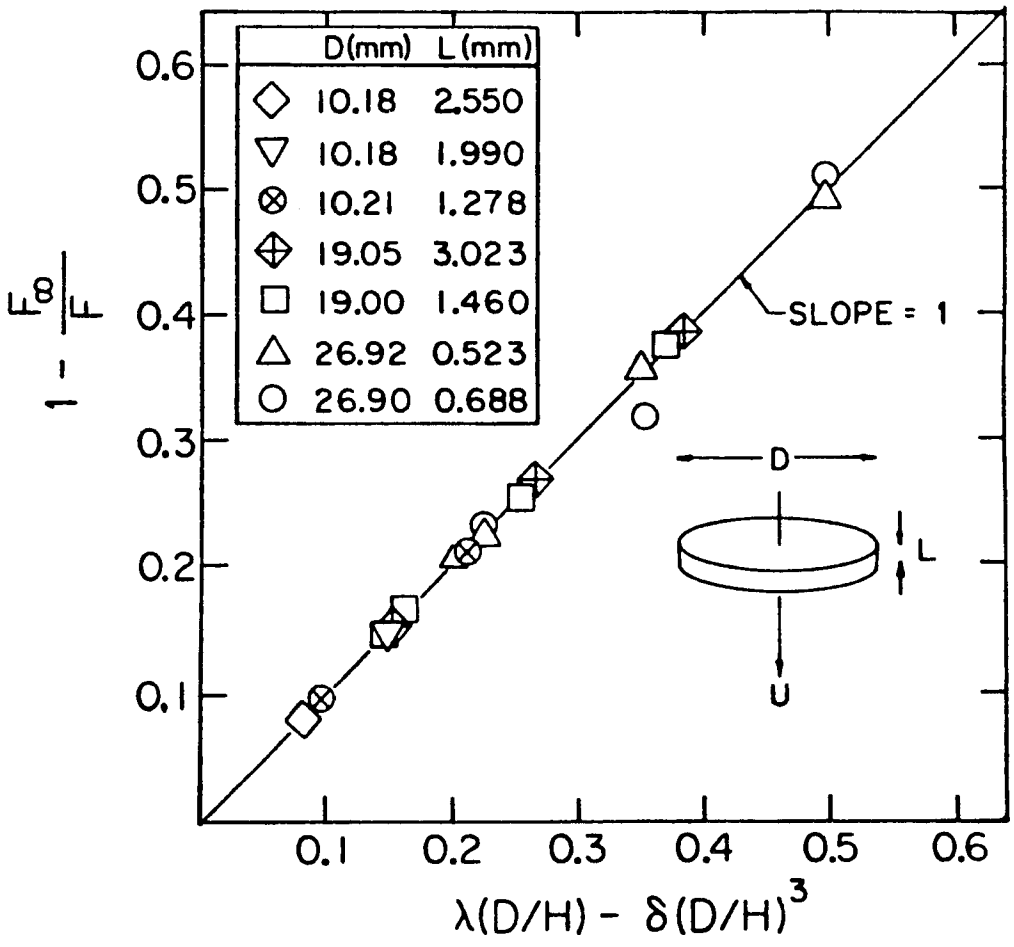

Fig. 3.10 Correlation of the boundary effect data for disks. The coefficients λ and δ are given by Eqs. (3.9) and (3.10) respectively. Both F and F_s are made dimensionless by the same factor, $8\mu UD$.

$$\left(\frac{D'}{D_o} - 1\right) \times 100\% = \left(\frac{BR_e}{24} + \frac{B^2R_e^2}{360} \ln R_e\right) \times 100\% \qquad (3.4)$$

where

$$D_o = \frac{\pi\mu ULB}{(1-e^2)}$$

and $R_e = UL\rho/2\mu$ is based on the half length L/2. As can be seen in Table XI, this contribution did not exceed 0.33% and was typically less than 0.1%. For the disks, approximated by oblate spheroids, the inertial contribution is given by

$$\left(\frac{D'}{D_o} - 1\right) \times 100\% = \left(\frac{bR_e}{24} + \frac{b^2}{360} R_e^2 \ln R_e\right) \times 100\% \qquad (3.5)$$

where

$$D_o = \frac{2\pi\mu UD_b}{3} \quad .$$

The largest contribution was 0.59% for disk I and the average value was 0.29% (see Table XII).

E. Effects due to the Bottom Boundary

The effect of the solid wall at the bottom of the tank, on the data was checked in two ways: (1) by measuring the velocity of a cylinder at the middle of a tank with two different fluid depths, 46 cm and 16.6 cm, and (2) by measuring cylinder velocities at different depths with a constant overall depth of 49 cm. For the first

TABLE XI

Inertial Correction for Long Cylinders

Cylinder	$R_e = \frac{UL\rho}{2\mu}$	$(D/D_o-1)x100\%$
16A	$2.48x10^{-2}$	$1.09x10^{-1}$
17A	$7.15x10^{-2}$	$3.30x10^{-1}$
18A	$4.80x10^{-2}$	$2.37x10^{-1}$
19B	$4.73x10^{-2}$	$2.59x10^{-1}$
21D	$4.88x10^{-3}$	$2.87x10^{-2}$
21C	$5.92x10^{-3}$	$3.59x10^{-2}$
21B	$1.66x10^{-2}$	$1.00x10^{-1}$
21A	$2.90x10^{-2}$	$1.76x10^{-1}$
22A	$3.59x10^{-2}$	$2.23x10^{-1}$
22C	$4.18x10^{-2}$	$2.98x10^{-1}$
22B	$1.34x10^{-2}$	$8.46x10^{-2}$
23A	$1.30x10^{-2}$	$8.65x10^{-2}$
24B	$1.66x10^{-2}$	$1.13x10^{-1}$
24A	$2.02x10^{-2}$	$1.42x10^{-1}$
25C	$9.43x10^{-3}$	$6.81x10^{-2}$
25D	$6.98x10^{-3}$	$5.07x10^{-2}$
25B	$1.26x10^{-2}$	$9.14x10^{-2}$
25A	$2.39x10^{-2}$	$1.73x10^{-1}$
26A	$1.59x10^{-2}$	$1.18x10^{-1}$
27B	$1.31x10^{-2}$	$1.02x10^{-1}$
27A	$1.74x10^{-2}$	$1.36x10^{-1}$
27C	$5.93x10^{-3}$	$4.75x10^{-2}$

TABLE XI (cont'd)

27D	4.45×10^{-3}	3.58×10^{-2}
30A	5.60×10^{-3}	4.98×10^{-2}
32A	8.18×10^{-3}	7.78×10^{-2}
34A	4.90×10^{-3}	4.95×10^{-2}
34B	7.18×10^{-3}	7.25×10^{-2}
36A	5.22×10^{-3}	5.74×10^{-2}
41A	3.31×10^{-3}	4.16×10^{-2}
46A	1.52×10^{-3}	2.21×10^{-2}
49A	1.80×10^{-3}	2.79×10^{-2}

TABLE XII

Inertial Correction for Short Cylinders
or Disk-Like Objects

DISK	$R_e(r)$	$(D/D_o-1)x100\%$
A	$1.36x10^{-2}$	$4.31x10^{-1}$
B	$1.04x10^{-2}$	$3.29x10^{-1}$
C	$7.23x10^{-3}$	$2.29x10^{-1}$
G	$6.96x10^{-3}$	$2.41x10^{-1}$
H	$3.50x10^{-3}$	$1.22x10^{-1}$
I	$1.70x10^{-2}$	$5.87x10^{-1}$
J	$2.90x10^{-3}$	$1.03x10^{-1}$

case, the dimensionless drag per unit length $F = m'g/2\pi\mu UL$ was measured for a cylinder 22C ($L = 4.206$ cm) at fluid depths of 46 and 16.6 cm in a boundary of diameter $H = 21.25$ cm. The shorter fluid depth was achieved by placing a false bottom within the cylindrical boundary. F was found to be 0.3076 without the false bottom and 0.3083 with the false bottom. This is a difference of

$$\frac{0.3083 - 0.3076}{0.3076} \times 100\% = 0.23\% .$$

Velocities were measured as functions of the distance of the mid-point of the measuring interval (d mid), from the bottom of the tank. The product μU rather than U, was evaluated to account for the variations in velocity due to changes in the fluid viscosity. The data are listed in Table XIII, and are plotted in Fig. 3.11 as $\frac{(\Delta\mu U)}{\mu U} \times 100\%$ vs $\frac{d\ mid}{L}$. $\Delta\mu U$ is equal to $\mu_o U_o - \mu U$, where $\mu_o U_o$ is the product μU measured near the middle of the tank. As long as the lower end of the cylinder was more than two cylinder lengths from the bottom, the velocity was the same within 0.4%.

TABLE XIII

Data for the Effect of the Bottom Boundary

Cylinder	L	H	d	d_{mid}	d_{mid}/L	μU	$\mu_o U_o$	$(\Delta\mu U/\mu U)x100\%$
15A	15.23	21.25	5.027	22.37	1.469	6.8112	6.8112	0
			5.066	17.33	1.138	6.8131		-0.03
			5.092	12.25	0.804	6.7645		+0.69
			5.112	7.15	0.469	6.7491		+0.91
16A	9.134	21.25	10.093	19.84	2.172	5.7751	5.7751	0
			5.092	12.25	1.341	5.7684		+0.12
			5.112	7.15	0.783	5.7006		+1.29
18A	7.816	13.32	10.071	29.92	3.828	14.013	14.013	0
			5.066	17.33	2.217	13.946		+0.48
			5.112	7.15	0.915	13.918		+0.68
25C	1.819	13.32	4.978	37.45	20.59	11.994	11.984	
			5.027	22.37	12.30	11.973		
			5.112	7.15	3.93	11.961		+0.19
21A	3.840	13.32	4.978	37.45	9.753	17.227	17.208	
			5.027	22.37	5.826	17.189		
			5.112	7.15	1.862	17.244		-0.21
27D	1.153	13.32	4.978	37.45	32.48	9.0946	9.0504	
			5.027	22.37	19.40	9.0061		
			5.112	7.15	6.20	9.0377		+0.14

TABLE XIII (cont'd)

18A	7.816	8.955	10.071	29.92	3.828	12.808	12.808	0
			5.066	17.33	2.217	12.769		+0.30
			5.112	7.15	0.915	12.741		+0.52
25C	1.819	8.955	4.978	37.45	20.59	11.595	11.584	
			5.027	22.37	12.30	11.572		
			5.112	7.15	3.93	11.570		+0.12
21A	3.840	8.955	4.978	37.45	9.753	16.353	16.331	
			5.027	22.37	5.826	16.309		
			5.112	7.15	1.862	16.261		+0.43
27D	1.153	8.955	4.978	37.45	32.48	8.9405	8.8749	
			5.027	22.37	19.40	8.8093		
			5.112	7.15	6.20	8.8573		+0.20
18A	7.816	4.32	10.071	29.92	3.828	10.830	10.760	
			5.027	22.37	2.862	10.690		
			5.112	7.15	0.915	10.712		
25C	1.819	4.32	4.978	37.45	20.59	10.566	10.543	
			5.027	22.37	12.30	10.520		
			5.112	7.15	3.93	10.513		+0.28

21B	3.233	2.18	10.071	29.92	9.255	8.2300		
			5.112	7.15	2.212	8.2115		+0.22
21A	3.840	2.18	4.978	37.45	9.753	11.379	11.375	
			10.071	29.92	7.792	11.371		
			5.112	7.15	1.862	11.386		-0.10
18A	7.816	2.18	10.071	29.92	3.828	8.8437	0	
			5.066	17.33	2.217	8.8516		-0.09
			10.158	14.78	1.891	8.8108	+0.37	
25D	1.610	2.18	10.071	29.92	18.58	7.6148	0	
			5.066	17.33	10.76	7.6052		+0.13
			5.092	12.25	7.609	7.6275		-0.17
			5.112	7.15	4.441	7.5669		+0.63

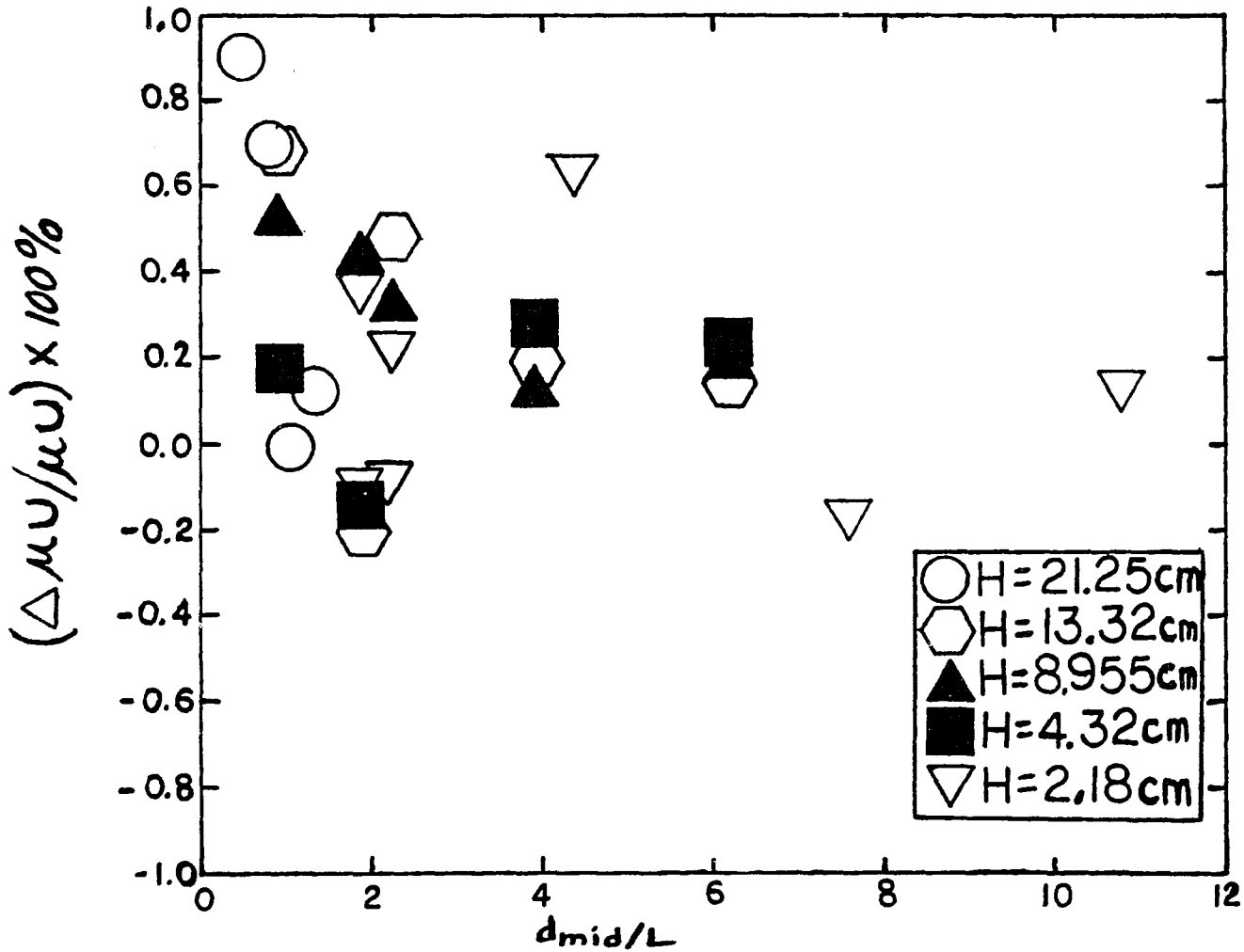

Fig. 3.11 THE CHANGE IN VELOCITY VS. THE DISTANCE OF THE MID-POINT OF THE MEASURING INTERVAL FROM THE BOTTOM OF THE TANK DIVIDED BY L.

CHAPTER 4

DISCUSSION

A. Axial Motion

The present measurements, combined with those of Heiss and Coull, and Blumberg and Mohr, provide experimental values of the Stokes drag on a circular cylinder in axial motion for length to diameter ratios in the range 0.019 to 231. Over the entire range there is good agreement with the available theoretical results. For the cylinder with the largest ratio $L/D \simeq 231$, $L = 9.134$ cm and $D = 0.03952$ cm. Cylinders which are longer and thinner are difficult to work with because they tend to flex. At these cylinder lengths $L > 9$ cm, one must also deal with the spatial requirements placed on the size of the tank containing the fluid. These factors make measurements for $L/D > 200$ difficult. However, this is the region for which the slender body expressions [Eqs. (1.18), (1.22) and (1.23)] are expected to be accurate. Similarly, for $L/D < 0.019$ it is reasonable to assume that the simple linear relation $8\mu UD[1+0.437(L/D)]$, obtained from the beads-on-a-shell calculations will be valid. Therefore, we conclude that accurate values of the Stokes drag for a cylinder in axial motion are available for all length to diameter ratios. Values of the drag can be obtained

from Eq. (1.18) for L/D > 75, Eq. (3.2) for 4 < L/D < 75, Eq. (3.8) for 1 < L/D < 4, and Eq. (3.7) for L/D < 1.

B. Transverse Motion

For a cylinder moving perpendicular to its axis of rotational symmetry, accurate drag results are lacking in the intermediate region 10 <L/D < 100. However, such results can be inferred by interpolation in the following manner: As discussed earlier in Chapter 2, the ratio of transverse drag (F_{tr}) to axial drag (F_{ax}) approaches 2 as $\varepsilon \to 0$. For $0<\varepsilon<0.2$, values of the drag ratio F_{tr}/F_{ax} can be obtained from the slender body calculations of Russel et al. as represented by our Eq. (1.23) and Stalnaker's[35] Eq. (4). At the other extreme ($\varepsilon > 0.3$), values of F_{tr} and F_{ax} are available from Roger's beads-on-a-shell calculations and from the measurements of Heiss and Coull. The resulting values of F_{tr}/F_{ax} are plotted vs. ε in Fig. 4.1. Assuming that there is a smooth variation of the drag ratio in the intermediate region, we have found that the following simple equation can be used for interpolation:

$$F_{tr}/F_{ax} = 2 - 2\varepsilon + \varepsilon^3 + \varepsilon^4 \ . \qquad (4.1)$$

From Eq. (4.1) and the values of F_{ax} calculated by Youngren and Acrivos it is possible to obtain the corresponding

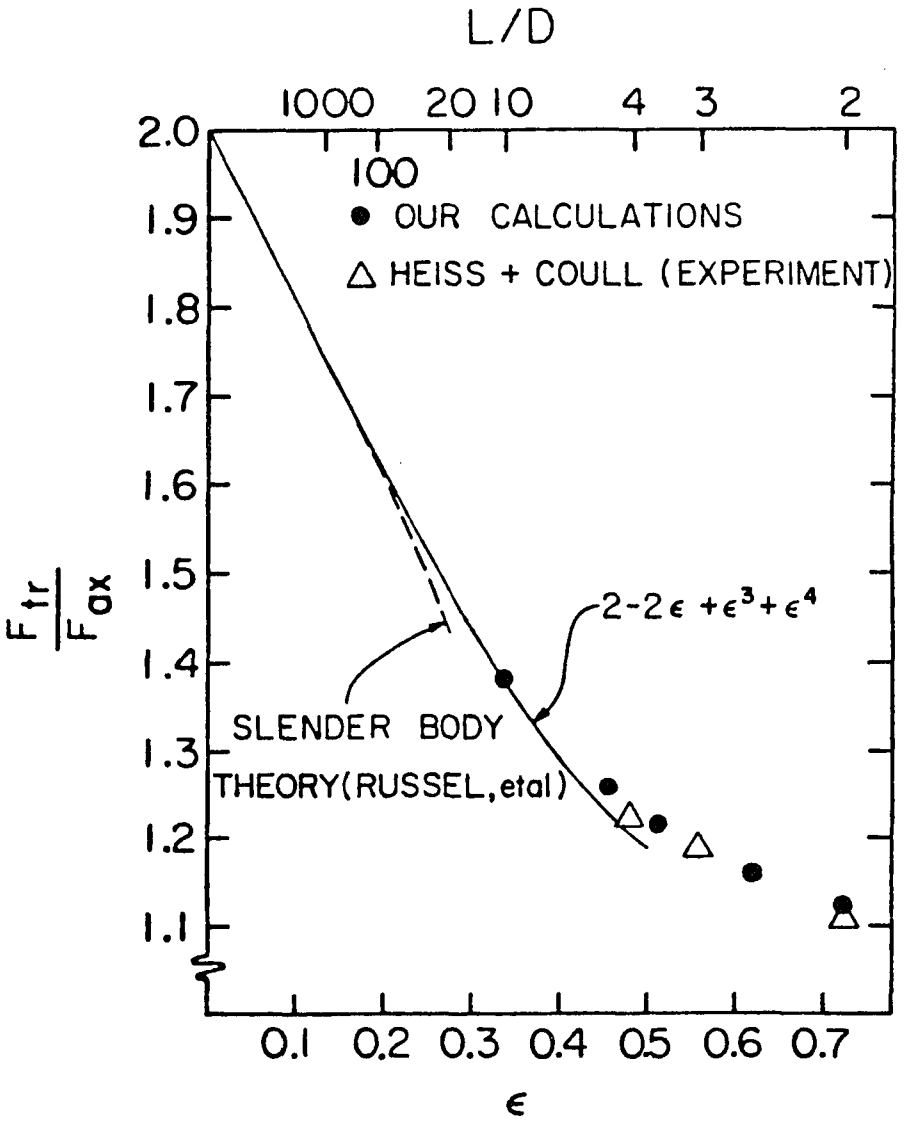

Fig. 4.1 *Interpolation curve for the ratio of transverse to axial Stokes drag for a circular cylinder.*

values of F_{tr}, which are given in Table XIV. Both F_{tr} and F_{ax} are made dimensionless by the same factor $2\pi\mu UL$, so for $\varepsilon << 1$, F_{ax} approaches ε and F_{tr} approaches 2ε.

C. Beads-on-a-Shell Calculations

In Tables I (axial motion) and II (transverse motion), it is shown that Roger's calculated values for the drag on short cylinders are slightly less than values calculated by other authors. We believe that these small differences are due to the manner in which the different calculations treat the sharp corners at which the curved cylindrical surface meets the flat end faces of the cylinder. Youngren and Acrivos have shown that the viscous stress at the surface is sharply peaked at the corner, as one would expect on physical grounds. Roger has obtained a similar result, as shown in Fig. 2.3. Here the normalized stress force (in the axial direction) is plotted for a cylinder of L/D = 1 as one proceeds from the center of an end face (S = 0) around the corner (S = 1) to a point halfway up the cylindrical surface (S = 2), as done by Youngren and Acrivos. The normalized stress force is obtained by calculating the force on a particular axisymmetric ring of beads divided by the total surface area of the beads in that ring $[(F/A)_{RING}]$ and dividing that ratio by the ratio of the force on the entire array of

TABLE XIV

Values of F_{tr} Obtained from the Interpolated Values of F_{tr}/F_{ax} (Fig. 4.1) combined with the Values for F_{ax} From Youngren and Acrivos.

L/D	F_{tr}/F_{ax}	F_{tr} = drag/$2\pi\mu UL$
20	1.483	0.533
40	1.558	0.449
60	1.593	0.410
80	1.615	0.386
100	1.631	0.370

beads to the surface area of the entire array [$(F/A)_{ARRAY}$].

Figure 4.2 shows the changes that occur in the stress distribution near the corner when different arrays of beads are used. In an array of equally spaced beads (array A) with one bead (bead C) centered at the corner, the maximum stress force occurs on the bead at the corner, while the stress force on the two beads adjacent to the corner (beads b and d) is significantly lower than on other beads nearby. This peculiar drop in the stress on those beads immediately adjacent to the corner occurs regardless of the size of the beads, so it must be an artifact of the model rather than a real physical effect. When the corner is rounded (array C) by moving bead C to a position midway between beads b and d, the maximum stress force shifts to bead d (the bead nearest the corner on the cylindrical surface) while the stress force on beads c and e drops to a low value. In array B, the corner is square and additional overlapping beads are concentrated near the corner; again, the bead at the corner has the largest stress force, but now the overlapping bead b on the flat face has a negative value of stress force, and both beads d and e on the cylindrical surface have low values.

In Fig. 4.3 is shown the extrapolation of the drag to zero bead radius for each of the arrays of Fig. 4.2.

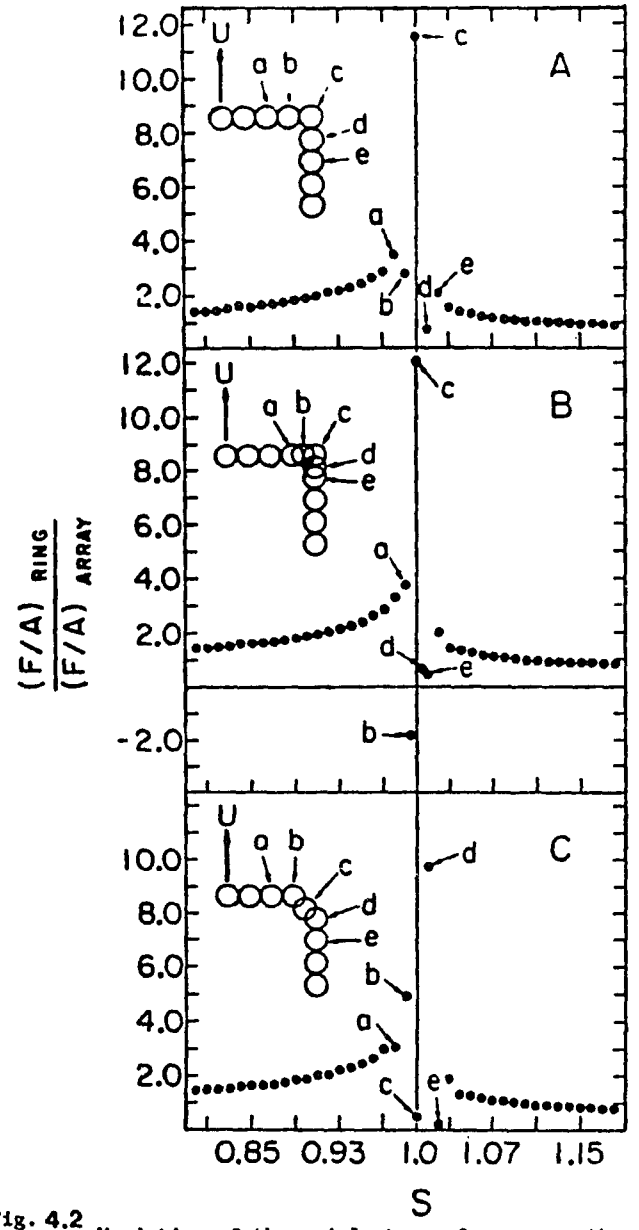

Fig. 4.2 Variation of the axial stress force near the corner for three different arrays of beads.

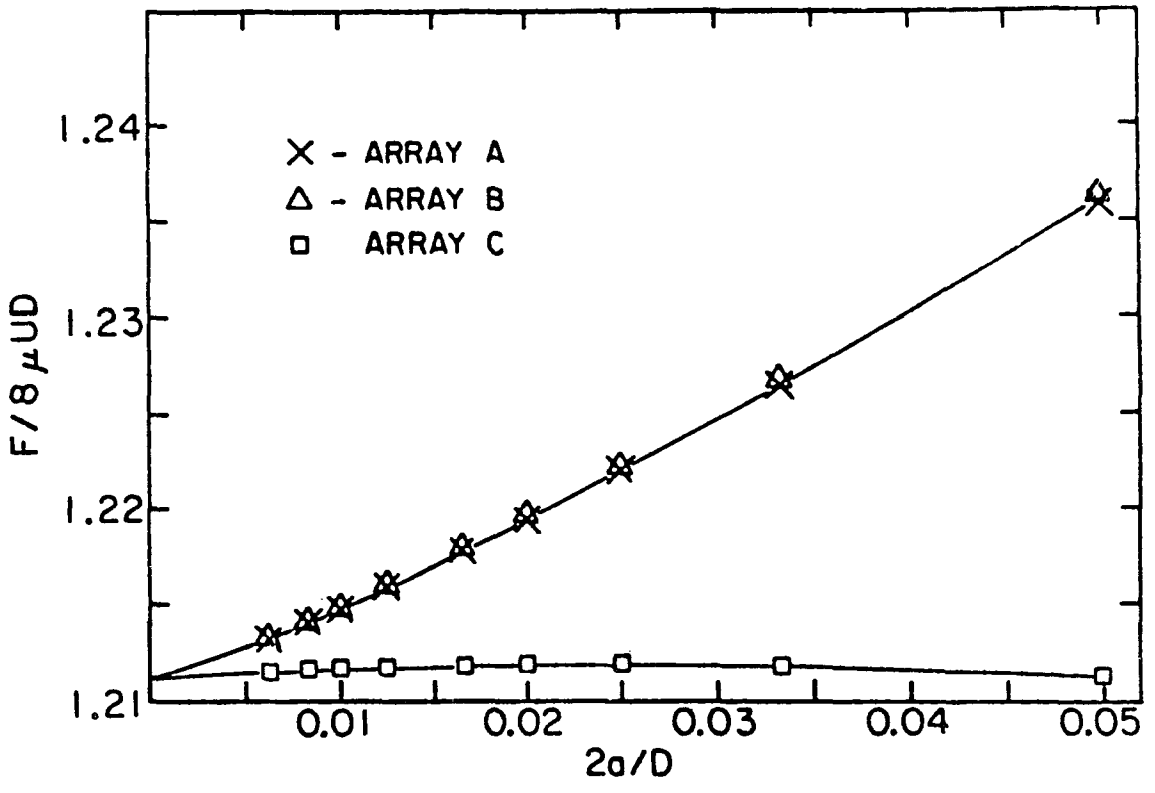

Fig. 4.3 Extrapolation curves for the three different arrays of Fig. 4.2.

The extrapolation curves for arrays A and B are practically identical, as are the extrapolated values of the drag F_d (1.2109 for both A and B). For array C, although the extrapolation curve is considerably different, the extrapolated drag value F_d = 1.2111 is within 0.2% of the values for A and B. Vivian O'Brien[63] has pointed out that the infinite values of pressure that occur at sharp corners are mathematical rather than physical anomalies; every corner of a real object will be slightly rounded. Roger's results are consistent with the finite difference results of Vivian O'Brien: when the corner point is part of the fluid rather than part of the solid surface (array C), the drag for non-zero sphere size is a better approximation to the extrapolated value.

The peculiar oscillation of the stress force near the corner suggests a possible flaw in the beads-on-a-shell model when applied to objects with sharp edges. To investigate this question further, Roger has used the method to calculate the drag on several objects for which analytical solutions are known. The results of his calculations for the ideal disk of zero thickness, the sphere, the cardioid, the hemispherical cap and two lens shapes formed from the intersection of two spheres, are given in Table II. In each case the calculations were carried out until the ratio of bead diameter to outside diameter of the object was 0.015 or less, and extrapolation to

zero bead diameter was done by least squares fit to a polynomial of order 1 to 3. For the two lens shapes and the flat disk, oscillations in the stress force occur which are similar to that of Fig. 4.2A but which are symmetrical about the edge. However, the amplitude of the oscillation decreases as the lens interior angle increases from 0° to 120°. As shown in Table II, the differences between the calculated and the exact values for the drag are quite small. Therefore, we conclude that although the beads-on-a-shell method may give unrealistic oscillations in the stress force as a sharp corner is approached, the drag values obtained from the method are reliable, at least for the convex shapes to which it has been applied thus far.

There is an apparent inconsistency between Roger's calculations for the short cylinders and the results obtained by Swanson et al.,[19] who also used the beads-on-a-shell model. We believe that the difference is due to the use of different cutoff values for the Gauss-Seidel iteration and the use of different extrapolation methods. Swanson et al., stopped their iteration when succession values differed by less than 0.1%, and they used a linear extrapolation to zero bead size. Roger continued the iteration until successive values differed by less than 0.0001% and extrapolated with least squares curve fits up to order 3. The convergence of the Gauss-Seidel

iteration is illustrated in Fig. 4.4 for the case L/D = 1.0, total number of beads = 1202, and a ratio of bead diameter to cylinder diameter of 0.05. In using the Gauss-Seidel method it is necessary to make an estimate of the drag on each bead. When the average drag per bead for the array was taken as the initial extimate (with each bead initially having equal drag), the convergence pattern shown in the middle of Fig. 4.4 was obtained. In the upper pattern the initial estimate was 30% lower than the average drag per bead and in the lower pattern the initial estimate was 30% higher. The arrows show the points at which successive values differ by less than 0.1%, 0.01%, 0.001% and 0.0001%. It is clear that a 0.1% cutoff can cause positive or negative errors as large as 1%.

D. Summary

We present here a summary of our conclusions:

1. Finite Cylinder in a Fluid of Infinite Extent

The slender body calculations of Keller and Rubinow (Eq. (1.21)), and Batchelor (Eq. (1.18)) agree well with our experimental results as anticipated for $\varepsilon < 0.2$ (long thin cylinders), and the numerically integrated slender body result of Russel et al. follows closely our experimental results until ε approaches 0.23. The drag calculated from the approximate solution of Burgers (Eq. (1.14)) is consistently less than our experimental results.

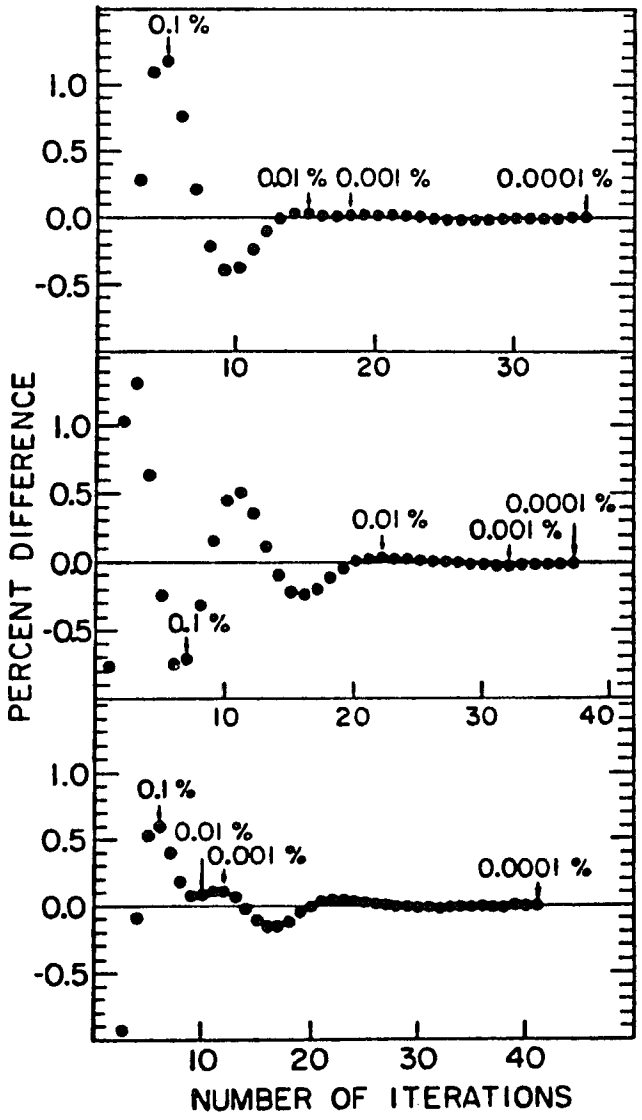

Fig. 4.4 Convergence of the Gauss-Seidel iteration for the case L/D = 1. The middle pattern was obtained when the initial estimate of the drag on each bead was taken as the total drag divided by the total number of beads. In the upper pattern, the initial estimate was 30% lower and in the lower pattern it was 30% higher. The arrows indicate points at which successive iterations differ by less than the given percentages.

Broersma's expression for the drag (same as Eq. (1.14) except for a coefficient of 0.81 instead of 0.72) gives values of the drag which are close to our experimental results for $\varepsilon < 0.2$ but are consistently less ($\sim$ 1%) than the results predicted by Batchelor for $\varepsilon < 0.2$. In the intermediate region $4 \leq L/D \leq 100$ ($0.1887 \leq \varepsilon \leq 0.4809$), experiment agrees well with the numerical calculations of Youngren and Acrivos. The numerical results of Gluckman et al. for L/D equal to 10 ($\varepsilon = 0.3338$), 20 ($\varepsilon = 0.2711$) and 40 ($\varepsilon = 0.2282$) are consistently lower than our experimental results, which suggests that the touching oblate spheroid method fails to treat accurately, the effects at the edge f the cylinder, on the total drag of the body. This hypothesis is consistent with the observation in Fig. 3.8 that the agreement between experiment and the results of Gluckman et al. improve as L/D increases (ε decreases). The contribution to the drag from the edge should diminish in importance, relative to the contribution from the rest of the body as the cylinder becomes thinner and longer. For $0.25 \leq L/D \leq 4$, the theoretical approaches of Youngren and Acrivos, and Swanson et al. agree well with the experimental results of Heiss and Coull, and of Blumberg and Mohr. Our experimental results of the drag for $L/D \leq 0.25$ are consistent with but slightly higher than the beads-on-a-shell calculations of Roger.

2. Boundary Effects

For the long cylinders, a plot of F vs 1/H was found to be linear over a wider range of H than a plot of 1/F vs 1/H, whereas the reverse was true for the short cylinders (i.e. plot of 1/F vs 1/H linear over a wider range of H than a plot of F vs 1/H). Both observations are consistent with Wakiya's theory for prolate and oblate spheroids. The effect of the wall at the bottom of the tank, on the velocity of the cylinders was small (same within 0.4%) as long as the leading edge of the cylinder was more than two cylinder lengths from the bottom.

3. Cylinder of Infinite Length in a Coaxial Boundary of Infinite Depth

It is physically impossible to attain the case of a cylinder of infinite length traveling in a coaxial boundary of infinite depth. However, the exact solution of Happel and Brenner (Eq. (1.10)) should apply near the center of a cylinder with a large length to diameter ratio and with D~H, where end effects are negligible. In the present experiment, this is best approximated by cylinder 16A (L/D = 231) translating in the boundary of diameter H = 2.18 cm. The dimensionless drag per unit length F calculated from Eq. (1.10) for this case is 0.2492 and the experimental value of F is 0.3320, which corresponds to a difference of $\left(\frac{0.3320-0.3267}{0.3267}\right)$ x 100% = 1.62%.

4. Mixing of Silicone Fluids

The time of approach to a steady value of the viscosity of a two component silicone fluid is shorter when the components are added to the tank alternatively in thin layers rather than in bulk to the other before stirring.

5. Transverse Drag

There are now available experimentally tested expressions for the Stokes drag on a circular cylinder in axial motion for the entire length to diameter ratio. When known values of the transverse (Stalnaker's Eq. (4)) to axial drag are plotted vs ε (Fig. 4.1), it is possible to connect these values with a smooth interpolation curve that allows the inference of approximate values of transverse drag from the known values of axial drag in the region 10 L/D 100.

6. Major Result

Our major result is that there are now available experimentally tested expressions for the Stokes drag on a cylinder of finite length moving along its axis in a fluid of infinite extent. This is summarized by our figures 3.8 and 3.9 and by the following expressions:

$$L/D > 100 \quad F = \frac{\text{Drag}}{2\pi\mu UL} = \frac{\varepsilon}{1-\alpha\varepsilon-\beta\varepsilon^2} + 4\varepsilon^5 + 28\varepsilon^6 \qquad (1.23)$$

where

$$\varepsilon = (\ell n \frac{2L}{D})^{-1} , \quad \alpha \equiv \frac{3}{2} - \ell n 2 \quad \text{and} \quad \beta = 1 - \frac{\pi^2}{12} ,$$

and

$$100 > \frac{L}{D} \geq 4 \quad F = 0.0244 + 0.5504\varepsilon + 3.328\varepsilon^2 - 2.971\varepsilon^3 \tag{3.2}$$

and

$$4 > \frac{L}{D} > 1 \quad F_d = \frac{\text{Drag}}{8\mu UD} = 1.0276 + 0.3963A - 0.0259A^2 + 0.0014A^3 , \tag{3.8}$$

where

$$A = L/D$$

and

$$1 \geq \frac{L}{D} \quad F_d = 1 + 0.437A - 0.0749A^3 + 0.0623A^5 - 0.0250A^7 . \tag{3.7}$$

REFERENCES

1. I. G. Currie, Fundamental Mechanics of Fluids (McGraw-Hill Book Company, New York, 1974) p. 35.

2. Philip M. Morse and Herman Feshbach, Methods of Theoretical Physics (McGraw-Hill Book Company, New York, 1953) Part I, p. 703.

3. G. K. Batchelor, An Introduction to Fluid Dynamics (Cambridge University Press, Cambridge, U.K., 1979).

4. J. Happel and H. Brenner, Low Reynolds Number Hydrodynamics (Nordhoff, Leyden, 1973) second edition, p. 53.

5. C. R. Illingworth, in Laminar Boundary Layers, edited by L. Rosenhead (Clarendon, Oxford, 1963) p. 168.

6. H. Schlichting, Boundary Layer Theory (McGraw-Hill Book Company, New York, 1979) seventh edition, p. 14.

7. J. Happel and H. Brenner, Low Reynolds Number Hydrodynamics (Nordhoff, Leyden, 1973) second edition, p. 342.

8. C. Brennen and H. Winet, Ann. Rev. Fluid Mech. 9, 339 (1977).

9. D. F. Katz, J. R. Blake and S. L. Paveri-Fontana, J. Fluid Mech. 72, 529 (1975).

10. J. M. Burgers, in Second Report on Viscosity and Plasticity of the Amsterdam Academy of Sciences (Nordemann, New York, 1938) Chap. 3.

11. S. Broersma, J. Chem. Phys. 32, 1632 (1960).

12. R. G. Cox, J. Fluid Mech. 44, 791 (1970).

13. G. K. Batchelor, J. Fluid Mech. 44, 419 (1970).

14. J. B. Keller and S. I. Rubinow, J. Fluid, Mech. 75, 705 (1976).

15. Milton Van Dyke, Perturbation Methods in Fluid Mechanics (Parabolic Press, Stanford California, 1978) p. 77.

16. W. B. Russel, E. J. Hinch, L. G. Leal and G. Tieffenbruck, J. Fluid Mech. 83, 273 (1977).

17. G. K. Youngren and A. Acrivos, J. Fluid Mech. 69, 377 (1975).

18. M. J. Gluckman, S. Weinbaum and R. Pfeffer, J. Fluid Mech. 55, 677 (1972).

19. E. Swanson, D. Teller and C. de Haen, J. Chem. Phys. 68, 5097 (1978).

20. R. P. Roger and R. G. Hussey, Phys. Fluids 25, 915 (1982).

21. D. C. Teller, E. Swanson and C. de Haen, in Methods in Enzymology, edited by C. H. W. Hirs (Academic Press, New York, 1979), Volume 61, p. 112.

22. J. Garcia de la Torre and V. A. Bloomfield, Q. Rev. Biopphys. 14, 81 (1981).

23. J. F. Heiss and J. Coull, Chem. Eng. Prog. 48, 133 (1952).

24. P. N. Blumberg and C. M. Mohr, AIChe J. 14, 331 (1968).

25. Private communications with R. P. Roger.

26. N. J. de Mestre, J. Fluid Mech. 58, 641 (1973).

27. N. J. de Mestre and W. B. Russel, J. Eng. Math. 9, 81 (1975).

28. D. F. Moore, Principles and Applications of Tribology (pergamon Press, New York, 1975) p. 113.

29. S. Wakiya, J. Phys. Soc. Jpn. 12, 1130 (1957).

30. H. A. Oberbeck, Crelles J. 81, 62 (1876).

31. I-D. Chang, Z. Angew. Math. Phys. 12, 6 (1961).

32. H. Brenner, J. Fluid Mech. 12, 35 (1962).

33. W. E. Williams, J. Fluid Mech. 24, 285 (1966).

34. B. Huner and R. G. Hussey, Phys. Fluids 20, 81211 (1977).

35. J. F. Stalnaker and R. G. Hussey, Phys. Fluids 22, 603 (1979).

36. Y. J. Chen and R. G. Hussey, Phys. Fluids 23, 853 (1980).

37. Allen T. Chwang and T. Yao-Tsu Wu, J. Fluid Mech. 67, 787 (1975).

38. T. L. Jahn and F. F. Jahn, How to Know the Protozoa (Wm. C. Brown Company Publishers, Dubuque, Iowa, 1949) pp. 31-35.

39. G. I. Taylor, in Problems of Hydrodynamics and Continuum Mechanics (SIAM, Philadelphia, 1969) English edition, p. 718; see also Low Reynolds Number Flows (film) (Educational Services, Cambridge, 1967).

40. J. P. K. Tillett, J. Fluid Mech. 44, 401 (1970).

41. H. F. Weinberger, J. Fluid Mech. 52, 321 (1972).

42. A. N. Whitehead, Quart. J. Math. 23, 143 (1889).

43. C. W. Oseen, in Neure Methoden Und Ergebnisse In Der Hydrodynamik, edited by E. Hilk (Akademische Verlagsgesellschaft, Leipzig, 1927).

44. I. Proudman and J. R. A. Pearson, J. Fluid Mech. 2, 237 (1957).

45. W. Chester and D. R. Breach, J. Fluid Mech. 48, 771 (1971).

46. T. Maxworthy, J. Fluid Mech. 23, 369 (1965).

47. J. Lloyd Sutterby, Trans. Soc. Rheol. 17, 559 (1973).

48. D. R. Breach, J. Fluid Mech. 10, 306 (1961).

49. H. Brenner, J. Fluid Mech. 11, 604 (1961).

50. H. Brenner and R. G. Cox, J. Fluid Mech. 17, 561 (1963).

51. A. M. D. Amarakoon, "Experimental Study of the Fluid Drag on a Torus at Low Reynolds Number," Ph.D. Dissertation, Louisiana State University, 1982.

52. C. C. Currie and B. F. Smith, Ind. Eng. Chem. 42, 2457 (1950).

53. H. Yamakawa, J. Chem. Phys. 53, 436 (1979).

54. V. Bloomfield, W. O. Dalton and K. E. Van Holde, Biopolymers 5, 135 (1967).

55. J. Rotne and S. Prager, J. Chem. Phys. 50, 4831 (1969).

56. T. J. Ui, R. G. Hussey and R. P. Roger (submitted to Phys. Fluids).

57. J. M. Dorrepaal, M. E. O'Neill and K. B. Ranger, J. Fluid Mech. 75, 273 (1976).

58. D. H. Michael and M. E. O'Neill, J. Fluid Mech. 80, 785 (1977).

59. S. Wakiya, Arch. Mech. 32, 809 (1980).

60. L. E. Payne and W. H. Pell, J. Fluid Mech. 7, 529 (1980).

61. W. D. Collins, Mathematika 10, 72 (1963).

62. S. Weinbaum, J. Fluid Mech. 33, 39 (1968).

63. V. O'Brien, J. Fluids Eng. 104, 500 (1982).

64. Table of Series, Products and Integrals, edited by J. M. Ryzhik and I. S. Gradshteyn (VEB Deutscher Verlag der Wissenschaften, Berlin, 1963), p. 307.

65. Handbook of Mathematical Functions, edited by M. Abramowitz and I. A. Stegun (U. S. Government Printing Office, Washington, D. C., 1964).

APPENDIX I

ANALYTICAL SOLUTIONS OF BATCHELOR'S INTEGRALS H_{01} AND H_{02}

Batchelor employs a term H_{mn} defined by

$$H_{mn} = (m+1) \int_0^1 \xi^m \{\ell n(1-\xi^2)^{\frac{1}{2}}\}^n d\xi. \tag{A1}$$

The special cases H_{01} and H_{02} can be evaluated analytically. We consider first H_{01}:

$$H_{01} = \int_0^1 [\ell n(1-\xi^2)^{\frac{1}{2}}] d\xi \ . \tag{A2}$$

The integral can be rewritten as

$$H_{01} = \frac{1}{2} [\int_0^1 \ell n(1+\xi) d\xi + \int_0^1 \ell n(1-\xi) d\xi] \ . \tag{A3}$$

Consider the first term. Let $x = \ell n(1+\xi)$; then $e^x = (1+\xi)$, or $d\xi = (1+\xi)dx = e^x dx$. When $\xi = 1$, $x = \ell n\ 2$, and when $\xi = 0$, $x = \ell n(1+0) = 0$. Therefore,

$$\int_0^1 \ell n(1+\xi) d\xi = \int_0^{\ell n 2} xe^x dx = xe^x - e^x \Big|_0^{\ell n 2} = 2(\ell n 2) - 1 \ . \tag{A4}$$

Similarly, for the second term we let $x = \ell n(1-\xi)$; then $e^x = (1-\xi)$ and $d\xi = -e^x dx$. When $\xi = 1$, $\ell n(1-1) = -\infty$, and when $\xi = 0$, $\ell n(1-0) = 0$. Hence,

$$\int_0^1 \ell n(1-\xi)d\xi = -\int_0^{-\infty} xe^x dx = \int_{-\infty}^0 xe^x dx = -1 \ . \qquad \text{(A5)}$$

Therefore,

$$H_{01} = \frac{1}{2}\,[2\ell n(2)-2] = \ell n(2)-1 = -0.3068528... \qquad \text{(A6)}$$

$$\cong -0.307.$$

This is the result obtained by Batchelor.

The solution of H_{02}

$$H_{02} = \int_0^1 [\ell n(1-\xi^2)^{\frac{1}{2}}]^2 d\xi \qquad \text{(A7)}$$

is accomplished as follows. The integral can be rewritten as

$$H_{02} = \frac{1}{4}\int_0^1 [\ell n(1-\xi^2)]^2 d\xi \ . \qquad \text{(A8)}$$

Let $-x = \ell n(1-\xi^2)$; then $e^{-x} = 1-\xi^2$, and $\xi = (1-e^{-x})^{\frac{1}{2}}$. Therefore,

$$d\xi = \left(\frac{1-\xi^2}{2\xi}\right)dx = \frac{e^{-x}}{2(1-e^{-x})^{\frac{1}{2}}}\,dx \ .$$

When $\xi = 0$, $-x = \ell n(1-0) = 0$ or $x = 0$, and when $\xi = 1$, $-x = \ell n(1-1) = -\infty$ or $x = +\infty$, so the integral becomes

$$H_{02} = \frac{1}{8}\int_0^{\infty} x^2 e^{-x}(1-e^{-x})^{-\frac{1}{2}}\,dx \ . \qquad \text{(A9)}$$

H_{02} can now be solved using the method of Laplace transforms. Let

$$f(s) = \mathcal{L}(F(x)) = \int_0^{\infty} e^{-sx}(1-e^{-x})^{-\frac{1}{2}}\,dx \ , \qquad \text{(A10)}$$

where $F(x) = (1-e^{-x})^{-\frac{1}{2}}$. We use the following property of Laplace transforms:

$$\int_0^{\infty} x^2 e^{-sx}(1-e^{-x})^{-\frac{1}{2}}dx = (-1)^2\,\frac{d^2}{ds^2}\,f(s) \ . \qquad \text{(A11)}$$

In the present case $s = 1$. Therefore, from equations (A9) and (A11) we have

$$H_{02} = \frac{1}{8}\,\frac{d^2 f(s)}{ds^2}\Big|_{s=1} \ . \qquad \text{(A12)}$$

The problem has been reduced to evaluating

$$\int_0^{\infty} e^{-sx}(1-e^{-x})^{-\frac{1}{2}}\,dx \ . \qquad \text{(A13)}$$

Let $z^2 = (1-e^{-x})$, and take $z = +(1-e^{-x})^{\frac{1}{2}}$. Then $2zdz = e^{-x}dx$, $dx = e^{x}2zdz = 2(1-z^2)^{-1}zdz$, and $e^{-sx} = (1-z^2)^{s}$. Substitution into (A13) leads to

$$\int_0^{\infty} e^{-sx}(1-e^{-x})^{-\frac{1}{2}}\,dx = 2\int_0^{1}(1-z^2)^{s-1}dz. \qquad \text{(A14)}$$

The limits of integration are: when x=0, z=0, and when $x=\infty$, z=1. However,

$$\int_0^{1}(1-z^2)^{s-1}dz = 2^{2s-2}\,B(S,s)$$

$$= \frac{1}{2}\,B(\tfrac{1}{2},s) \qquad \text{(A15)}$$

(p. 294 Gradshteyn and Ryzhik)[64]

where $B(\frac{1}{2},s)$ is the Beta function:

$$B(\tfrac{1}{2},s) = \frac{\Gamma(\frac{1}{2})\Gamma(s)}{\Gamma(\frac{1}{2}+s)}\ . \qquad \text{(A16)}$$

Therefore,

$$H_{02} = \int_0^{1}[\ell n(1-\xi^2)^{\frac{1}{2}}]d\xi$$

$$= \frac{1}{8}\frac{d^2}{ds^2}\,[B(\tfrac{1}{2},s)]_{s=1}$$

$$= \frac{1}{8} \frac{d^2}{ds^2} \left[\frac{\Gamma(\frac{1}{2})\Gamma(s)}{\Gamma(s+\frac{1}{2})} \right]_{s=1}$$

$$= \frac{\sqrt{\pi}}{8} \frac{d^2}{ds^2} \left[\frac{\Gamma(s)}{\Gamma(s+\frac{1}{2})} \right]_{s=1} , \tag{A18}$$

since $\Gamma(\frac{1}{2}) = \sqrt{\pi}$. If we perform the differentiation and set s equal to one, Equation (A18) becomes

$$H_{02} = \frac{\sqrt{\pi}}{8} \frac{\Gamma^2(\frac{3}{2})[\Gamma(\frac{3}{2})\Gamma''(1) - \Gamma(1)\Gamma''(\frac{3}{2})] - 2\Gamma(\frac{3}{2})\Gamma'(\frac{3}{2})[\Gamma(\frac{3}{2})\Gamma'(1) - \Gamma(1)\Gamma'(\frac{3}{2})]}{\Gamma^4(\frac{3}{2})} \tag{A19}$$

Rather than differentiating the gamma functions directly, we use the di-gamma and tri-gamma functions. The di-gamma function is

$$\psi(x) = \frac{d \ \ell n \Gamma(x)}{dx} = \frac{1}{\Gamma(x)} \frac{d\Gamma(x)}{dx} = \frac{\Gamma'(x)}{\Gamma(x)} \tag{A20}$$

and the tri-gamma function is

$$\frac{d\psi(x)}{dx} = \psi'(x) \ . \tag{A21}$$

Therefore,

$$\Gamma'(x) = \psi(x)\Gamma(x) \quad \text{and} \tag{A22}$$

$$\Gamma''(x) = \psi'(x)\Gamma(x) + \psi(x)\Gamma'(x)$$

$$= \Gamma(x)(\psi'(x) + \psi^2(x)) \ . \tag{A23}$$

In terms of $\psi(x)$ and $\psi'(x)$, Eq. (A19) is

$$H_{02} = [\frac{\sqrt{\pi}}{8} \div \Gamma^4(\tfrac{3}{2})] \ [A - B] \tag{A24}$$

where

$$A = \Gamma^2(\tfrac{3}{2}) \ [\Gamma(\tfrac{3}{2})\Gamma(1)(\psi'(1) + \psi^2(1)) - \Gamma(1)\Gamma(\tfrac{3}{2})[\psi'(\tfrac{3}{2}) + \psi^2(\tfrac{3}{2})]$$

$$= \Gamma^3(\tfrac{3}{2}) \ [\Gamma(1)(\psi'(1) + \psi^2(1)) - \Gamma(1)(\psi'(\tfrac{3}{2}) + \psi^2(\tfrac{3}{2})]$$

and

$$B = 2\Gamma^2(\tfrac{3}{2})\psi(\tfrac{3}{2}) \ [\Gamma(\tfrac{3}{2})\psi(1)\Gamma(1) - \Gamma(1)\psi(\tfrac{3}{2})\Gamma(\tfrac{3}{2})]$$

$$= 2\Gamma^3(\tfrac{3}{2})\psi(\tfrac{3}{2}) \ [\psi(1)\Gamma(1) - \Gamma(1)\psi(\tfrac{3}{2})] \ ,$$

so that

$$H_{02} = \frac{\frac{\sqrt{\pi}}{2}\,\Gamma^3(\frac{3}{2})}{4\Gamma^4(\frac{3}{2})}\,[\Gamma(1)(\psi'(1) + \psi^2(1)) - \Gamma(1)(\psi'(\tfrac{3}{2})$$

$$+ \psi^2(\tfrac{3}{2}) - 2\psi(\tfrac{3}{2})(\psi(1)\Gamma(1) - \Gamma(1)\psi(\tfrac{3}{2})]. \qquad \text{(A25)}$$

Inserting $\Gamma(\frac{3}{2}) = \frac{\sqrt{\pi}}{2}$ and $\Gamma(1) = 1$ into the equation above leads to the result:

$$H_{02} = \frac{1}{4}\,[\psi'(1) + \psi^2(1) - \psi'(\tfrac{3}{2}) - \psi^2(\tfrac{3}{2}) - 2\psi(\tfrac{3}{2})\psi(1)$$

$$+ 2\psi^2(\tfrac{3}{2})]\ . \qquad \text{(A26)}$$

According to Abramowitz and Stegun,[65]

$$\psi'(1) = \frac{\pi^2}{6} \quad (6.4.2) \text{ and } (23.2.24)$$

and

$$\psi(1) = -\gamma \quad (6.3.2)$$

where γ is Euler's constant,

$$\gamma = 0.5772156649 \ldots$$

and

$$\psi(z+1) = \psi(z) + \frac{1}{z} \qquad (6.3.5)$$

so that

$$\psi(\tfrac{3}{2}) = \psi(\tfrac{1}{2} + 1) = \psi(\tfrac{1}{2}) + \frac{1}{(\frac{1}{2})} \ .$$

Also,

$$\psi(\tfrac{1}{2}) = -\gamma - 2 \ \ell n \ 2 \ . \qquad (6.3.3)$$

Therefore,

$$\psi(\tfrac{3}{2}) = -\gamma - 2 \ \ell n \ 2 + 2 \ .$$

$\psi'(\frac{3}{2})$ can be evaluated by using

$$\psi^n(z+1) = \psi^n(z) + (-1)^n n! \ z^{-n-1} \qquad (6.4.6)$$

or

$$\psi'(\tfrac{1}{2} + 1) = \psi'(\tfrac{1}{2}) - (1)(\tfrac{1}{2})^{-2}$$
$$= \psi'(\tfrac{1}{2}) - \tfrac{1}{4} \ .$$

However,

$$\psi^{n}(\tfrac{1}{2}) = (-1)^{n+1} n!\,(2^{n+1}-1)\,\xi(n+1) \qquad (6.4.4)$$

or

$$\psi'(\tfrac{1}{2}) = 3\xi(2)$$

$$= \frac{\pi^2}{2} \quad .$$

Therefore,

$$\psi'(\tfrac{3}{2}) = \frac{\pi^2}{2} - 4$$

which leads to the final result

$$H_{02} = -\frac{\pi^2}{12} + 2 - 2\,\ell n\,2 + (\ell n\,2)^2 = 0.271691619 \quad .$$

This agrees with Batchelor's numerical integration result

$$H_{02} \approx 0.272 \quad .$$

APPENDIX II

SOLUTION OF AN INTEGRAL USED BY de MESTRE

In the slender body calculations of the drag coefficient for a cylindrical rod, de Mestre employs the integral,

$$I = \int_{-1}^{+1} \ell n\ (1-\xi^2)d\xi \quad . \tag{A27}$$

The solution of the above integral is similar to the solution of Batchelor's integral H_{01}. Equation (A27) can be rewritten as

$$I = \int_{-1}^{+1} \ell n\ (1+\xi)d\xi + \int_{-1}^{+1} \ell n\ (1-\xi)d\xi \ . \tag{A28}$$

Except for the factor of 1/2 and the lower limit of integration of -1 instead of zero, Equation (A28) is the same as Equation (A3). Consider the first term of (A28). Let $x = (1+\xi)$. When $\xi = 1$, $x = \ell n2$ and when $\xi = -1$, $x = \ell n(1-1) = -\infty$. In the second term of (A28), let $x = (1-\xi)$. When $\xi = 1$, $x = \ell n(1-1) = -\infty$ and when $\xi = -1$, $x = \ell n(1-(-1)) = \ell n\ 2$. Therefore the integral can be rewritten as

$$1 = \int_{-\infty}^{\ell n 2} xe^x \, dx + \left(-\int_{\ell n 2}^{-\infty} xe^x \, dx \right)$$

$$= 2 \int_{-\infty}^{\ell n 2} xe^x \, dx \, . \qquad \text{(A29)}$$

Hence,

$$1 = 2[xe^x - e^x]_{-\infty}^{\ell n 2}$$

$$= 4 \, [\ell n 2 - 1]$$

$$= -1.2274113 \ldots \qquad \text{(A30)}$$

APPENDIX III

EXPERIMENTAL VALUES OF THE DIMENSIONLESS DRAG

$F = m'g/2\pi\mu UL$ FOR LONG CYLINDERS

H(cm)	F				
Cylinder	21.25	13.32	8.955	4.32	2.18
16A	0.2093	0.2215	0.2360		0.3267
17A	0.2322	0.2477	0.2679		0.3948
18A	0.2417	0.2575	0.2759	0.3250	0.4006
19B	0.2696	0.2848	0.3031	0.3589	0.4455
21D	0.2709	0.2748	0.2833	0.3127	0.3655
21C	0.2777	0.2822	0.2907	0.3218	0.3780
21B	0.2867	0.2957	0.3087	0.3530	0.4296
21A	0.2925	0.3042	0.3207	0.3730	0.4638
22A	0.3041	0.3163	0.3338	0.3902	0.4905
22C	0.3076	0.3215	0.3434	0.4046	0.5144
22B	0.2992	0.3068	0.3175	0.3612	0.4368
23A	0.3182	0.3277	0.3400	0.3824	0.4625
24B	0.3175	0.3273	0.3411	0.3868	0.4711
24A	0.3355	0.3447	0.3592	0.4093	0.5045
25C	0.3505	0.3564	0.3671	0.4077	0.4862
25D	0.3473	0.3533	0.3637	0.3992	0.4698
25B	0.3478	0.3558	0.3685	0.4132	0.4985
25A	0.3535	0.3631	0.3791	0.4341	0.5415
26A	0.3625	0.3705	0.3836	0.4331	0.5285
27B	0.3770	0.3850	0.3981	0.4449	0.5381
27A	0.3840	0.3923	0.4073	0.4606	0.5640
27D	0.3881	0.3933	0.4015	0.4334	0.4990
27C	0.3838	0.3895	0.3997	0.4347	0.5077
30A	0.4281	0.4371	0.4;460		0.5585
32A	0.4598	0.4688	0.4811		0.6185
34A	0.4870	0.4959	0.5062		0.6221
34B	0.5365		0.6217		
36A	0.5724		0.6514		
38A	0.5759	0.5813	0.5957		0.7036
41A	0.6623		0.7421		
46A	0.7273	0.7415	0.7538		0.8563
49A	0.8167	0.8402	0.8886		

APPENDIX IV

EXPERIMENTAL VALUES OF THE DRAG

F_d = m'g/8μUD FOR THE DISK-LIKE OBJECTS

H(cm) Disk	23.6	21.25	13.32	8.955
A	1.2242	1.2437	1.3198	1.4439
B	1.1860	1.2074	1.2776	1.3875
C	1.1613	1.1778	1.2444	1.3542
G	1.2837	1.3107	1.4884	1.7621
H	1.2293	1.2574	1.4036	1.6719
I	1.2785	1.3083	1.5685	2.0012
J	1.3469	1.3763	1.5538	2.1637

VITA

Tsukasa Jeff Ui was born to Kazuo and Fumiko Ui on September 1, 1950 in Hiki, Japan. He emigrated to Vancouver, Canada at the age of nine where he received his primary and secondary education. He was awarded a Bachelor of Science in Physics from the University of British Columbia, Vancouver, Canada in May 1973 and a Master of Science in Physics in May 1978 from Simon Fraser University, Burnaby, Canada. He then entered graduate study at Louisiana State University, Baton Rouge, Louisiana, where he is presently a candidate for the degree of Doctor of Philosophy in the Department of Physics and Astronomy.

EXAMINATION AND THESIS REPORT

Candidate: Tsukasa Jeff Ui

Major Field: Physics and Astronomy

Title of Thesis: Experimental Investigation of a Cylinder in Axial Motion at Low Reynolds Number.

Approved:

R. D. Hussey
Major Professor and Chairman

Dean of the Graduate School

EXAMINING COMMITTEE:

R. F. O'Connell

Paul K. Hansma

Charles A. Kelly

G. H. Fredrickson

Herbert Keller

Date of Examination:

April 12, 1984